Dissertation

submitted to the

Combined Faculty of Mathematics, Engineering

and Natural Sciences

of Heidelberg University, Germany

for the degree of

Doctor of Natural Sciences

Put forward by

Daniel Heimfarth

born in: Neuwied, Germany

Oral examination: 18.10.2022

Electrolyte-Gated Transistors with Polymer-Wrapped Carbon Nanotube Networks for Bioelectronics and Brain-Inspired Computing

Referees:

Prof. Dr. Jana Zaumseil

Prof. Dr. Martijn Kemerink

Electrolyte-Gated Transistors with Polymer-Wrapped Carbon Nanotube Networks for Bioelectronics and Brain-Inspired Computing — Networks of polymer-sorted semiconducting single-walled carbon nanotubes (SWNTs) exhibit ideal properties for electrolyte-gated transistors, such as high charge carrier mobilities and a porous morphology. In combination with many electrolytes, such as ionic liquids, the porosity enables volumetric charge accumulation in these networks, comparable to ion-permeable polymers in electrochemical transistors (ECTs). However, the performance of polymer-wrapped SWNTs in water-gated transistors, which are an important component of bioelectronics, is limited by the hydrophobicity of commonly used wrapping-polymers. This limitation is overcome within this thesis by exchanging the hydrophobic wrapping-polymer with an equivalent polymer that features hydrophilic oligoethylene glycol side chains. High performance water-gated transistors with large volumetric capacitances are demonstrated, employing aerosol-jet printed hydrophilic polymer/SWNT hybrids. Furthermore, slow ionc motion in ion-gel-gated dense SWNT networks is studied and implemented as an approach to create artificial synapses, which show promising behavior for the development of neuromorphic devices. The properties of the presented prototypes suggest that future device generations should contain a mixed network of semiconducting and metallic SWNTs as the gating material and avoid all parasitic capacitances by passivation in order to obtain non-volatile device operation. These findings expand the applicability of solution processed SWNT networks for bioelectronics and brain-inspired computing.

Elektrolytgesteuerte Transistoren mit polymer-umwickelten Kohlenstoffnanoröhrchen für die Bioelektronik und gehirn-inspiriertes Rechnen — Netzwerke aus polymer-sortierten, halbleitenden einwandigen Kohlenstoffnanoröhrchen (engl. *Single-Walled Carbon Nanotubes*, SWNTs) weisen ideale Eigenschaften für elektrolytgesteuerte Transistoren auf, wie zum Beispiel hohe Ladungsträgermobilitäten und eine poröse Morphologie. In Kombination mit vielen Elektrolyten, wie ionischen Flüssigkeiten, ermöglicht die Porosität dieser Netzwerke eine volumetrische Ladungsakkumulation, vergleichbar zu ionendurchlässigen Polymeren in elektrochemischen Transistoren (ECTs). Die Leistung von polymer-umwickelten SWNTs in wassergesteuerten Transistoren, die die Basis der Bioelektronik darstellen, ist jedoch durch die Hydrophobie der gebräuchlichsten Wickel-polymere limitiert. Diese Limitierung wird in dieser Thesis durch das Austauschen des hydrophoben Wickelpolymers mit einem äquivalenten Polymer, das hydrophile Oligoethylenglycol-Seitenketten aufweist, überwunden. Leistungsfähige wassergesteuerte Transistoren mit aerosolstrahlgedruckten hydrophilen Polymer/SWNT-Hybriden mit großen volumetrischen Kapazi-täten werden demonstriert. Weiterhin wird die langsame Ionenbewegung in Ionen-Gel-gesteuerten dichten SWNT-Netzwerken untersucht und als Ansatz zur Herstellung von künstlichen Synapsen implementiert, die vielversprechendes Verhalten für die Entwicklung von neuromorphen Bauteilen zeigen. Die Eigenschaften der präsentierten Prototypen deuten darauf hin, dass zukünftige Bauteilgenerationen gemischte Netzwerke aus halbleitenden und metallischen SWNTs als Gating-Material beinhalten sollten, und dass das Entstehen von jeglichen parasitären Kapazitäten durch Passivierung verhindert werden sollte, um nicht-volatilen Bauteilbetrieb zu erzielen. Diese Ergebnisse erweitern die Anwendbarkeit von lösungsprozessierten SWNT-Netzwerken für die Bioelektronik und für das gehirn-inspirierte Rechnen.

List of Publications

Parts of this work have been published in the following reference:

Daniel Heimfarth, Merve Balcı Leinen, Patrick Klein, Sybille Allard, Ullrich Scherf, Jana Zaumseil
Enhancing Electrochemical Transistors Based on Polymer-Wrapped (6,5) Carbon Nanotube Networks with Ethylene Glycol Side Chains
ACS Appl. Mater. Interfaces. **2022**, 14, 8209-8217.

Further publications with own contributions:

Kan Ueji, Nobuhiro Muto, Daniel Heimfarth, Yuya Matsuoka, Yota Ichinose, Yohei Yomogida, Takashi Yagi, Jana Zaumseil, Kazuhiro Yanagi
Heat and Charge Carrier Flow through Single-Walled Carbon Nanotube Films in Vertical Electrolyte-Gated Transistors: Implications for Thermoelectric Energy Conversion
ACS Appl. Nano Mater. **2022**, 5, 6100-6105.

Merve Balcı Leinen, Sebastian Lindenthal, Daniel Heimfarth, Jana Zaumseil
Networks of As-Dispersed, Polymer-Wrapped (6,5) Single-Walled Carbon Nanotubes for Selective Cu^{2+} and Glyphosate Sensing
submitted to Nanoscale **2022**

Abdurrahman Ali El Yumin, Nicolas Zorn, Felix Berger, Daniel Heimfarth, Jana Zaumseil
Trion Electroluminescence from Static p-n Junctions in Networks of Electrolyte-Gated (6,5) Single-Walled Carbon Nanotubes
submitted to ACS Appl. Nano Mater. **2022**

Nicolas F. Zorn, Francesca Scuratti, Felix J. Berger, Andrea Perinot, Daniel Heimfarth, Mario Caironi, Jana Zaumseil

Probing Mobile Charge Carriers in Semiconducting Carbon Nanotube Networks by Charge Modulation Spectroscopy

ACS Nano. **2020**, 14, 2412-2423.

Paul Fassl, Simon Ternes, Vincent Lami, Yuriy Zakharko, Daniel Heimfarth, Paul Hopkinson, Fabian E.Paulus, Alex Taylor, Jana Zaumseil, Yana Vaynzof

The effect of crystal grain orientation on the rate of ionic transport in perovskite polycrystalline thin films

ACS Appl. Mater. Interfaces. **2019**, 11, 2490–2499.

List of Abbreviations

[EMIM][FAP]	1-Ethyl-3-MethylIMidazoliumtris(pentafluoroethyl)trifluorophosphate
AFM	Atomic Force Microscope
AI	Artificial Intelligence
ANN	Artificial Neural Network
AP	Action Potential
DOS	Density Of States
E-QCMD	Electrochemical Quartz Crystal Microbalance with Dissipation monitoring
ECT	ElectroChemical Transistor
EG-FET	Electrolyte-Gated Field-Effect Transistors
EIS	Electrochemcial Impedance Spectroscopy
EL	ElectroLuminescense
EPSC	Excitatory PostSynaptic Current
FET	Field-Effect Transistor
LEFET	Light-Emitting Field-Effect Transistor
LTP	Long-Term Plasticity
NMP	*N*-Mmethyl-2-Pyrrolidone
OCP	Open-Circuit Potential
p(g2T-TT)	Poly(2-(3,3'-bis(2-(2-(2-methoxyethoxy)ethoxy)ethoxy)-[2,2'-biThiophen]-5-yl) Thieno[3,2-b] Thiophene)
P(VDF-HFP	Poly(VinyliDene Fluoride-coHexaFluoro-Propylene
P3HT	Poly(3-HexylThiophene)
PBS	Phosphate-Buffered Saline
PEDOT:PSS	Poly(3,4EthyleneDioxyThiophene):Poly(Styrene Sulfonate)
PFO-BPy	Poly[(9,9-dioctylFluorenyl-2,7-diyl)-alt-(6,6'-[2,2'-BiPyridine])]

PL	Photoluminescense
PLE	PhotoLuminescense Excitation-Emission
PPF	Paired-Pulse Facilitation
PSP	Post-Synaptic Potential
PTFE	PolyTetraFluoroEthylene
RBM	Radial Breathing Mode
SDS	SodiumdoDecylSulphate
SEM	Scanning Electron Microscope
SPA	Semiconductor Parameter Analyzer
SRDP	Spike-Rate Dependent Plasticity
STDP	Spike-Timing Dependent Plasticity
STP	Short-Term Plasticity
SWNT	Single-Walled carbon NanoTube
TEG-PF-BPy	Poly[(9,9-di(2,5,8,11-tetraoxatridecan-13-yl)fluorenyl-2,7-diyl)-alt-(6,6'-[2,2'-bipyridine])]
THF	TetraHydroFuran
UV	UltraViolet
VIS	Visible
VMU	Voltage Monitor Unit

Contents

Chapter 1

Introduction

Technological advances in the electronics and semiconductor industry has been dominated by optimizing and miniaturizing conventional silicon circuits for decades,[1] with the demand for single crystalline silicon growing to date. Meanwhile, the need for alternative semiconductors is driven by novel applications where mechanical flexibility, biocompatibility, or specific optical properties are required, for example for transparent electronics. Especially cheap semiconductors that can be solution processed on a large scale and at low temperatures are desired and can be found in polymers,[2] small molecules[3] or nanomaterials.[4]

One of the most promising nanomaterials studied extensively over the past decades are single-walled carbon nanotubes (SWNTs). Their cylindrical, tube-like arrangement of carbon atoms, with diameters of a few nanometers and lengths of a few micrometers, gives rise to exceptional charge transport properties, high tensile strength and chemical stability.[5] Harnessing this almost perfect set of properties for real-world applications, however, remains a technological challenge. A fundamental issue is the statistically mixed synthesis of metallic (33 %) and semiconducting (67 %) nanotube species in every production process. Decades of research have addressed this problem and several post-synthesis purification and sorting methods have been established.[6] One of the most successful sorting methods is selective polymer-wrapping with conjugated polymers, yielding up to monochiral semiconducting nanotube dispersions in organic solvents.[7] These purified dispersions can be solution processed, for example *via* printing techniques to form SWNT networks.[8] Using such SWNT networks has led to many reports of high-performance field-effect transistors utilizing various device architectures (also electrolyte-gated and on flexible substrates)[9,10] and even to the realiza-

tion of a 16-bit microprocessor.[11]

While providing purified semiconducting SWNT dispersions for high quality (opto)electronic devices, the polymer-wrapping technique introduces the respective conjugated polymer as an additional parameter. The influence of the polymer onto the SWNT networks in terms of charge transport or charge injection, as well as the impact onto other components in a system, for example an electrolyte, have to be considered.[12] Although polymer-wrapped SWNT networks were successfully employed as a semiconductor for the development of sensing applications in aqueous electrolytes (biosensing),[13–15] their performance was always inferior to alternative materials.[16] The main reason for this is the hydrophobicity of commonly used wrapping-polymers, which prevents the full hydration of SWNT networks and leads to inefficient gating.

In general, SWNT films are highly suitable for electrolyte-gated applications due to their porous morphology, which has been demonstrated in combination with ionic liquids or ion-gels in various reports.[10,17] An emerging research field where the excellent material properties of SWNTs and the ion dynamics in electrolyte-gated networks of them could excel is neuromorphic computing and the development of artificial synapses.[18,19] Currently, this new topic is headed by electrochemical transistors with conductive polymers, however many materials and approaches are under investigation, each offering different benefits.[20,21]

In this work, the limitations of polymer-wrapped SWNT networks in transistors with aqueous electrolytes are overcome by attaching hydrophilic side chains onto the SWNTs by the exchange of the wrapping-polymer. By this means, polymer-wrapped SWNTs are shown to be a viable alternative to other active materials for bioelectronic components. Moreover, artificial synapses based on the slow ion diffusion in dense SWNT networks, capable of emulating typical synaptic mechanisms, are demonstrated. This device concept is further evaluated for the application in neuromorphic computing and first development steps into this direction are presented.

In the following, the structure of this thesis is outlined:

Chapter 2 explains the theoretical principles and gives an overview of the current research state relevant for the findings in this work. The structure of SWNTs as well as their electronic and optical properties are summarized and purification and functionalization techniques are

introduced. The working principles of unipolar and ambipolar field-effect transistors are described and the specific properties of SWNT network transistors and electrochemical transistors are highlighted. The last part of this chapter gives a brief overview of the components and mechanisms in the human brain and introduces the concepts of artificial synapses and neuromorphic devices from the field of brain-inspired computing.

Chapter 3 contains all details about the employed materials, sample preparation and characterization techniques, with the emphasis on aerosol-jet printing and spray-coating.

Chapter 4 demonstrates highly efficient water-gated electrochemical transistors through the functionalization of polymer-wrapped (6,5) SWNTs with hydrophilic ethylene glycole side chains. The functionalization is achieved non-covalently by exchanging the wrapping-polymer with the corresponding side chain. The impact of the hydrophilicity on the water-gating efficiency is studied by *in situ* photoluminescence spectroscopy under bias. Electrochemical transistors with networks of functionalized and reference SWNTs are characterized and compared to state-of-the-art materials.

In chapter 5 the slow ion diffusion in thick and dense SWNT networks is investigated and employed to fabricate artificial synapses. Biological computation and learning mechanisms such as short-term and long-term plasticity as well as spike-timing-dependent plasticity are observed. Finally, a controlled potentiation and depression of the synapses is shown when operated with optimized voltage pulses and the viability and remaining challenges for the use as neuromorphic device is discussed.

The final chapter 6 summarizes the achievements of this dissertation and discusses the open questions that could be the subject of future research.

Chapter 2

Background

This chapter discusses the fundamental properties of SWNTs, the functionality of field-effect transistors and in particular electrochemical transistors and introduces the basic principles of brain-inspired computing.

2.1 Single-Walled Carbon Nanotubes

Covering the full range of low-dimensionality, nanocarbon allotropes have been investigated in great detail over the last decades, not only to research quantum effects in different degrees of quantum confinement but also for their application in (opto)electronic devices.[22] From zero-dimensional fullerenes,[23] to one-dimensional carbon nanotubes[24] and two-dimensional graphene,[25] all three types of nanomaterials are composed of solely sp^2-hybridized carbon atoms. The highly ordered and periodic carbon lattices lead to astounding mechanical but also electrical and optical properties, that are highly desirable for many applications. Single-walled carbon nanotubes (SWNTs) in contrast to multi-walled carbon nanotubes, which are concentrical stacks of single-walled carbon nanotubes, feature well-defined optical and electronic transitions and are thus of greater interest in research. In the following sections, the structure of SWNTs and the implications for their electronic and optical features are elaborated. Furthermore, polymer-wrapping as highly efficient purification method to obtain selective semiconducting (6,5) SWNTs is explained and in connection to that, polymer exchange is discussed as an efficient, non-covalent functionalization technique.

2.1.1 Structural Properties

Sharing the same hexagonal carbon lattice, graphene sheets and carbon nanotubes are very similar in terms of their exceptional mechanical strength, high charge carrier mobilities along the lattice and their vibrational modes.[26,27] Therefore, a straight forward structural description of SWNTs is based on the concept of rolling up a graphene sheet as illustrated in Figure 2.1. While graphene itself has no bandgap, the periodic boundary conditions for electronic wavefunctions along the lattice change drastically depending on the roll-up angle and diameter of the resulting nanotube, leading to metallic but also semiconducting SWNT species. Defined as the linear combination of the two unit vectors of the carbon bravais lattice $\boldsymbol{a_1} = \frac{a}{2} \cdot (\sqrt{3}, 1)$ and $\boldsymbol{a_2} = \frac{a}{2} \cdot (\sqrt{3}, -1)$, with a lattice constant of $a = 0.246\,\mathrm{nm}$,[28] the chirality vector $\boldsymbol{C_h}$ – also termed roll-up vector – defines the nanotube circumference:

$$\boldsymbol{C_h} = n \cdot \boldsymbol{a_1} + m \cdot \boldsymbol{a_2} \tag{2.1}$$

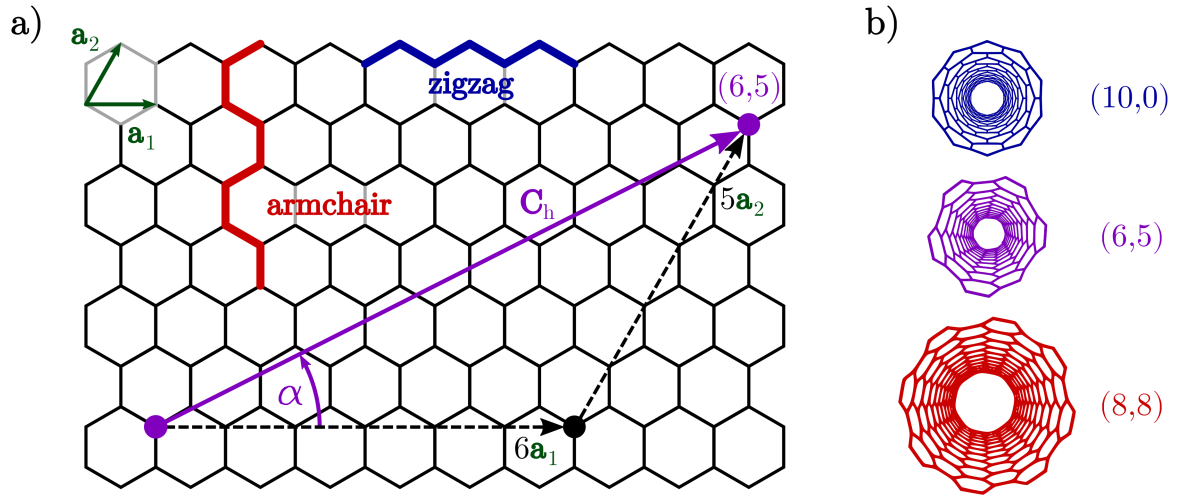

Figure 2.1: Structural description of SWNTs based on the roll-up formalism of graphene a) Hexagonal graphene lattice with the definition of the chiral vectors and the rolling direction for a (6,5) SWNT. b) Frontal view of a *zigzag* (10,0), a chiral (6,5) and an *armchair* (8,8) SWNT.

The two integers (n,m) are called chiral indices, giving the different SWNT species their unique name or *chirality*. Expressed by the chiral indices, the diameter d_t is given by

$$d_\mathrm{t} = \frac{|\boldsymbol{C}_\mathbf{h}|}{\pi} = \frac{a}{\pi}\sqrt{n^2 + nm + m^2} \tag{2.2}$$

and the chiral angle α, spanning between $\boldsymbol{a_1}$ and $\boldsymbol{C_h}$, is given by

$$\cos\alpha = \frac{2n+m}{2\sqrt{n^2+nm+m^2}}. \tag{2.3}$$

SWNTs are divided into achiral and chiral species, where the two achiral cases with $m = 0$ ($\alpha = 0°$) and $m = n$ ($\alpha = 30°$) are called *zigzag* SWNTs and *armchair* SWNTs, respectively. All other cases ($0° < \alpha < 30°$) are referred to as chiral. Typically, diameters of SWNTs range between (0.5–3 nm), while tube lengths of microns up to centimeters are possible,[29] depending on the method of synthesis. Due to the large aspect ratio, SWNTs are approximated and modeled as one dimensional and infinitely long.

2.1.2 Electronic and Optical Properties

Similarly to the structural properties, the electronic properties of SWNTs can be derived from a virtually rolled up graphene sheet. The band structure of graphene is commonly

derived using the nearest-neighbor tight-binding model.[30] As already touched upon, the additional periodic boundary conditions in cylindrical SWNTs, restrict the possible wave functions of graphene, such that only the following discrete wave vectors are allowed (zone-folding approximation),[28,31]

$$|\boldsymbol{K}_\mathbf{c}|j = \frac{2\pi}{|\boldsymbol{C}_\mathbf{h}|}j, \tag{2.4}$$

where $|\boldsymbol{K}_\mathbf{c}|$ denotes the wave vector in circumferential direction and j being an integer, ranging from zero to the maximum number of carbon hexagons per unit cell.

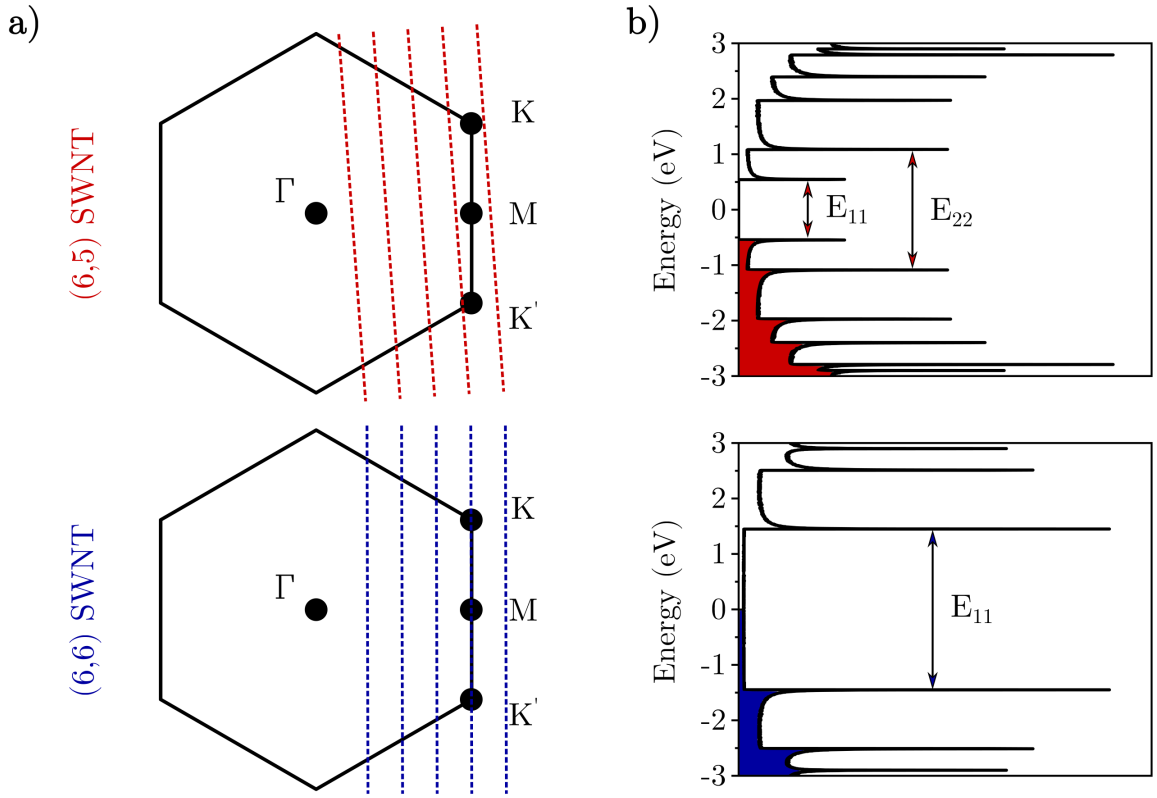

Figure 2.2: Density of states calculation following the zone-folding formalism for semiconducting (6,5) SWNTs (top, red) and metallic (6,6) SWNTs (bottom, blue). a) Schematic illustration of the allowed wave vectors as cuts (dashed lines) through the Brillouine zone of graphene and its symmetry points. Note that the spacing between the lines and their length depends on the chirality and is not to scale. b) Resulting DOS distribution with allowed optical transitions (E_{11} and E_{22}). All occupied states are colored, highlighting the formation of a bandgap for the semiconduting (6,5) SWNTs and the nonzero density of states of the metallic (6,6) SWNT at the Fermi energy. The data was taken from reference 32.

In reciprocal space, these discrete wave vectors appear as cuts through the first Brillouin zone of graphene, which translate into sharp singularities in the electronic density of states

(DOS) called van Hove singularities, as illustrated in Figure 2.2. If cuts through the graphene Brillouin zone intersect the K- or K'- point – the zero-bandgap (Dirac) points where valence and conduction band of graphene touch – the corresponding SWNT is metallic. Vice versa, if the Dirac points are not part of the SWNTs band structure it is semiconducting. The band structure is directly determined by the chiral indices, such that all metallic SWNTs without a bandgap fulfill the condition $(m-n)\mathrm{mod}(3) = 0$, whereas all semiconducting SWNTs have $(m-n)\mathrm{mod}(3) = 1, 2$. The bandgap of semiconducting SWNTs ranges between 0.5–1.5 eV and scales inversely with their diameter.[33]

As the band structure of semiconducting SWNTs features direct band gaps the formation of excitons by optical excitation and photoluminescense can be observed. Owing to their antenna like one-dimensional shape, SWNTs exhibit high polarization anisotropy, such that the polarizability longitudinal to the tube axis is significantly larger than transversal.[34] Thus, it is possible to analyze the alignment or orientation of SWNTs in a film with linearly polarized light (*e.g.* polarized Raman spectroscopy).[35] Due to the large difference in polarizability, the predominant optical features of SWNTs are restricted to the quantum mechanically allowed excitonic transitions related to excitations along the tube axis.[36] The possible transitions are depicted in Figure 2.2b and occur between subbands of the valence and conductance band of identical quantum number i, identified as E_{ii}. The diameter dependent and characteristic sharp optical peaks are used to analyze SWNT samples by standard UV-vis-NIR spectroscopy in the range of 300–3000 nm, as exemplified by a polymer-wrapped monochiral (6,5) SWNT dispersion in toluene in Figure 2.3. The diameter dependence of the different transition energies is summarized in the Kataura plot, which is used to determine the presence of SWNT species in a sample by spectroscopic techniques (like UV-vis-NIR or Raman spectroscopy).[37]

The optical excitation of a nanotube can occur at arbitrary subband transitions and their specific wavelengths, however luminescent emission is only detectable for the lowest E_{11} transition, due to non-radiative relaxation of the excitons. Hence, photoluminescence excitation and emission maps are a usefull tool for sample analysis giving a more detailed overview of the optical features and being less prone to overlapping peaks.[38]

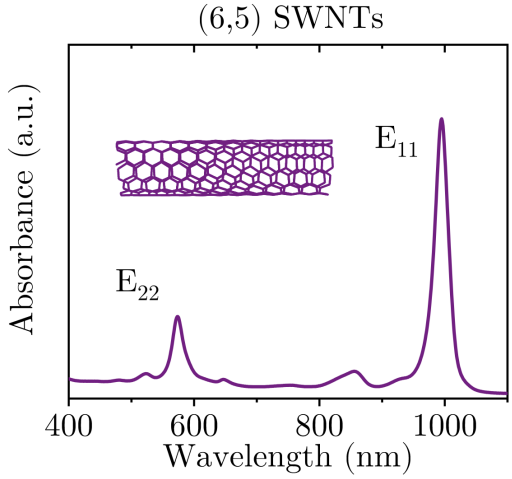

Figure 2.3: Baseline corrected UV-vis-NIR absorption spectrum of a monochiral (6,5) SWNT dispersion in toluene produced by polymer-wrapping. The sharp peaks are assigned to the characteristic optical transitions E_{11} and E_{22}.

Another integral analytic tool to investigate SWNT samples is resonant Raman spectroscopy, which is an experimental technique to study vibrational modes stimulated by inelastic light scattering. This technique offers remarkable sensitivity towards different SWNT chiralities because matching the excitation wavelengths and the excitonic transition energies of a particular nanotube species result in resonantly enhanced vibrational modes. The signal enhancement in contrast to non-resonant modes even allows to unambiguously detect single SWNTs.[39,40] With excitation wavelengths lying in the visible range for SWNTs with diameters up to 2 nm, standard laser wavelengths can be utilized and chosen depending on the sample. Characteristic Raman modes are shown in Figure 2.4, again exemplary for (6,5) SWNTs.

The Raman modes corresponding to outward and inward vibrations in radial direction of the SWNTs are called radial breathing mode (RBM) and are found between 100–350 cm^{-1}. The wavenumbers of this mode scale antiproportional with the tube diameter, hence valuable information about the chirality composition of a nanotube sample can be drawn from the RBM peak positions. The intensity of the D-mode ranging from 1300–1350 cm^{-1} originates from defects or impurities in the sp^2 carbon lattice and is therefore a measure for the structural integrity of SWNTs. It is used to evaluate the progress of functionalization.[41] All vibrations within the lattice plane in the range from 1500–1600 cm^{-1} are summarized as G-modes with the notation G^+, G^- and E_2 for the modes related to displacements along the

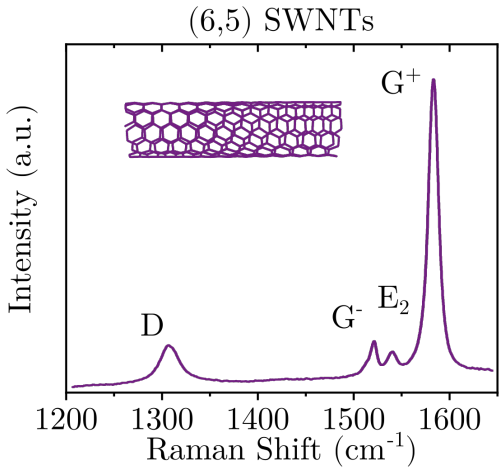

Figure 2.4: Exemplary Raman spectrum of polymer-wrapped (6,5) SWNTs dopcast on aluminum showing the D-mode and G-modes (excitation wavelength 532 nm).

tube axis, perpendicular to the tube axis and in both directions. Due to the structural similarity, the D-mode and G-modes also occur in graphene, while the RBM-mode only appears in SWNT spectra. The fact that all peak positions and intensities of the Raman modes change drastically for charged SWNTs, additionally renders resonant Raman spectroscopy a powerful tool to study electrostatic or (electro-)chemical doping.[42–44]

The unique band structure of SWNTs not only leads to interesting optical properties but also exceptional electronic properties and in particular outstanding charge transport. The almost symmetric band structure and thus similar effective masses of both electrons and holes in combination with efficient charge injection from typical electrode metals (*e.g.* gold) results in ambipolar charge transport, making SWNTs suitable for optoelectronic devices like light-emitting field-effect transistors (LEFETs).[45,46] Unipolar charge transport can be achieved by efficient contact engineering (use of low/high work function metals) and contact doping,[47] or occurs naturally from p-doping in ambient air due to adsorption of oxygen and water.[48,49]

In a single nanotube at room temperature the charge carrier mobility – quantifying the velocity of a particle in a given electric field – of both holes and electrons reach outstanding values of several thousand $\mathrm{cm^2\,V^{-1}\,s^{-1}}$. The peak mobility μ_{peak} scales quadratically with the nanotube diameter d_{t} and is antiproportional to temperature T, due to reduced electron-phonon scattering at low temperatures, typical for band transport:[50,51]

$$\mu_{\text{peak}} = 0.48 \frac{e\nu_0}{\hbar\alpha} \frac{d_t^2}{T} \tag{2.5}$$

In this empirical equation ν_0 denotes the Fermi velocity of graphene, $\hbar$ the reduced Planck constant and $\alpha = 12\,\text{m}\,\text{K}^{-1}\,\text{s}^{-1}$ is an empirical coefficient.[51]

The carrier density in combination with the sharp van Hove singularities of SWNTs has a strong influence on the carrier mobility. Increasing the carrier density, for example by increasing the gate voltage in a field-effect transistor (FET), first leads to higher mobility values until the first subband is filled. When the Fermi level rises to the second subband with lower conduction velocity, the mobility decreases with increasing electric field (negative differential mobility),[50,52] giving rise to a peak mobility. Another important factor that directly follows from the one dimensional DOS distribution is the quantum capacitance of SWNTs.[53] Due to the Pauli exclusion principle and the fact that electrons can only be added to available quantum states above the Fermi energy, there is a limited number of available electron states apart from the van Hove singularities.[54] This is reflected by the small quantum capacitance for the occupation of the first subband of a semiconducting nanotube of roughly $0.4\,\text{fF}\,\mu\text{m}^{-1}$.[54,55] In fact, due to being so small, the quantum capacitance dominates the total interfacial capacitance of a nanotube in an electrical device, as it is connected in series and added reciprocally to much larger capacitances like the geometric gate capacitance or the even larger double layer capacitance in electrolyte gated systems, as explained later (see equation (2.18)).[56] In SWNT network transistors also the network density has to be taken into account to not overestimate the capacitance with the basic plate capacitor approximation.[5,57] Therefore, direct capacitance measurements on individual devices should be performed for reliable results.[58]

A detailed theoretical understanding of charge transport in individual SWNTs has been achieved since the beginning of nanotube research.[59] However, employing SWNTs as active material for optoelectronic applications is usually done with two dimensional or even three dimensional networks with random orientation and numerous nanotube junctions, where comprehensive theoretical studies are still missing. Fundamentally, the formation of SWNT networks and the resulting charge transport is well described by percolation theory.[60] However, for a deeper understanding, experimental studies with semiconducting SWNT networks

were missing for a long time, due to the lack of purification methods and the influence of metallic chiralities.[61] Thanks to the advances in chirality sorting and purification techniques of SWNT material, studies on transistors with purely semiconducting nanotube species and high on-off-rations are possible nowadays, which have contributed immensely to unravel the complex correlations in nanotube networks.[62–65]

The charge transport in randomly oriented semiconducting SWNT networks is governed by the inefficient hopping of charges across nanotube-nanotube junctions and the highly efficient transport along the tubes.[66,67] In this context, the high-resistance inter-nanotube transport is the limiting factor, reducing the extraordinary charge carrier mobilities of single nanotubes by orders of magnitude to roughly 0.1–100 $\mathrm{cm^2\,V^{-1}\,s^{-1}}$,[68] which is still high in comparison to many other materials used for organic electronics.[69] Bundles and aggregates of SWNTs are detrimental for charge transport as they promote scattering and their formation during device fabrication should be suppressed.[67,70] On the other hand, the influence of dispersion stabilizing surfactants or residual wrapping-polymers on the charge transport in SWNT is still under investigation.[71,72]

More insight into the charge transport and mobility in random SWNT networks of different chiralities has been drawn from temperature dependent measurements.[64,65,73] Although band transport within the nanotubes becomes more efficient with decreasing temperature, the overall mobility drops, due to a reduction in the temperature activated charge hopping process across junctions. Neither the variable-range hopping model,[74] nor the fluctuation-induced tunneling model[75] were able to describe the observations entirely across the full temperature range.[64,65,76]

Computational models for the description of charge transport in semiconducting nanotube networks have been developed in the recent past,[77] using the Master equation approach where only the nanotube junctions were taken into account and considered as resistors.[78,79] Creating a virtual box of randomly oriented sticks with a predefined density, the resulting random resistor network was analyzed by Kirchhoff's current law. Although several simplifications and assumption have been made, this model was able to describe experimental observations well. Improvements could be made by implementing the influences of temperature, intra-tube transport in relation to the nanotube diameter or three dimensional effects which were neglected so far.

While a lot of open questions remain about the charge transport in networks of semiconducting SWNTs, the understanding is detailed enough to draw conclusions for an ideal high-mobility SWNT network. To exploit the extraordinary intra-tube transport and suppress the influence of inefficient inter-tube transport as much as possible, an optimized network of semiconducting SWNTs consists of a dense array of long and aligned large diameter tubes of the same chirality[64] in parallel to the charge transport direction. A lot of progress has been made recently to accomplish the very challenging task of producing networks with these prerequisites and purely semiconducting SWNTs by developing highly elaborate fabrication techniques.[80]

2.1.3 Selective Dispersion by Polymer-Wrapping

There are several industrialized processes that are capable of synthesizing high quality SWNTs in large quantities, however all of them produce a mixture of metallic and semiconduction SWNTs. Carbon vaporization at elevated temperatures above 1000 °C with arc discharge,[24,81] laser ablation[82] or arc plasma jet[83] produce mostly large-diameter SWNTs with diameters of 1–3 nm. On the other hand, metallic catalyst assisted chemical vapor deposition (CVD) of carbon precursors in the gas phase yields smaller diameter ranges of around 0.7–1.2 nm. The most prominent examples are the HipCO® (high-pressure carbon monoxide) and CoMoCAT® (cobalt molybdenum catalyst) processes. Common carbon precursors are methane, ethane, ethanol or carbon monoxide and usually iron or cobalt/molybdenum are used as catalysts.

In order to use the SWNTs synthesized with the above mentioned processes for applications, the obtained mixtures of metallic and semiconducting species and impurities such as residual catalyst or different carbon allotropes have to be purified and sorted by chirality. This preparation is usually performed in organic solvents or aqueous media. Since the van der Waals forces between nanotubes promote aggregation and bundling, the SWNTs have to be dispersed by strong shear forces[7] or ultrasonication[84] and stabilized against re-aggregation. In aqueous dispersions colloidal stability is achieved by surfactants such as sodiumdodecylsulphate (SDS)[85] or cholates[86] and impurities can be removed via centrifugation. The obtained mixture of semiconducting and metallic SWNTs can be subsequently sorted using

various methods such as gel permeation chromatography,[87] density gradient ultracentrifugation,[86] aqueous two-phase extraction[88,89] or dielectrophoresis.[90]

A well-established process to produce highly selective dispersions with outstanding purity in organic solvents (toluene or xylenes)[91,92] is the polymer-wrapping technique, which was used in this thesis. This technique was first reported by Nish *et al.*[91] and is based on the selective wrapping of π-conjugated polymers around specific nanotube chiralities by simple dispersion of SWNT powders with the polymers in organic solvents. Several conjugated polymers have been explored in this context ranging from polyfluorenes, polyfluorene copolymers[91,93,94] and polythiophenes[95,96] to polycarbazoles.[97,98] The selectivity is directly determined by the structure of the polymer in combination with the SWNT raw material and the solvent.[96,99] The backbone of the polymer wraps preferentially around nanotube chiralities where the π-π-interactions are maximized, while the length of the alkyl-side-chains that provide the solubility, influences the favored nanotube diameters.[93,95] Even small deviations in the polymer structure have a strong impact on the selectivity, which can be seen when comparing dispersions of CoMoCAT® SWNTs sorted by PFO-BPy (polyfluorene with a bipyridine unit, see Figure 3.1) or PFO, yielding dispersions of preferentially (6,5) or (7,5) SWNTs, respectively.

The efficiency of the polymer-wrapping method is further influenced by temperature and the polarity and viscosity of the solvent,[100] which limits the choice of suitable solvents. The molecular weight of the polymer is also an important parameter with higher molecular weights resulting in greater yields however to the detriment of selectivity.[92]

After colloidal stabilization of purely semiconducting SWNTs, centrifugation is used to obtain a degree of purity that is feasible for the fabrication of transistors.[101] Since the conjugated polymers exhibit charge carrier mobilites that are orders of magnitude lower than those in SWNTs, it was for a long time a widely accepted and intuitive assumption that excess polymer had to be removed before device fabrication for example via vacuum filtration and washing with solvents.[11,102] However, this believe was recently challenged by Mirka *et al.*,[12] who found that up to an artificially high threshold of excess polymer a simple rinsing of deposited SWNT networks with solvents is sufficient to remove the excess polymer. Device fabrication with dispersions of higher polymer concentration profits from suppressed re-aggregation and especially printing techniques such as aerosol-jet-printing benefit also

from the higher viscosity. In this thesis, the combination of CoMoCAT® SWNT powder and PFO-BPy was employed, to yield an exceptional purity of monochiral (6,5) SWNTs well-suited for device fabrication or spectroscopic investigations (see chapter 3.2 for details).[101]

2.1.4 Functionalization

One of the great advantages of organic electronics in comparison to conventional technologies is the close connection to chemistry and its many tools to synthesize new or functionalize established materials depending on specific application requirements. Over the past decades of carbon nanotube research a large number of functionalization techniques has been developed to add new features, such as tailored optical transitions.[103–105] In general, functionalization describes the process of attaching functional groups to the nanotube surface and the developed methods can be categorized into covalent and non-covalent functionalization. Since the greatest weaknesses of SWNTs remain the poor solubility in aqueous and organic solvents and their tendency to form aggregates in dispersions, the vast majority of functionalization routes address these issues.[106–109]

An example of covalent functionalization, that has drawn great research interest over the last few years, is based on introducing sp^2-defects into the carbon lattice of SWNTs in a controlled manner.[110] These defects offer interesting new optical properties, such as single-photon emission at room temperature, and even lead to an increased photoluminescence quantum yield due to the localization of otherwise mobile excitons.[111] Although offering interesting optical features, covalent functionalization with sp^2-defects has a negative impact on the charge transport properties due to the disturbance of the π-system of the carbon lattice. Depending on the degree of functionalization this effect is not detrimental for applications of functionalized SWNTs in optoelectronic devices but results in lower charge carrier mobilities.[76]

The challenge of creating soluble or dispersable carbon nanotubes is commonly approached by non-covalent functionalization methods, which rely on the adsorption of surfactants or polymers through van der Waals interaction. In this way, SWNTs can be made solution-processable without disturbing the π-system of the hexagonal carbon lattice, preserving the desired electronic properties, as explained in the previous section. Reports in literature

have shown that it is possible to exchange the wrapping-polymer used to create stable and selective dispersions of SWNTs after the purification process to introduce new functionalities.[112] Although being weakly bound to the SWNT surface, an energy transfer between an adsorbed polymer and the nanotube is possible, rendering non-covalent functionalization an equally powerful tool to introduce new properties.[113] In a recent example, the selective wrapping-polymer that was used to create stable dispersion in toluene was exchanged by an amphiphilic polymer, which enabled SWNT dispersability with high purity levels in various organic solvents.[108]

In another example, optical memory elements based on random SWNT networks were fabricated by exchanging the original wrapping-polymer for a UV-light and temperature switchable one.[114] This way, the conductivity of the SWNT networks could be increased by exciting the wrapping-polymer with light pulses and decreased again by heating.

The commonly used wrapping-polymers that exhibit good selectivity are of hydrophobic nature, allowing stable dispersions in organic solvents. Utilizing the resulting highly purified SWNT dispersions in electrochemical transistors with aqueous electrolytes or in biological environments is possible but yields inferior device performance compared to other materials. This problem is addressed in chapter 4 by functionalizing SWNTs non-covalently with hydrophilic ethylene glycole side chains *via* polymer exchange.

2.2 Field-Effect Transistors

Field-effect transistors are the fundamental component of any electronic circuit, where they act as amplifiers or digital switches. Apart from the well-established inorganic materials, solution-processable semiconductors in combination with flexible substrates (*e.g.* plastics, paper or textiles) are investigated for exotic applications such as wearable[115] or edible electronics.[116] Due to the well understood device dynamics, FETs are also used to benchmark properties like charge injection and charge transport of new materials. Although the transistors fabricated in the later chapters of this thesis are electrolyte-gated devices with lateral instead stacked geometry, the general principles of FETs are derived for standard architectures to simplify matters. After introducing the basics, special emphasis is laid on SWNT networks as semiconducting channel material and the specifics of electrochemical transistors.

2.2.1 Basic Principles

Standard FETs are composed of a semiconductor, a dielectric and three electrodes – or terminals – referred to as source (S), drain (D) and gate (G). One possible arrangement of these components is depicted in Figure 2.5, where the semiconductor is connecting the source and drain electrodes but is separated from the gate electrode by the insulating dielectric layer. The area between the source and drain electrodes is called the channel and is defined by the width (W), which is the extension of the electrode in parallel direction, and the length (L), denoting the separation of the electrodes. Besides the bottom-contact/top-gate configuration depicted in Figure 2.5, top-contact/top-gate, top-contact/bottom-gate or bottom-contact/bottom-gate architectures are employed, depending on the fabrication routes of different materials and the final applications. Regardless of the architecture, the operating principle is based on the accumulation of charges at the interface between the dielectric and the semiconductor to form a conductive channel.

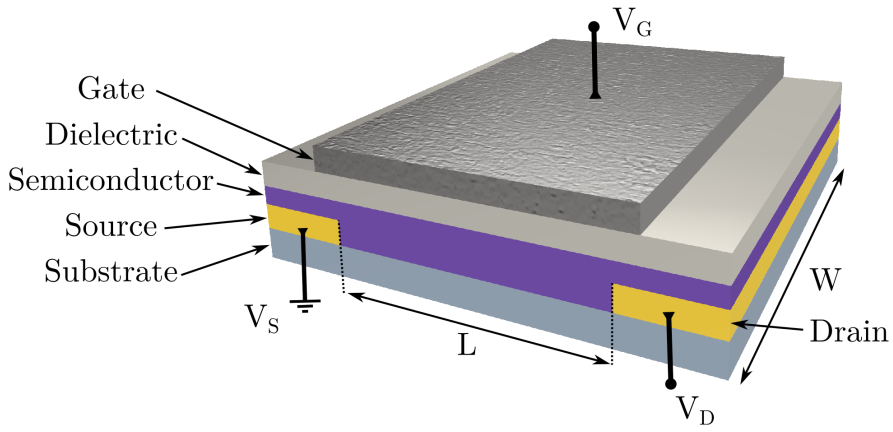

Figure 2.5: Schematic representation of a bottom-contact/top-gate FET architecture consisting of a gate, source and drain electrode, a semiconducting layer and a dielectric. The channel geometry is defined by the length L and the width W.

For an undoped semiconductor and no applied voltages the transistor is in its *off*-state. Charge accumulation in the semiconductor is achieved by creating an electric field across the dielectric by applying a gate voltage (V_G) between the gate and the grounded source electrode. If V_G is large enough to induce mobile charges a directed current (I_D) can flow by applying an additional electric field between the source and the drain electrode (V_D) and the transistor switches to the *on*-state. Up to a certain threshold voltage (V_{th}) at the gate,

the induced charges are immobile and occupy trap states, that are present at interfaces or caused by defects and impurities in the semiconductor. Depending on the insulation quality of the dielectric a marginal current flows between the source and gate electrode (I_{G}), which is called leakage current and should be ideally several orders of magnitude lower than I_{D}.
As long as the lateral electric field between source and drain is significantly lower than the gating electric field, which is approximately given for dielectrics thinner than a tenth of L, the position-dependent potential ($V(\mathrm{x})$) in the transistor channel can be described by the gradual channel approximation,[117,118] where x ranges from zero at the source electrode ($V(0) = 0$) to L at the drain electrode ($V(L) = V_{\mathrm{D}}$). For the amount of mobile charges that are induced by a gate voltage exceeding V_{th} it follows:

$$Q_{\mathrm{mobile}} = C'(V_{\mathrm{G}} - V_{\mathrm{th}} - V(x)) \tag{2.6}$$

Where C' is the areal capacitance of the dielectric. By applying Ohm's law and neglecting diffusion, the drain current reads

$$I_{\mathrm{D}} = W\mu Q_{\mathrm{mobile}} E_{\mathrm{x}}, \tag{2.7}$$

with the charge carrier mobility μ and the electric field E_{x} at position x. By merging equations 2.6 and 2.7, writing the electric field in its differential form $E_{\mathrm{x}} = \dfrac{\mathrm{d}V}{\mathrm{d}x}$ and solving the differential equation by separation of variables the drain current is defined by

$$I_{\mathrm{D}} = \frac{W}{L}\mu C' \left[(V_{\mathrm{G}} - V_{\mathrm{th}})V_{\mathrm{D}} - \frac{1}{2}V_{\mathrm{D}}^2\right]. \tag{2.8}$$

In this step, the charge carrier mobility was approximated as independent from the carrier density.
A transistor can be operated in two distinct regimes, the linear regime and the saturation regime. In the linear regime, where the drain voltage is smaller than the effective gate voltage $V_{\mathrm{G}} - V_{\mathrm{th}}$, the carrier density scales linearly with increasing $V(x)$, as illustrated in Figure 2.6a. Since the quadratic term in equation (2.8) can be neglected, the current in the linear regime also scales linearly with V_{D}:

$$I_{\mathrm{D,lin}} = \frac{W}{L}\mu_{\mathrm{lin}}C'(V_{\mathrm{G}} - V_{\mathrm{th}})V_{\mathrm{D}}. \tag{2.9}$$

The saturation regime on the other hand commences when V_{D} surpasses the effective gate voltage ($V_{\mathrm{D}} \geq V_{\mathrm{G}} - V_{\mathrm{th}}$), at which point the channel is pinched off, as shown in Figure 2.6b. Due to the increasing depletion region the drain current saturates and becomes independent of V_{D}, which can be seen by substituting V_{D} with $V_{\mathrm{G}} - V_{\mathrm{th}}$ in equation (2.8):

$$I_{\mathrm{D,sat}} = \frac{W}{2L}\mu_{\mathrm{sat}}C'(V_{\mathrm{G}} - V_{\mathrm{th}})^2. \tag{2.10}$$

It follows, that the square root of $I_{\mathrm{D,sat}}$ scales with the gate voltage. Therefore, the threshold voltage is commonly determined by plotting the square root of the saturation current against the gate voltage, extrapolating linearly at the maximum of the first derivative and extracting the intersection of this extrapolation with the x-axis. A small V_{th} is beneficial for low voltage operation and power consumption and can be tuned *via* doping. A similar parameter is the onset voltage (V_{on}), which marks the gate voltage that is needed for the drain current to exceed the leakage current. The extraction of V_{th} in real FETs can be inaccurate due to the presence of trap states, hence in practice, comparing the onset voltage can be a more reliable tool in some cases.[119]

Basic electrical characterization of FETs involves gate voltage sweeps at constant drain voltages and drain voltage sweeps at constant gate voltages. The transistor metrics are commonly extracted from two graphical representations of the measured drain currents, which are called output and transfer characteristics as shown in Figure 2.6c and d. For the output characteristics, the drain current is plotted against the drain voltage at different constant gate voltages. This way, the transition between the linear and the saturation regime and the corresponding voltage ranges can be assessed. Furthermore, any deviations from the linear behavior at low drain voltages provides information about injection barriers at the interface between contact electrodes and semiconductor. Transfer characteristics are commonly semi-log plots of the drain current against the gate voltage at different constant drain voltages. This graphical representation enables assessment of the switching behavior of the transistor in detail. For a preferentially high on/off-current ratio above 10^6, a high on-current I_{on} and a low off-current I_{off} are important and can be directly extracted from the graph.

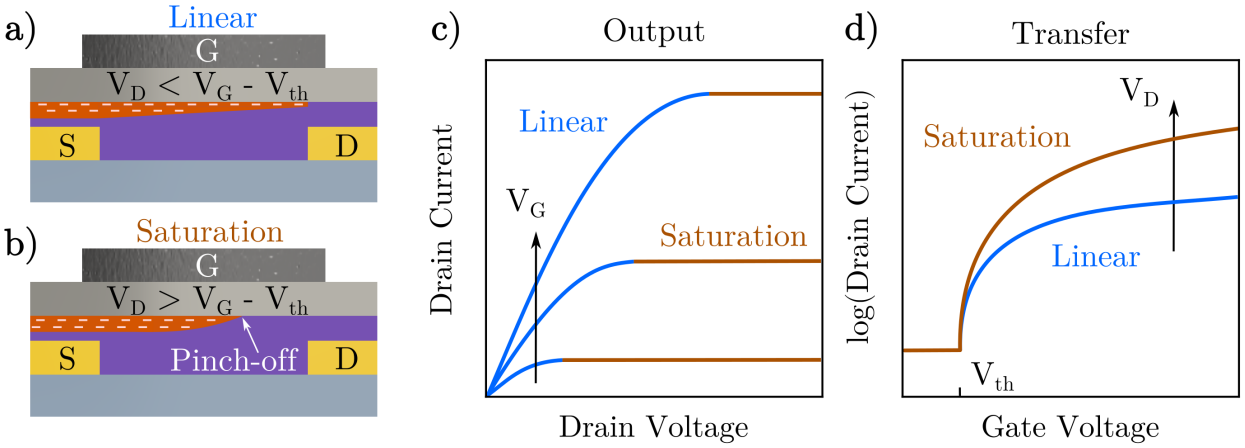

Figure 2.6: a) Illustration of the accumulated electrons in the channel of a unipolar n-type FET when operated in the linear regime (blue) and b) in the saturation regime (orange). c) Ideal output characteristics for three gate voltages, showing the transition from the linear to the saturation regime with rising drain voltage. d) Corresponding ideal transfer characteristics in both operation regimes.

Additionally, the most fundamental parameter of a FET[117] – the transconductance g_m – is represented by the slope of the transfer curve and thus quantifies the modulation of the drain current with respect to the gate voltage:

$$g_m = \frac{\partial I_D}{\partial V_G} \tag{2.11}$$

Together with Equations 2.9 and 2.10 the expressions for the linear and saturation regime read

$$g_{m,lin} = \frac{W}{L}\mu_{lin}C'V_D \tag{2.12}$$

and

$$g_{m,sat} = \frac{W}{L}\mu_{sat}C'(V_G - V_{th}). \tag{2.13}$$

With 2.9 and 2.10, rearranging the above expressions yield the equations in the two operation regimes to extract the arguably most important quantity for a transistor material, the charge carrier mobility:

$$\mu_{\mathrm{lin}} = \frac{L}{WC'V_{\mathrm{D}}} g_{\mathrm{m,lin}} \tag{2.14}$$

and

$$\mu_{\mathrm{sat}} = \frac{L}{WC'} \frac{\partial^2 I_{\mathrm{D,sat}}}{\partial V_{\mathrm{G}}^2}. \tag{2.15}$$

The two values for the linear and saturation mobility are equal for an ideal FET, however in reality the linear mobility is often lowered by the influence of contact resistance.[120] The contact resistance is the sum of the two resistances at the source and drain electrode, which correspond to the injection barriers between the electrode material and the semiconductor. These injection barriers depend on the work functions and the alignment of the energy levels of the two components. For small injection barriers and thus low resistance, the contact is classified as *ohmic* and the drain current scales linearly with the drain voltage in the linear regime. *Non-ohmic* contacts lead to S-shape output characteristics at low drain voltages, which affects the device performance negatively.

2.2.2 Ambipolar Field-Effect Transistors

The basic description of a FET above holds true only for a purely n-type or p-type transistor, where either a conducting hole or electron channel can be induced into the semiconductor. SWNTs on the other hand are able to conduct both holes and electrons, leading to ambipolar device characteristics, which are explained in this section.

Depending on the applied voltages, accumulation of electrons and holes in the semiconductor can occur simultaneously, where the electrons are injected from the source and the holes from the drain electrode, as depicted in Figure 2.7a. This ambipolarity has a drastic effect on the transfer and output characteristics compared to the unipolar case, as can be seen in Figure 2.7b and c. On the left hand side of the transfer curves a unipolar hole transport (green) can be observed for positive drain voltages as well as $V_{\mathrm{G}} - V_{\mathrm{D}} < V_{\mathrm{th,h}}$ and $V_{\mathrm{G}} < V_{\mathrm{th,e}}$. The linear regime of this hole transport is observed for $V_{\mathrm{G}} < V_{\mathrm{th,h}}$ and the saturation regime for $V_{\mathrm{th,h}} < V_{\mathrm{G}} < V_{\mathrm{th,e}}$.

By increasing the gate voltage above $V_{\mathrm{th,e}}$, while $V_{\mathrm{G}} - V_{\mathrm{D}} < V_{\mathrm{th,h}}$ is still given, the FET

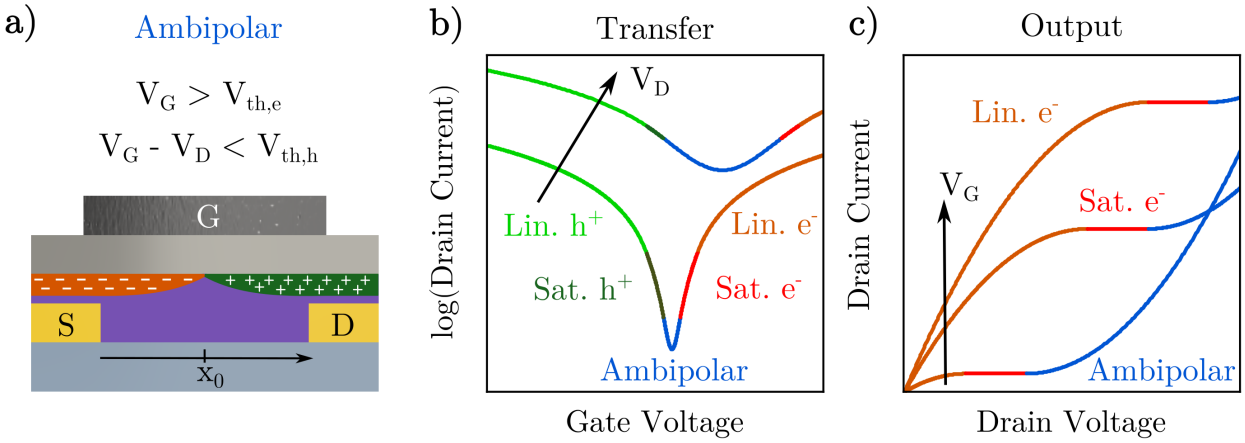

Figure 2.7: a) Illustration of the accumulated electrons (orange) and holes (green) in the channel of an ambipolar FET when operated in the ambipolar regime. b) Ideal transfer characteristics for two positive drain voltages and equal hole and electron mobilities. c) Output characteristics for positive drain voltages and three different positive gate voltages. The colors in b) and c) stand for the linear and saturation regime of holes (light and dark green), the ambipolar regime (blue) and the linear and saturation regime of electrons (orange and red).

undergoes the transition to the ambipolar regime (blue). From this point on, both charge carriers are injected into the semiconductor from opposite sides forming a recombination zone of vanishing charge carrier density where they meet.

The drain current for an ambipolar transistor is the superposition of the two currents from both charge carriers and can be calculated by

$$I_{\mathrm{D}} = \frac{W}{2L} C \left(\mu_{\mathrm{e}} (V_{\mathrm{G}} - V_{\mathrm{th,e}})^2 + \mu_{\mathrm{h}} (V_{\mathrm{G}} - V_{\mathrm{D}} - V_{\mathrm{th,h}})^2 \right). \tag{2.16}$$

Upon further increase of the gate voltage, pure electron accumulation and transport is achieved, first in the saturation regime (red), for $V_{\mathrm{th,e}} > V_{\mathrm{G}} - V_{\mathrm{D}} > V_{\mathrm{th,h}}$ and finally in the linear regime (orange) for $V_{\mathrm{G}} - V_{\mathrm{D}} > V_{\mathrm{th,e}}$. From the equations and the transfer characteristics above, it becomes clear that the position of the recombination zone and the ambipolar current is directly dependend on V_{D}, which is best seen in the output characteristics (Figure 2.7c). In contrast to the unipolar case, a steep current increase is observed after the plateau of the saturation regime, due to the concurrent injection of opposite charge carriers at sufficiently high drain voltages. Since the recombination of electrons and holes inside semiconductors can be of radiative nature, termed electroluminescence (EL), materi-

als that exhibit ambipolar charge transport are particularly interesting for the fabrication of LEFETs[45,46,121–123] or for the understanding of the fundamental physics of excitons and trions.[124,125] However, logic circuits with low power dissipation require purely n-type and purely p-type devices, which can be achieved by doping.[47,126,127]

2.2.3 Single-Walled Carbon Nanotube Network Transistors

A lot of research has been dedicated towards the development of electronic devices with semiconducting SWNTs as the active layer, ranging from FETs[9,128–130] and integrated circuits[131,132] to sensors[13,14] and neuromorphic devices.[133,134] In order to harness the outstanding mechanical and electronic properties that individual SWNTs show in theory, new device architectures and SWNT processing methods are constantly developed. Over the last decades, SWNTs have been successfully implemented in transistors either as single SWNTs, as arrays of SWNTs or as SWNT networks. In this section, a recap of the recent progress in the field together with open problems and challenges is given.

FETs with sub 10 nm channels using single SWNTs were successfully fabricated and showed extraordinary current density and energy efficiency even surpassing comparable silicon devices.[135] Naturally, the fabrication of such devices requires extremely expensive and time-consuming contacting of single SWNTs *via* electron beam lithography, which lacks reproducibility and scalability.[136,137]

Growing aligned and dense SWNT arrays directly onto substrates[138–140] offers much cheaper fabrication in comparison. Unfortunately, so far there has been no advances in the field which would allow selective growth of solely semiconducting SWNTs. Nonetheless, examples with on/off current ratios of 10^5, charge carrier mobilities of up to thousands of $cm^2\,V^{-1}\,s^{-1}$ and large on-currents have been demonstrated.[141] Creating aligned SWNT arrays or networks of semiconducting nature from purified dispersions using self-assembly techniques that are driven by the evaporation or flow of solvents[142] or by vacuum filtration[143], has also been shown to yield exceptional device performance and recent progress has pushed the scalability to the wafer scale.[80] Still the transformation to industrialization remains a challenge, since the fabrication involves several elaborate processing steps, that so far have only been shown under laboratory conditions. Another way to achieve nanotube alignment in chan-

nel direction is *via* dielectrophoresis, which is an electric field assissted alignment method using prepatterned electrodes. For short-channel devices, which are more prone to metallic impurities on/off current ratios of up to 10^4 were achieved,[144] while for longer channels a ratio of up to 10^7 is possible.[145] The cheapest and easiest deposition techniques of SWNTs result in randomly aligned networks. The most prominent examples are drop-casting,[146] dip-coating[147,148] or spin-coating,[9] all relying on photolithografic patterning, or localized printing techniques such as ink-jet,[149] aerosol-jet[8] or gravure printing[150]. The advantage in processability comes at the price of lower charge carrier mobilities compared to the above mentioned approaches. Typical values range between 1–100 $\mathrm{cm^2\,V^{-1}\,s^{-1}}$, which is still sufficient for applications such as active-matrix OLED backplanes. Thus, the performance is readily comparable to polycristalline silicon or solution-processable metal oxide semiconductors.[151] So far, SWNT network FETs have been shown to provide low-voltage operation with high switching speeds even on flexible substrates.[152–154] Advances in p-doping and n-doping of SWNT networks have reached a level where basic complementary circuits[126,127] and even more elaborate applications like a 16-bit microprocessor have been reported.[11]
In addition to the standard FET architectures listed above, SWNT networks also represent a highly suitable semiconducting material for the use in electrolyte-gated systems,[15] where their porous nature allows the infiltration of electrolyte ions, leading to volumetric gating. In that sense, electrolyte-gated SWNT networks also belong to the field of electrochemical transistors (ECTs), which are discussed in the following section.

2.2.4 Electrolyte-Gated and Electrochemical Transistors

Instead of a solid dielectric as introduced in the previous sections, FETs can also be operated using electrolytes with mobile ions instead, leading to the device class of electrolyte-gated field-effect transistors (EG-FETs). Typical electrolytes are ionic liquids, which are liquid salts, ion-gels (ionic liquids that are mixed with a polymer) or aqueous solutions with various dissolved salts. Electrolyte-gating enables different device architectures, such as a side-gate configuration as schematically shown in Figure 2.8. Although the basics derived previously for standard FETs are still valid for EG-FETs, the charge accumulation follows a different principle. Whereas the dielectric and most crucially its thickness determines the capacitance

in standard FETs, the capacitance in EG-FETs is governed by the formation of nanometer thick electric double-layers of ions and compensating charges at the interface between electrolyte and semiconductor upon gating. Due to the close proximity of the charges, electric double-layer capacitances C_{dl} are orders of magnitude larger than capacitances of solid dielectrics.

A special type of electrolyte-gated transistors is the electrochemical transistor, whose active semiconducting layer is permeable to the electrolyte ions and a volumetric gating with a volumetric capacitance C^* is observed. This principle is illustrated in Figure 2.8. In these types of devices, applying a gate voltage injects ions from the electolyte into the channel, where the doping state of the active material is changed by reduction or oxidation. However, the underlying device physics of ECTs is theoretically described by the Bernards model, which implies a purely capacitive compensation of opposite electrostatic charges in the semiconductor instead of electrochemical oxidation/reduction.[155,156] Within the Bernads model, ECTs are conceptually split into the ionic circuit and the electronic circuit, describing the ion movement between gate, electrolyte and channel and the current flow between source and drain separately.

In ECTs huge volumetric capacitances instead of areal capacitances are exhibited and since the entire volume of the semiconductor becomes conductive in the *on*-state of the transistor, large drain current modulation is observed already at low gate voltages.[157,158]

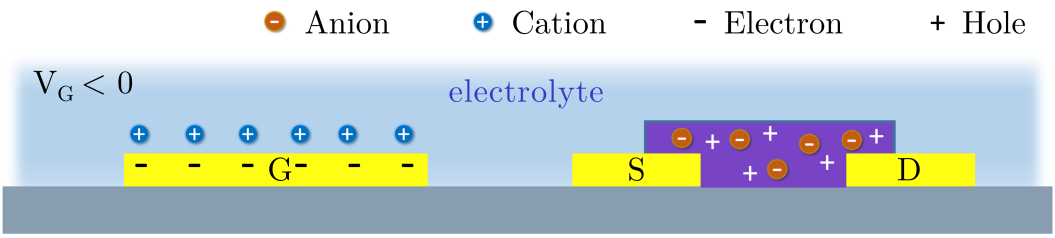

Figure 2.8: Cross section of an ECT with side-gate architecture upon gating with a negative gate voltage. At the gate electrode an electric double-layer is formed and volumetric gating is achieved in the channel.

Typical capacitance values for the different types of devices range from C' values of tens of $\mathrm{nF\,cm^{-2}}$ for a solid SiO_2 dielectric,[159] over C' values around 1–10 $\mathrm{\mu F\,cm^{-2}}$ for an areal electrical double layer[160] to $d \cdot C^*$ values of up to 500 $\mathrm{\mu F\,cm^{-2}}$ for an ECT.[161]

The enormous capacitances give ECTs the ability to transduce small voltages into large drain

currents, which translates into steep transfer curves and ultimately large transconductance values.[157] The equations derived previously for FETs still hold true for ECTs, however the areal capacitance C' is replaced by the volumetric capacitance C^* and the thickness d of the semiconductor is added, leading to the following equation for the transconductance in the saturation regime:

$$g_{\mathrm{m,sat}} = \frac{W}{L} d\mu_{\mathrm{sat}} C^* (V_{\mathrm{G}} - V_{\mathrm{th}}). \tag{2.17}$$

The trade-off to the large transconductance values are the rather slow switching speeds of ECTs, which can be limited by the electronic circuit but in most cases are limited by the response time of the ionic circuit.[155,161] Thus, ECTs are most suitable for (bio)sensing applications[16,162] and as transducers in biological interfacing[161,163] or as neuromorphic devices.[18,164] The latter will be discussed in the next section.

In order to benchmark and compare materials for ECTs the product of charge carrier mobility and volumetric capacitances μC^* has emerged as a figure of merit,[165] as they are the two material dependent parameters that directly determine the transconductance. By plotting the saturation transconductance against all parameters from equation (2.17) that are not material dependent, the material performances can be readily compared from their intersection with the y-axis, as shown in Figure 2.9.[166] The best performing materials can be found in the upper part of this plot.

State-of-the-art materials are found in the field of conducting and semiconducting polymers (see Figure 2.9), with the most prominent representative poly(3,4ethylenedioxythiophene) :poly(styrene sulfonate) (PEDOT:PSS). ECTs with conducting polymers, such as PEDOT:PSS, are in the on-state without a gate voltage and turn off when being gated (depletion mode). The success of PEDOT:PSS as ECT material stems from the high drift velocities of ions injected from an electrolyte, which are comparable to the ones observed in water.[156,168,169] Additionally, PEDOT:PSS exhibits a large hole conductivity of up to $1000\,\mathrm{S\,cm^{-1}}$,[170] is stable in aqueous electrolytes[171] and, since it is commercially available as aqueous dispersions, can be solution processed at low cost. Recent development for new materials has focused on improving the electronic properties with for example fused thiophenes that exhibit higher

a)

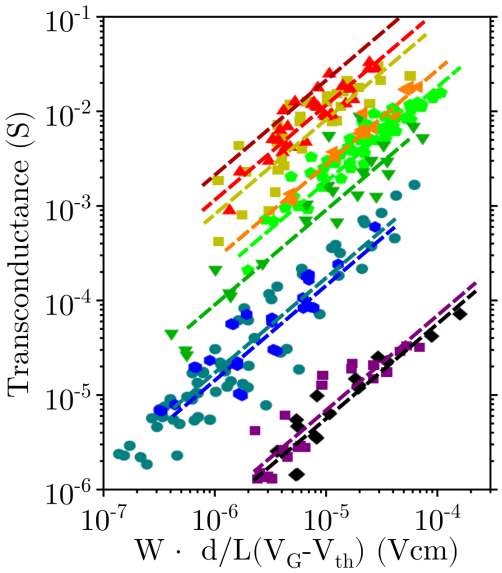

b)

Polymer	μC*(Fcm^{-1}V^{-1}s^{-1})
p(g1T2-g5T2)	496
p(g2T-TT)	261
p(g2T-T)	167
PEDOT:TOS [VPP]	72
PEDOT:PSS + EG	47
PEDOT:PSTFSILi100	20
PTHS + EG	5.5
PEDOT:DS + EG	2.2
p(gNDI-g2T)	0.18
PEDOT:PMATFSILi80	0.15

Figure 2.9: a) Graphical determination of the figure of merit μC^* for state-of-the-art polymers for ECTs and b) reported μC^* values. The colors refer to the same material in a) and b). The dashed lines are guides for the eye and the data was taken from references 165 and 167.

hole mobilities than PEDOT:PSS.[172] A common approach to boost the volumetric capacitances of polymers is to make them more hydrophilic and improve ion-transport with side chain engineering. Usually this is done by replacing hydrophobic alkyl side chains by hydrophilic (oligo)ethylene glycole chains of different lengths.[167,173] However, this approach is limited by the fact that enhanced hydrophilicity leads to increased swelling of the films which is ultimately detrimental to the charge transport.[173–175] Over the last decade, the hunt for new record-breaking materials has created a rapidly changing reasearch field. In 2015 PEDOT:PSS with ethylene glycole reached a μC^* value of 75 F cm^{-1} V^{-1} s^{-1},[161] which was already one year later surpassed by poly(2-(3,3'-bis(2-(2-(2-methoxyethoxy)ethoxy)ethoxy)-[2,2'-bithiophen]-5-yl) thieno[3,2-b] thiophene) (p(g2T-TT)) with the new benchmark value μC^* value of 228 F cm^{-1} V^{-1} s^{-1}.[176] Since then, new derivatives of this polymer have been investigated and values of up to 500 F cm^{-1} V^{-1} s^{-1} were demonstrated.[167] At this point, however, other parameters have been put forward such as long-term and cycle stability, which are crucial aspects for real applications and commercialization. The benchmark polymer p(g2T-TT) for example has been shown to retain only 75 % of its initial on-current after 700 switching cycles within 2 h.[176] In the last years, a lot of progress has been made in this

direction and state-of-the-art materials are able to retain up to 98 % of their current under identical conditions.[167]

SWNTs networks have been investigated as semiconductor for EG-FETs and have been successfully implemented as sensors in aqueous electrolytes.[13,14] Due to the low dimensionality of nanotubes and the formation of porous networks, electrolytes can penetrate SWNT films, similar to the volumetric gating achieved in ECTs. Therefore, EG-FETs with SWNT networks can be readily compared to ECTs and common ECT materials. However, especially polymer-wrapped SWNTs are a very hydrophobic material, which impedes their performance and volumetric capacitances in combination with aqueous electrolytes. The history of well-performing ECT materials clearly shows, that a certain hydrophilicity is a requirement[156] as it is essential for proper ion transport[168,176–179] Another important aspect of SWNTs is their comparably small quantum capacitance C_q as introduced in the beginning of this chapter. Especially in combination with electrolytes this becomes a limiting factor. The small quantum capacitance dominates the overall interfacial capacitance as it is connected in series – if imagined as an electrical circuit – to the huge double layer capacitance C_dl:[55,180]

$$\frac{1}{C_\mathrm{interface}} = \frac{1}{C_\mathrm{dl}} + \frac{1}{C_\mathrm{q}}. \tag{2.18}$$

Although the achievable volumetric capacitances are limited in that regard, SWNT networks outperform most state-of-the-art ECT materials in terms of their charge carrier mobility, which speaks in their favor. Further discussion can be found in chapter 4.

2.3 Brain-Inspired Computing

One of the most heavily researched topics in the last decades is artificial intelligence (AI) with all its promising applications in healthcare,[181] project management,[182] autonomous control of machines or vehicles[183] and for human-machine interfaces such as voice recognition.[184] A large subfield of AI is machine learning, which represents algorithms that are able to produce models for specific training data to correctly map inputs to outputs. These algorithms are implemented on artificial neural networks (ANNs), where artificial neurons are connected to form a deep network[185] to resemble cognitive human functions. That way, the

algorithms feature brain-like learning mechanisms, which are however mostly implemented on the software level on sequential silicon hardware. Consequently, these approaches face the *von Neumann bottleneck*, originating from the limited speed at which data can be transferred between memory and processor.[186] In order to mimic the highly parallel computing power of the human brain, new hardware systems are under development featuring neural and synaptic functions on the device level.[19,187,188] In the following sections, the basic biological principles are briefly explained, followed by a description of artificial synapses and the state-of-the-art of neuromorphic computing.

2.3.1 Biological Principles

The center of the nervous system of most vertebrate and invertebrate animals is called the brain and consists of a highly complex three dimensional network of neurons, whose connections are called synapses. This evolution optimized structure allows for parallel computation at tens of watts per day, while being adaptable to external stimuli by means of plasticity, which describes the strengthening and weakening of synapses. An average male human brain weights around 1.5 kg and contains about 86 billion neurons and almost equally non-neuron cells.[189] The complexity of the brain is hard to imagine, given the fact, that this large number of neurons is connected by up to 0.15 quadrillion synapses and the total distance that was covered if all nerve fibers were aligned is 150 000–180 000 km.[190]

Neurons are made of a cell core, called the *soma* which spreads out into root-like branches called the *dendrites* that narrow down to the *axons* and finally form a connection to the next neuron *via synapses* as illustrated in Figure 2.10. The computation is performed by the neurons, which generate voltage spikes – so called action potentials (APs) – that are forwarded along the axons and synapses to downstream neurons. These outgoing APs are generated when the integration of all incoming APs reaches a certain threshold (integrate-and-fire model).[191] Synapses come as chemical or in rare cases as electrical synapses. Chemical synapses transmit the APs by releasing neurotransmitters into the gap between the presynaptic and the postsynaptic membrane (synaptic cleft), which diffuse to the receiving neuron and trigger an electrical response, the post-synaptic potential (PSP). Electrical synapses are

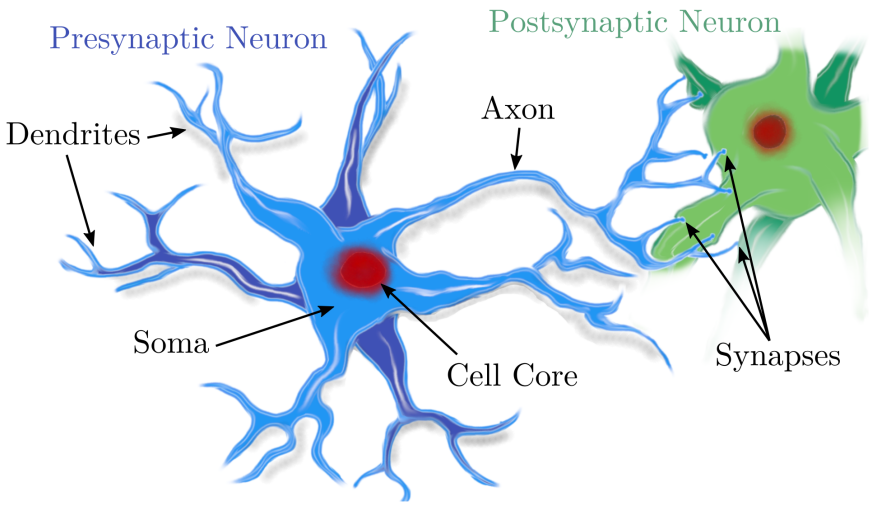

Figure 2.10: Illustration of two connected biological neurons. Information travels as APs across the axion of the presynaptic neuron (blue) and over synapses to the postsynaptic neuron (green).

able to exchange ions directly but are mostly found in the early developing phases of the mammalian brain.[192]

The most complex but also powerful computation mechanism in the brain is plasticity, describing the ability to adapt to the history of previous experiences and learn. This learning and adaptation is mainly controlled by the connection strength of the synapses, called the synaptic weight. The famous postulate from Donal Hebb in 1949 describes this change in synaptic plasticity between a transmitting neuron A and a receiving neuron B in a precise manner:

"When an axon of cell A is near enough to excite cell B and repeatedly or persistently takes part in firing it, some growth process or metabolic change takes place in one or both cells such that A's efficiency, as one of the cells firing B, is increased." (Hebb, 1949)[193]

This statement has been rephrased later into the short mnemonic "what fires together, wires together". However, this simple rule does not cover the full picture and there are many forms of synaptic plasticity, allowing to increase/potentiate the synaptic weight but also to decrease/depress it. The different mechanisms are mainly distinguished by the time scales on which they are relevant, ranging from short-term plasticity (STP) starting at milliseconds

to long-term plasticity (LTP) of up to days and months. Computational brain functions are believed to be based on STP, while learning and memory is attributed to LTP.[194]

The decision whether a synaptic weight should be potentiated or depressed is based on causality. To determine the causality of a signal, the exact timing of the presynaptic AP t_{pre} in relation to the firing of the postsynaptic neuron t_{post} is crucial.

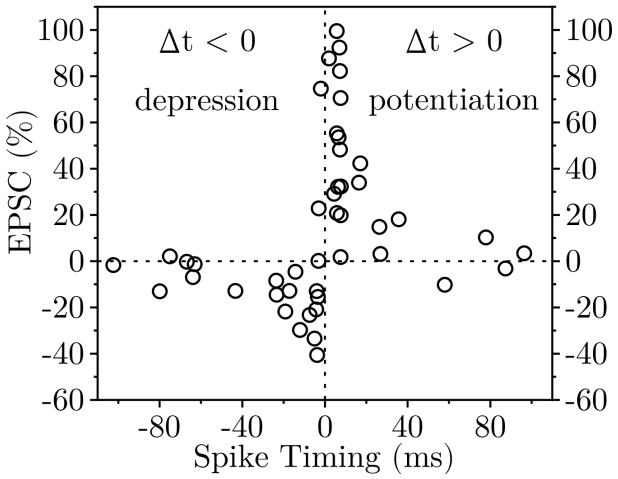

Figure 2.11: Biological STDP response, measured at rat hippocampal neurons, showing depressed and potentiated EPSC branches for negative and positve spike-timings, respectively. The data was taken from reference 195.

All signals with a positive spike timing difference $\Delta t = t_{\mathrm{post}} - t_{\mathrm{pre}}$ are causal, since the presynaptic spike arrived prior to the computation event of the postsynaptic neuron. If $\Delta t < 0$, the signal from the corresponding synapse is anticausal. This mechanism is called spike-timing dependent plasticity (STDP) and the change in excitatory postsynaptic current (EPSC) is depicted for a biological synapse of a rat in Figure 2.11.[195,196] Evidently, the closer the spike-timings are, the stronger the response of the system, leading to changes in the EPSCs of up to $\pm 100\,\%$.

The processes and mechanisms described in a very simple and brief manner in this section are significantly more complex and are subject to ongoing research in neuroscience, which also motivates the development of artificial synapses as a supplement to test and improve existing models of biological systems.

2.3.2 Artificial Synapses

Spiking neural networks and artificial synapses have been implemented as silicon circuits and are investigated for quite some time already.[197] Already in 1971 Leon Chua theoretically described the missing 4^{th} circuit element, the *memristor*, which next to the resistor, the capacitor and the inductor combines memory and transistor aspects.[198] Memristors are nonlinear dynamic devices whose resistance change depending on the history of previous operations and conditions and have been demonstrated in 2008.[199] By definition, artifical synapses belong to the device class of memristive devices and share many similarities with biological synapses, as the variable resistance resembles synaptic strength and the dependence on the history of previous operations emulates the mechanisms of synaptic plasticity. The term artificial synapse is nowadays very ambiguously defined and can describe large circuits of many electronic components or only single devices. Devices that are optimized and developed for the implementation in ANNs to perform vector-matrix multiplication are termed artificial synapses, which is described in this work as neuromorphic computing devices in the next section. However there is also an interest to develop artificial synapses which are single electronic devices that mimic the current understanding of biological synapses as precisely as possible.[19] Chapter 5 reports on the challenging task of developing an artificial synapse that follows the latter definition. In many aspects the properties of an artificial synapse and those of a neuromorphic device are very similar, which leads to the ambiguity. Both types of devices operate at minimum energy consumption and feature a current-voltage characteristic that is based on the history of previous switching events. However, fundamental mechanisms of biological synapses such as STDP and STP are unwanted for efficient neuromorphic computing, where instead other parameters such as state retention and controlled operation are essential as will be explained in the next section.

There are many reports with different approaches to develop low power consuming single devices that feature STP, LTP, and STDP or a related mechanism such as spike-rate-dependent plasticity (SRDP).[200] One way is to use floating-gate transistors, where the history of trapped charges on the floating gate leads to corresponding changes in the channel conductance, which emulates synaptic plasticity.[201] Another approach are ferroelectric-gate synaptic transistors, which make use of multidomain polarization of ferroelectric gates to

enable a gradually tunable channel conductance in order to mimic synaptic learning mechanisms.[202] A rather exotic field of synaptic devices relies on optical stimulation to generate a photocurrent, which is however usually harder to control and synaptic depression is rarely demonstrated.[203] So far, the most reports of artificial synapses have been about electrolyte-gated synaptic transistors,[181,204–206] probably due to the most facile device fabrication and the similarity to the biological counterpart, as the penetration of ions into a semiconductor can be readily compared to neurotransmitters entering the cleft of a chemical synapse. The same approach has been chosen to fabricate artificial synapses with SWNT networks in chapter 5 of this work.

2.3.3 Neuromorphic Computing

The research field around neuromorphic computing follows the aim of developing a new brain-like computation platform for energy efficient parallel computing. Conventional digital computers based on silicon chips were not invented for parallel computing. Supercomputers such as IBM's Blue Gene require power on the order of 10 MW to simulate only a small fraction of brain activity.[200,207] A heavily researched and promising approach are analog circuits, as for example developed within the BrainScaleS project at Heidelberg University.[208] Although analog systems require minimal amounts of power and operate many times faster than the biological counterparts, they are hardwired systems with low flexibility.[209]
The ultimate goal is to develop single neuromorphic devices that require minimal amounts of energy and can be arranged in artificial neural networks to perform vector-matrix multiplication on the hardware level. This vector-matrix multiplication is performed between input layers (for example of pixels of an image or of a list of datapoints) and output layers of an ANN, as depicted in Figure 2.12a.[19,210]
Each input x_i is connected to all outputs y_j of the next layer and the connection between the nodes $w_\mathrm{i,j}$, resembling the synaptic strength, can be modulated by training. While this is usually implemented in software and the output nodes are calculated by $y_\mathrm{j} = \sum_n w_\mathrm{i,j} x_\mathrm{i}$, it is also possible to perform in hardware as depicted in Figure 2.12b.[211] Making use of Ohm's and Kirchhoff's laws, the result of vector-matrix multiplication is directly given by the read-out currents determined by $I_\mathrm{j} = \sum_n G_\mathrm{i,j} V_\mathrm{i}$, where $G_\mathrm{i,j}$ (or $w_\mathrm{i,j}$) is the conductance

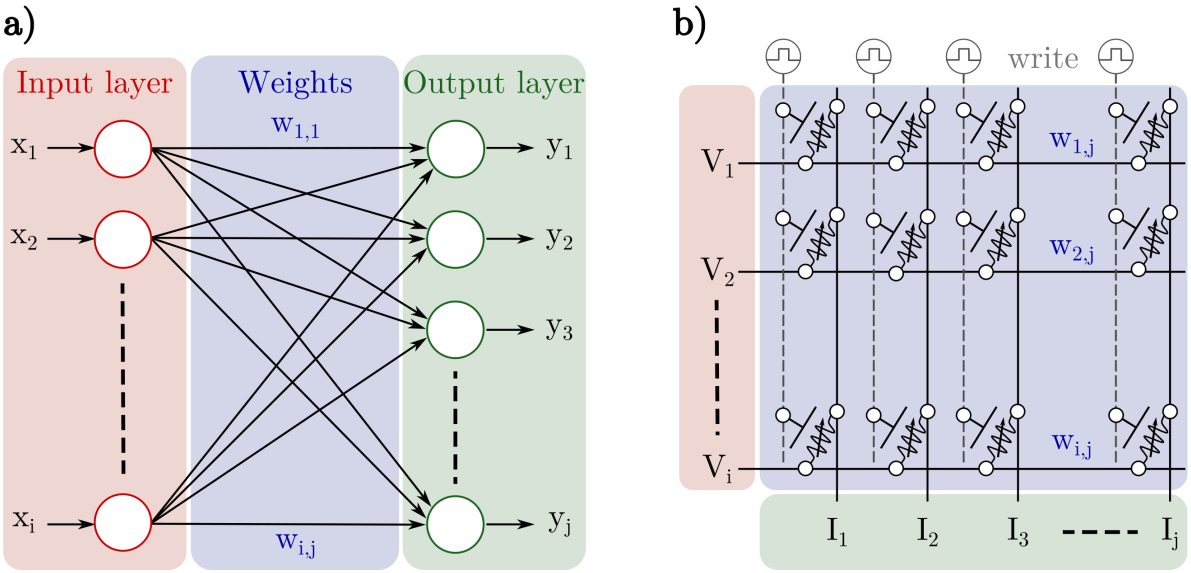

Figure 2.12: Concept of a neural network and how it would be implemented in a) software and b) hardware. Every node from the input layer (red) is connected with a synaptic weight (blue), that is modified by training, to the nodes from the output layer (green). The synaptic weight in b) is represented by the conductance $G_{i,j}$ of the neuromorphic devices, which is tunable by write pulses applied at the gate via an access device.

state of the neuromophic device at a specific node in the lattice and V_i is the applied voltage. To avoid crosstalk in this array, every node is connected to some sort of analog switch, a so called access device, that ensures open-circuit conditions in between weight updates and readouts.[19,212]

Neuromorphic devices have to comply with very strict metrics in order to operate the hardware based neural network efficiently.[19,213] Obviously, the energy consumption per switching event should be as low as possible but at least comparable to the energy efficiency of the brain with roughly 1 pJ per event.[214] The energy consumption depends on the required operation voltage and the conductance range of the devices and can be calculated by integrating the electrical power over the duration t_{spike} of the voltage spikes:

$$E = \int_0^{t_{spike}} I \cdot V dt. \tag{2.19}$$

Further, the physical dimensions should be smaller than 1 µm^2 to be able to fabricate dense and compact arrays. The devices need to exhibit at least 100 well-distinguishable conductance states with low noise of less than 0.5 % of the conductance range. Additionally, these

conductance states should be tunable upwards and downwards in linear and symmetric steps to allow for blind weight updates during training. The read and write speed should be on the order of µs for reasonable learning times and the distinct states should be non-volatile with retention times on the order of 10^3 – 10^8 s, depending on the application. Finally, device stability needs to be high with cycle endurances exceeding ideally 10^9 cycles and a good temperature stability that complies with typical array operating temperatures. However, as can be seen from the large ranges, for instance for the state retention times, the research field is still in a young state and it is not entirely clear how a final application in combination with common sequential systems would operate and which specifications are crucial.

Therefore, in literature many approaches are under investigation all offering strengths and weaknesses in fulfilling the above mentioned criteria. The different types of devices are based on diverse mechanisms, such as localized conductive filament formation,[215,216] ion migration,[210,217,218] charge-trapping-based switching,[219–222] light-assisted reactions or switching[223–225] or electrochemical redox-based switching.[18,164,226] Switching the conductance by the formation of conductive filaments commonly shows non-linear and unsymmetrical behavior, as well as high energy dissipation once the devices are fully trained and fully conductive.[212,216,227,228] Ion migration, for example in perovskite films, shows synaptic mechanisms at very low power consumption ($\mathrm{fJ}/(100\,\mathrm{nm}^2)$),[229] however device stability and state stability are usually lower.[218] Employing charge-trapping as learning mechanism offers promising properties, such as low power consumption and long state retention, yet downscaling of device dimensions, especially of the channel length reduces discharge times drastically, eventually leading to volatile behavior.[220] Optically trained systems are the least investigated types of devices, although they offer the advantage over electrical systems of requiring no access devices to avoid crosstalk. Outstanding device performance has been reported using a photosensitive blend of poly(3-hexylthiophene) (P3HT) and diarylethene,[230] which should be investigated and optimized further.

So far, the most promising approach is the use of electrochemical transistors, with the most prominent polymers PEDOT:PSS,[164,206] P3HT[205] or p(g2T-TT).[231] The slow ion kinetics in these devices has been optimized to a point where conductance levels can be precisely programmed and retained for long times.[18,232] The first proofs-of-principle have been reported such as pattern recognition using crossbar arrays[133,232,233] and even a learning robot.[231]

This shows that real world applications assisted with neuromorphic computing becomes a relevant topic in the near future. A similar approach is discussed in chapter 5, where ion diffusion through dense networks of SWNTs is investigated as mechanism for artificial synapses and for neuromorphic computing.

Chapter 3

Materials and Experimental Methods

This chapter describes the employed materials, device fabrication methods and characterization techniques in detail.

3.1 Materials

Solvents were used as purchased from Sigma-Aldrich. The chemicals used in this thesis are listed in Table 3.1 together with the suppliers.

Table 3.1: List of employed chemicals and suppliers.

Purpose	Chemical	Abbreviation	Supplier
Wrapping-polymer	Poly[(9,9-dioctylfluorenyl-2,7-diyl)-alt-(6,6'-[2,2'-bipyridine])]	PFO-BPy	American Dye Source
Wrapping-polymer	Poly[(9,9-di(2,5,8,11-tetraoxatridecan-13-yl)fluorenyl-2,7-diyl)-alt-(6,6'-[2,2'-bipyridine])]	TEG-PF-BPy	P. Klein and U. Scherf, Bergische Universität Wuppertal
For ion-gel	Poly(vinylidene fluoride-co-hexafluoro-propylene	P(VDF-HFP)	Sigma-Aldrich
Ionic liquid for ion-gel	1-Ethyl-3-methylimidazolium tris(pentafluoro-ethyl)trifluorophosphate	[EMIM][FAP]	Merck
Aqueous buffer solution for water-gating	Phosphate-buffered saline	PBS	Merck
Surfactant	Sodium cholate	NaCh	Sigma-Aldrich

CoMoCAT® SWNT powders, with a diameter range of 0.79–1.0 nm, were purchased from Sigma-Aldrich (lot no. MKCJ7287) and CHASM Advanced Materials Inc. (Batch SG65i-L58). Supplier information states that CoMoCAT® raw material comes with a carbon content of 95 % and an SWNT content of 93 %. The amount of (6,5) SWNTs is specified as roughly 40 %. The raw material was dried overnight at 110 °C before further purification steps. TUBALL™ SWNT raw material was purchased from OCSiAl (lot no. 109-16092015). The

powder contains a broad mixture of semiconducting and metallic SWNT chiralities with a mean diameter of 1.6 ± 0.4 nm and an average length ≥ 5 µm. The SWNT content is specified by the supplier as ≥ 80 % and raman G/D ratios of ≥ 90 are given.

The polymer TEG-PF-BPy ($M_w = 51\,\mathrm{kg\,mol^{-1}}$) was synthesized by *Dr. Patrick Klein* under the supervision of *Prof. Dr. Ullrich Scherf* at the *Bergische Universität Wuppertal*. The synthesis was performed similar to previous examples for polyfluorene copolymer synthesis[234] *via* Suzuki cross-coupling and is described in detail in the literature.[235,236] The wrapping-polymer PFO-BPy (lot no. 18H011A1) was purchased from American Dye Source with $M_w = 40\,\mathrm{kg\,mol^{-1}}$. The molecular structures of these two wrapping-polymers are shown in Figure 3.1.

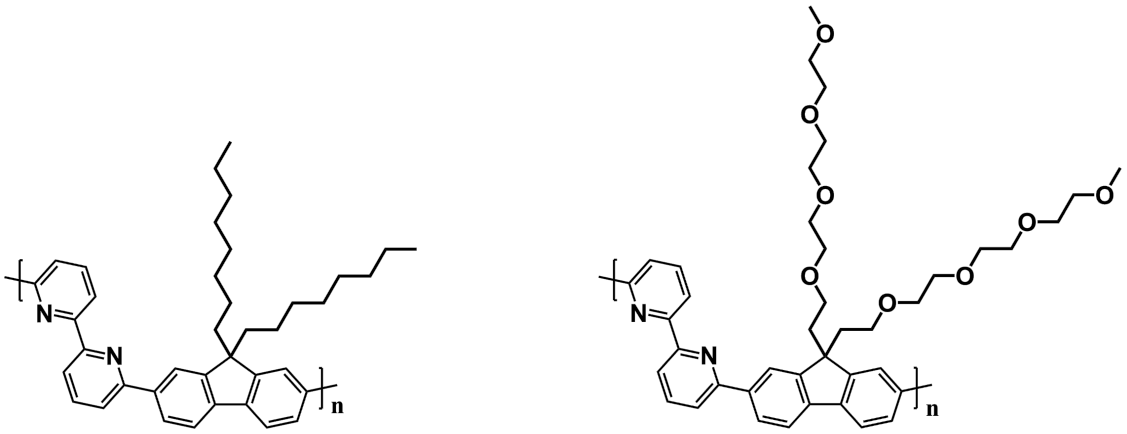

PFO-BPy TEG-PF-BPy

Figure 3.1: Molecular structure of the two wrapping-polymers PFO-BPy and TEG-PF-BPy.

3.2 Dispersions of SWNTs

3.2.1 Monochiral (6,5) SWNT Dispersions

Selective dispersions of (6,5) SWNTs were obtained by polymer-wrapping as described in the literature.[7] CoMoCAT® SWNT powder ($0.4\,\mathrm{g\,L^{-1}}$) was added to a solution of $0.5\,\mathrm{g\,L^{-1}}$ of the wrapping-polymer PFO-BPy in toluene. Exfoliation of the nanotubes was achieved by shear force mixing (Silverson L2/Air) for 3 days at a mixing speed of 10 230 rpm. Bundles and non-exfoliated material were removed by centrifuging two times at 60 000 g for 45 min

(Beckmann Coulter Avanti J26XP) and by filtering through a syringe filter (PTFE, pore size 5 µm). The supernatant was further purified by vacuum filtration through a PTFE membrane (Merck Omnipore, JVWP, pore size 0.1 µm) and rinsing the obtained filter cake with toluene to remove excess and free polymer. These filter cakes with purified (6,5) SWNTs were stored in dry air at room temperature. Directly before usage, they were redispersed *via* bath sonication (Branson 2510) for 30 min in 1 mL of pure toluene. Alternatively, polymer exchange was performed (see below).

3.2.2 Polymer Exchange for Polymer-Wrapped SWNTs

In order to exchange the wrapping-polymer PFO-BPy efficiently with TEG-PF-BPy after purification of the SWNT material, the filter cake with PFO-BPy-wrapped (6,5) SWNTs had to be washed rigorously. Following the published procedure,[113] the filter cakes were soaked seven times for 5 min in hot toluene (80 °C). Thereafter, they were redispersed in 1 mL of a TEG-PF-BPy solution in toluene (1 g L^{-1}) by bath sonication for 30 min. As described above, the free polymer was removed by filtering through a PTFE filter. Before usage, the filter cakes were redispersed by bath sonication for 30 min in fresh toluene, followed by a final centrifugation step at 30 000 g for 30 min.

3.2.3 Mixed Metallic/Semiconducting Dispersions

Mixed dispersions of both metallic and semiconducting SWNTs were produced by adding 2 g L^{-1} of commercial TUBALL™ raw material, with an average SWNT length of 5 µm, to an aqueous sodium cholate solution (6 g L^{-1}). The exfoliation of the material was performed in three consecutive steps, starting with 2 h of bath sonication, followed by 15 min of tip sonication (Weber Ultrasonics, tapered tip, amplitude 20 %, 1 s on/off) and another 2 h of bath sonication. Non-exfoliated fractions were sedimented by centrifugation at 2790 g for 90 min (Andreas Hettich GmBH & Co. KG, Hettich MIKRO 220R centrifuge). The supernatant was diluted in an aqueous solution of sodium cholate (2 g L^{-1}) in a ratio of 1:15 and again centrifuged at 2790 g for 90 min.

3.3 Device Fabrication

All devices in this work were fabricated on AF32eco glass substrates (Schott AG, $25 \times 20 \times 0.3\,\mathrm{mm}^3$). The substrates were cleaned by bath sonication in acetone and isopropanol for 10 min respectively and blow-dried with a nitrogen gun. The chemicals used for photolithography are listed in Table 3.2 together with the suppliers.

Table 3.2: List of employed chemicals for photolithography and suppliers.

Purpose	Chemical	Supplier
Photoresist	LOR5B	MicroChem Corp.
Photoresist	MICROPOSIT S1813	Dow Chemical Co.
Developer	MICROPOSIT MF-319	Dow Chemical Co.
Photoresist	SU-8 2005	microresist technology GmbH
Developer	mr-Dev 600	microresist technology GmbH

3.3.1 Patterned Bottom Electrodes

The electrode patterns used in this work are depicted in Figure 3.2. Corresponding photomasks were designed in Autodesk AutoCAD and produced by Compugraphics Jena GmbH (chrome-on-glass, soda-lime).

For patterning of metal electrodes on the glass sheets, first the lift-off resist LOR5B was spin-coated at 4000 rpm for 30 s and softbaked at 185 °C for 4 min. Next, the positive photoresist MICROPOSIT S1813 was spin-coated on top with identical parameters but softbaked at 115 °C for 1 min. The resist-coated substrates were exposed through the photomasks with UV-light (i-line, $\lambda = 365\,\mathrm{nm}$, $182\,\mathrm{mJ\,cm^{-2}}$) with a mask aligner (SÜSS MicroTec SE, MA6 Gen4, hard contact). After exposure, the samples were developed in MICROPOSIT MF-319 for 25 s, which resulted in an undercut, which is essential for a successful lift-off.

An adhesion layer of 3 nm of chromium and 30 nm of gold was evaporated *via* electron-beam evaporation (Winter Wakuumtechnik GbR, HVB-130) onto the patterned substrates.

Lift-off was performed in *N*-methyl-2-pyrrolidone (NMP) at 60 °C for 1 h, after which the substrates were thoroughly rinsed with ultrapure water and blow-dried with nitrogen.

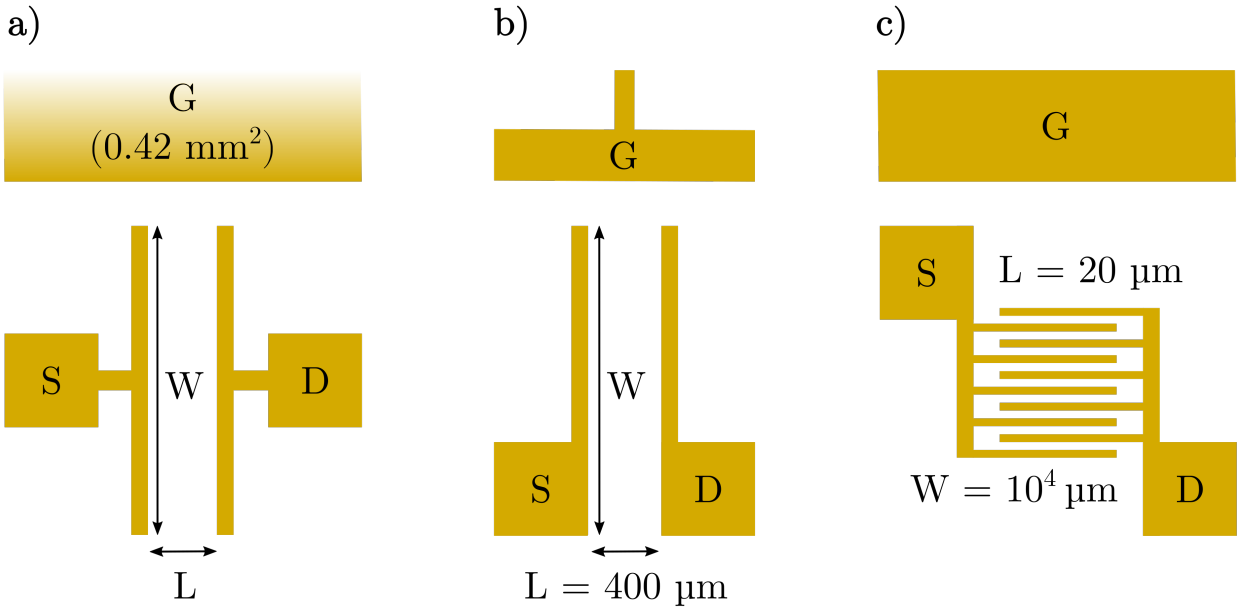

Figure 3.2: Bottom electrode patterns with side gate configuration. a) Large gold side gate with standard T-shaped source drain electrodes of varying W/L ratios (lengths in µm, $\frac{1000}{600} = 1.7$, $\frac{1000}{500} = 2.0$, $\frac{1000}{400} = 2.5$, $\frac{1000}{300} = 3.3$, $\frac{3000}{600} = 5.0$, $\frac{3000}{500} = 6.0$, $\frac{3000}{400} = 7.5$, $\frac{3000}{300} = 10$). b) Small gold side gate for the deposition of gate material with L-shaped source drain electrodes of fixed W/L (W depends on the printed area, L = 400 µm). c) Large gold side gate with interdigitated source drain electrodes with large W/L ratio of $\frac{10\,000}{20} = 500$.

3.3.2 Electrode Passivation

After patterning of the electrodes, a second photolithographic step was performed to passivate them for most of the devices in this work (as stated in the following chapters). For this purpose, the epoxy-based negative photoresist SU-8 2005 was used, which forms a very thick and durable insulating layer after hardbaking.

A diluted solution of the commercial photoresist with cyclopentanone was prepared in a 1:1 ratio and spin-coated in a two-step process (step 1: 10 s at 500 rpm with acceleration 500 rpm s^{-1}, step 2: 30 s at 3000 rpm with acceleration 500 rpm s^{-1}), resulting in a film thickness of around 1.5 µm after a softbake at 95 °C for 2 min.

Next, the samples were exposed to UV-light (i-line, λ = 365 nm, 384 mJ cm^{-2}) with the MA6 Gen4 mask aligner. After that, a post-exposure bake at 95 °C for 90 s was performed

prior to development in MR DEV-600 for 60 s and rinsing with ultrapure water. Finally, the substrates were blow-dried and hardbaked at 150 °C for 5 min. Patterns for passivation were designed to match the structure of the bottom electrodes in a way that only small edges (4–15 µm) were left uncovered by photoresist, to ensure good contact and charge injection into the later deposited SWNT layers but to passivate as much of the electrode area as possible (see Figure 5.6b and c).

3.3.3 Spray-Coating of Mixed SWNTs

A custom-made spraying setup was used to deposit thick films of mixed TUBALL™ dispersions through a shadow mask (see Figure 3.3). The shadow mask was designed in Autodesk AutoCAD and produced by Becktronic GmbH (lasercut, 0.2 mm stainless steel). The sample and the shadow mask were mounted onto an aluminium holder and placed on a uniaxially movable and heatable stage.

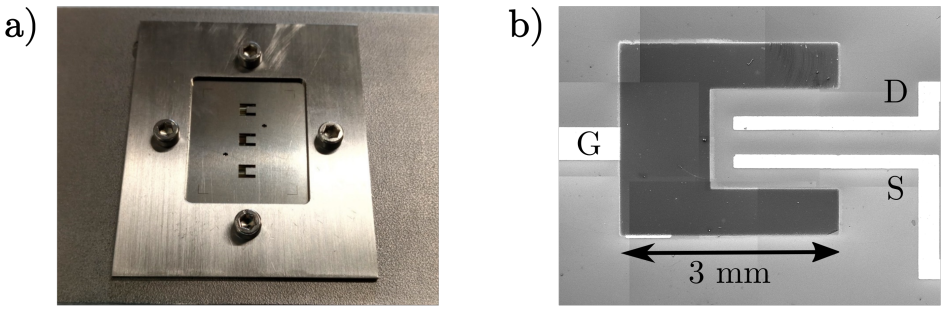

Figure 3.3: a) Photograph of the spray-coating sample holder with a mounted shadow mask. b) Low magnification SEM images stitched together, showing the electrode pattern from Figure 3.2b with a U-shaped spray-coated TUBALL™ SWNT film.

For a fast evaporation of water from the aqueous dispersions, the stage temperature was set to 185 °C and the stage was programmed to continuously swivel back and forth 7 cm below the nozzle of a commercially available airbrush gun (Harder and Steenbeck, Infinity airbrush, 0.15 mm nozzle). Aqueous TUBALL™ dispersions with sodium cholate were diluted with ultrapure water to an optical density of 0.5 cm^{-1} at 660 nm and filtered through a PTFE filter (25 µm pore size) directly before usage. Nitrogen was used as the carrier gas at a pressure of 2 bar and 15 mL of ink were continuously sprayed onto one sample. The needle displacement was optimized with deionized water before every spraying attempt by slowly increasing the

spraying rate to the point, where small droplets became visible on the aluminum-covered heated stage. For spraying, the displacement was then adjusted so that the amount of deposited ink and the evaporation rate of the solvent matched.
Finally, the samples were soaked in deionized water overnight to remove as much sodium cholate from the films as possible.

3.3.4 Aerosol-Jet Printing of (6,5) SWNTs

Networks of (6,5) SWNTs were printed with a commercial Aersol Jet 200 system from Optomec Inc. using a 200 µm nozzle. As described in detail before,[237] custom-made ink vials were used with disposable parts to be able to use the system for a variety of materials. The stage temperature was set to 100 °C and the stage speed to 0.5 mm s^{-1}. Inks were kept at constant temperatures between 8 and 20 °C and were atomized *via* ultrasonication to form a dense aerosol at a transducer current of roughly 460 mA, which was the system's maximum power. The nitrogen flow rates of the collimating sheath gas and the carrier gas were fixed to 30 sccm and 20–26 sccm, respectively.
Purified, monochiral (6,5) SWNT dispersions were formulated into printable inks by adding 2% v/v terpineol. The small fraction of terpineol not only increases the density of the formed aerosol due to an increased ink viscosity, but also guarantees an efficient material transport from the ink vial to the substrate by forming droplets with a high boiling point that reach their destination before drying out.[238] The film thickness is controlled by adjusting the ink concentration, the carrier gas flow rate and the number of printing loops on the same spot. Ink concentrations were determined by diluting the dispersions to the desired optical density at the E_{11} transition (*i.e.* 1–6 cm^{-1} at 996 nm). The print paths were designed in AutoCAD and exported using the plugin VMTOOLS (Optomec Inc.). A grid pattern of horizontal and vertical lines with a pitch of 25 µm resulted in homogeneous films. Finally, the samples were rinsed with tetrahydrofuran (THF) and isopropanol and blow-dried with nitrogen.

3.3.5 Applying Electrolytes and Ion-Gel

The devices were completed by forming a dielectric connection between the side gates and the channel areas through an electrolyte. For devices in capter 4, which were measured

with ultrapure water or PBS-buffer, the electrolytes were contained by a custom-built PTFE sample holder (made by the fine mechanics workshop of the Institute for Physical Chemistry, where an O-ring sealed electrolyte reservoir could be pressed onto the samples (see Figure 3.4). The large volume of the reservoir (several mL) enabled measuring samples over long periods of time without noticeable changes due to evaporating water.

For measurements with PBS, pellets were diluted in 200 mL of ultrapure water to obtain a PBS stock solution with a concentration of 0.01 M phosphate buffer, 0.0027 M potassium chloride and 0.137 M sodium chloride and a pH of 7.4 that could be further diluted.

The samples in chapter 5 were finalized with a spin-coated layer of ion-gel. For that, a solution of the polymer P(VDF-HFP) and the ionic liquid [EMIM][FAP] in acetone was prepared in a mass ratio of P(VDF-HFP):[EMIM][FAP]:acetone = 1:4:14. All steps were performed in a dry-nitrogen glovebox (M.Braun Inertgas-Systeme GmbH, MB200-G), due to the hygroscopic nature of the ionic liquid. Prior to spin-coating, the samples were annealed at 300 °C for 60 min to remove trapped water and oxygen inside the SWNT networks. After spin-coating at 2000 rpm for 30 s, the ion-gel deposited in areas between multiple devices on one substrate was removed with an acetone-soaked wipe to prevent crosstalk. In a final step, the samples were annealed at 80 °C overnight.

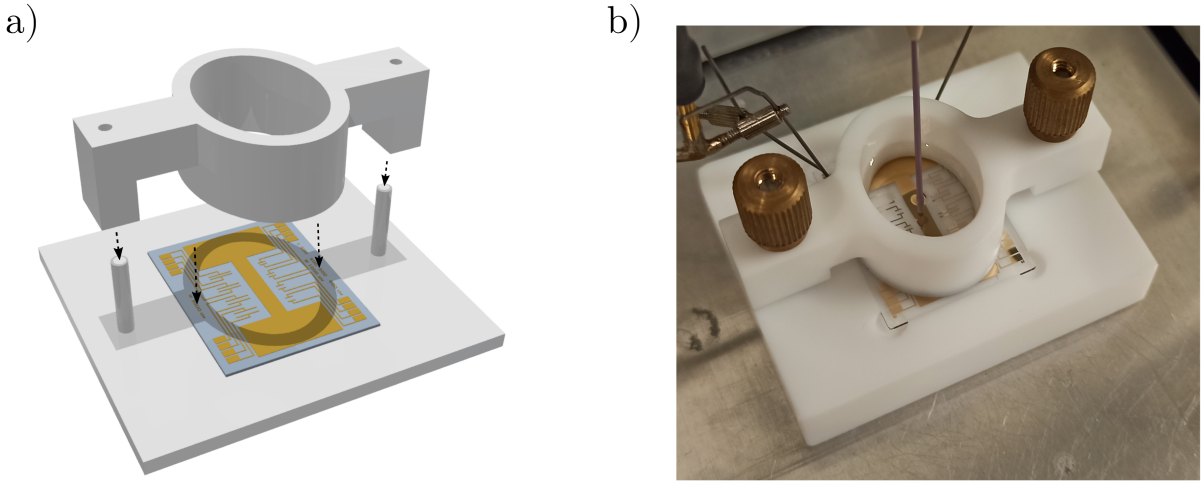

Figure 3.4: Illustration of the custom-made sample holder with electrolyte reservoir. (a) 3D model designed in Autodesk Inventor as construction plan for the fine mechanics workshop of the APC in Heidelberg. (b) Photograph of the setup during a measurement.

3.4 Characterization

3.4.1 Electrical Characterization

A 4155C semiconductor parameter analyzer (SPA) from Agilent Technologies Inc. served for standard transfer and output characteristics. Measurements were performed in ambient air for devices with aqueous electrolytes (chapter 4) and in a nitrogen-filled glovebox (Inert Corp., I-Lab 3GB) for all ion-gel devices (chapter 5). Experiments in aqueous electrolytes were carried out with a Ag/AgCl micro-reference electrode (rhd instruments, 0.1 mol L^{-1} KCL) submerged into the electrolyte close to the gate pad. This electrode was connected to a voltage monitor unit (VMU) of the SPA to determine the applied potential.

a) b)

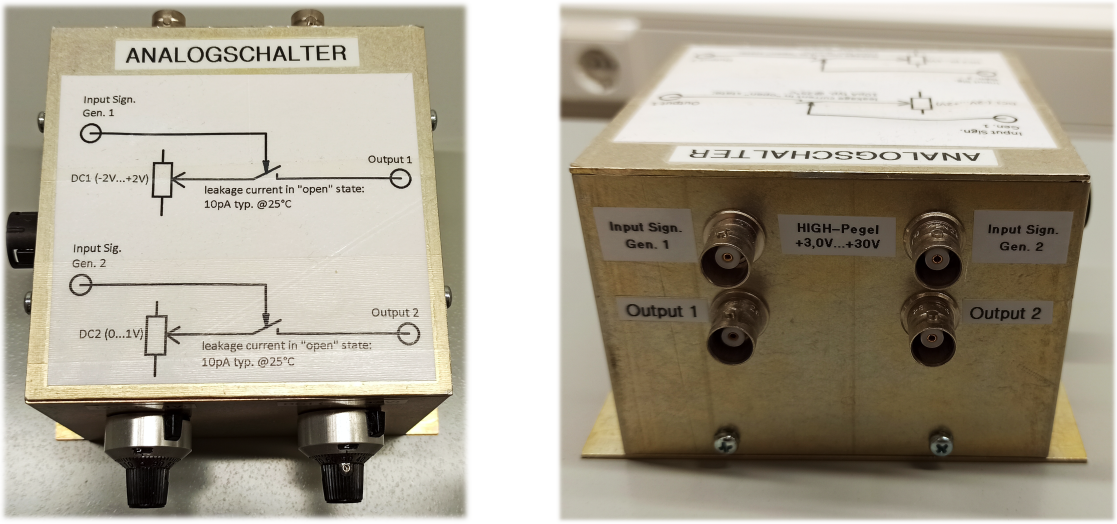

Figure 3.5: Photographs of the custom-built analog switch for pulsed measurements with open-circuit conditions. a) Top view with a schematic of the circuits for the two channels and b) side view with BNC connections for the inputs and outputs.

Capacitances were quantified with a Modulab XM MTS impedance analyser from Solarton Analytical in a two-electrode setup, where the shorted source and drain electrodes acted as the working electrode and the gold side gate as the counter electrode. A 1 Hz modulation of 10 mV rms was applied to the gate for the off- and on-state of the devices respectively.
To perform pulsed measurements with open circuit conditions inbetween the voltage pulses in chapter 5, a custom-built analog switch (see Figure 3.5) was constructed in collaboration with the electronics workshop. The two BNC outputs of this circuit were controlled with two

potentiometers and a waveform generator (Keysight Trueform 33600 A Series) connected to the inputs. The outputs change from open circuit to a DC voltage when 5 V are applied to the input. The two potentiometers define the output voltage range, which is 0–2 V at output 1 and up to 1 V for output 2.
Voltages and currents were recorded with a B1500A SPA from Keysight Technologies Inc. during these measurements.

3.4.2 Photoluminescence Spectroscopy

Dispersion stability was investigated by continuous photoluminescence (PL) sampling with a Horiba Jobin-Yvon Fluorolog®-3 spectrometer. SWNT dispersions were diluted to an absorbance of 0.4 cm^{-1} at the E_{11} transition (996 nm for (6,5) SWNTs) and placed in a 4 × 10 mm^2 quartz cuvette. The samples were excited along the 10 mm cuvette axis at the E_{22} transition (575 nm for (6,5) SWNTs) using a 450 W xenon lamp and a double monochromator. The emission was detected perpendicular to the excitation, along the 4 mm axis, by a liquid nitrogen-cooled InGaAs diode array, covering a range of 800–1600 nm. The aggregation was monitored over several hours with an integration time and a delay between measurements of both 30 s.
In situ PL analysis of transistors in operation was performed with a supercontinuum laser (Fianium Ltd., WhiteLase SC400) that was pulsed at a filtered wavelength of 575 nm with a 20 MHz repetition rate and a picosecond pulse width. An Acton SpectraPro SP2358 spectrometer and a liquid nitrogen-cooled InGaAs line camera (Princeton Instruments, OMA V:1024-1.7 LN) were employed for recording PL spectra. The same 50× objective (Olympus, NA = 0.65) was used to both focus the excitation laser through the glass substrate onto the device and to collect the emitted PL. Scattered excitation light was blocked with a dichroic long-pass filter, cutting off at 875 nm. The transistors were operated by applying a small source-drain voltage of −0.1 V and a gate voltage sweep from +0.5 to −1.0 V with a Keithley 2612A source meter. PL spectra and currents were measured after an equilibration time of 5 min for every gate voltage step.

3.4.3 Raman and UV-Vis-NIR Absorption Spectroscopy

The quality of the SWNT dispersions was characterized by Raman spectroscopy and absorption spectroscopy to determine the purity and concentration.

A confocal Raman microscope (Renishaw, InVia Reflex) with a 50× (Leica Microsystems GmbH, NA = 0.75) objective and three different lasers (532 nm, 633 nm and 785 nm) was utilized. The system was operated in StreamLine™ mode to collect maps over $100 \times 100\,\mu m^2$ of dropcast SWNT films on aluminium foil (see Figure 2.4). Only dispersions without detectable metallic nanotube species were taken for further experiments.

UV-Vis-NIR absorption spectra were measured with a Cary 6000i from Varian Inc. featuring a silicon detector for short wavelengths (175–800 nm) and an InGaAs detector for the NIR range (800–1800 nm). A cuvette with 1 cm path length, filled with a diluted dispersion, was inserted into the dual-beam setup. A baseline with the respective pure solvent was acquired before the actual measurement (see Figure 2.3).

3.4.4 Atomic Force Microscopy and Profilometry

The SWNT network morphology was investigated with an atomic force microscope (AFM). A Dimension Icon was used in ScanAsyst® mode with SCANASYST-AIR tips and a DAFMCH cantilever holder (all Bruker Corp.). Representative areas of $5 \times 5\,\mu m^2$ were scanned with 1024 samples per line and a scanning frequency of 1 Hz. The open-source program Gwyddion was used to process the data and generate images.

For the determination of film thicknesses, both the AFM and a profilometer (Bruker Corp., DektakXT Stylus Profiler) were employed. The films were scratched with a cannula and scanned perpendicular to that scratch. Averaging along the profile yielded the final average film thickness. Depending on the expected film thicknesses, the AFM (below ≈ 10 nm) or the DektakXT (above 10 nm) was utilized for the scan.

3.4.5 Optical and Scanning Electron Microscopy

Topological investigations of the fabricated samples were carried out with an Olympus BX51 optical microscope equipped with Olympus objectives for 5×, 10×, 20× and 100× magnification. Bright-field and dark-field images were taken and processed using the Stream Essentials

software.

A more detailed view regarding topology but also morphology was gained with scanning electron microscopy (SEM) using a JEOL JSM-7610F field emission system. Both backscattered and secondary electrons were detected with an in-lens detector (SEI) for high resolution imaging and an in-the-chamber detector (LEI) for topological views. Acceleration voltages up to 15 kV and a working distance around 8 mm were used. A conductive connection between the regions of interest on the sample and the sample holder was established by contacting the electrodes of devices with copper tape and conductive silver paste. This grounding significantly reduced distortions in the images by charging of the samples. Samples in which the electrodes were passivated with SU-8 photoresist were mostly analysed using the gentle beam mode, in which a decelerating voltage is applied to the sample holder to prevent damaging and charging of the samples.

Chapter 4

Functionalization of Polymer-Wrapped (6,5) SWNTs with Ethylene Glycol Side Chains for Improved Electrochemical Transistors

This chapter demonstrates highly efficient water-gated electrochemical transistors by introducing oligoethylene glycole side chains to polymer-wrapped (6,5) SWNTs.

Most of the data and results in this chapter were published in the journal article Heimfarth *et al. ACS Appl. Mater. Interfaces* **2022**, 14 (6), 8209-8217.[235] Figures and tables were adapted with permission from the American Chemical Society. The polymer TEG-PF-BPy was synthesized by *Dr. Patrick Klein* at the Wuppertal Center for Smart Materials and Systems at the Bergische Universität Wuppertal under the supervision of *Prof. Dr. Ullrich Scherf*. All photoluminescence measurements were carried out by *Merve Balcı Leinen*.

4.1 Introduction

A lot of research in the field of organic electrochemical transistors is dedicated towards the optimization and discovery of new active materials. Especially biocompatible materials that can operate in aqueous media are in great demand for a variety of bioelectronic applications. Films of conducting and semiconducting conjugated polymers,[156,164,165,239–241] currently dominate the field owing to their permeability for electrolyte ions, which enables high charge accumulations and thus high currents in the transistor channel. To benchmark the performance of active materials in ECTs, the ability to transduce ionic signals into electronic currents is directly determined and expressed by the peak transconductance. As derived in equation (2.17), of all the parameters that determine the transconductance, the two material specific quantities are the charge carrier mobility μ and the volumetric capacitance C^*. The suitability of a material for ECTs is therefore expressed as the product μC^*, which has become a figure of merit in literature.[156,165]

For this metric, conjugated polymers usually offer low carrier mobilities but compensate this deficiency with their immense volumetric capacitances which have been pushed to outstanding values recently ($187\,\mathrm{F\,cm^{-3}}$).[167] A boost in capacitance and ultimately transistor performance is achieved by further improving the ion mobility and thus diffusion into the polymer films.[242] A very effective way to do that is to increase the hydrophilicity of the films by replacing alkyl side chains with oligo(ethylene glycol) chains. The limiting factor of this approach is the swelling of the films when operated in aqueous electrolytes, which can lead to detrimental effects on the charge transport.[173–175] Many studies of both p-type and n-type glycolated polymer transistors have been reported,[176–178,243,244] where the length and distribution of side chains was optimized. The best performances in terms of μC^* are on the

order of 200 to 500 $\mathrm{F\,cm^{-1}\,V^{-1}\,s^{-1}}$.[165,167]

Adapting the successful ethylene glycol side chain engineering approach to a hydrophobic but high mobility semiconductor like polymer-wrapped SWNTs[132] is a promising way to create a highly suitable ECT material. This adaptation was realized in this work by functionalizing the SWNTs through a polymer exchange[113,114,245] to replace the hydrophobic alkyl side chains of PFO-BPy with hydrophilic ethylene glycol moieties. In the past, this idea has been used to create stable dispersion in benign polar solvents instead of harmful organic ones[108,109] but was not investigated for ECTs. In this chapter, the influence of the wrapping-polymer of aerosol-jet printed (6,5) SWNTs on the device performance of ECTs with aqueous electrolytes is investigated. For that, a version of PFO-BPy with tetraethylene glycol side chains was synthesized (TEG-PF-BPy, see Figure 3.1) by collaborators from the University of Wuppertal and used for polymer exchange. Electrical measurements on reference samples with PFO-BPy/(6,5) SWNTs and functionalized samples with TEG-PF-BPy/(6,5) SWNTs corroborate a significant increase in transconductance of the more hydrophilic nanotube/polymer network, which originates from higher volumetric capacitances. Further insight is gained by *in situ* photoluminescence spectroscopy on biased samples and a more efficient charging due to the ethylene glycol side chains is confirmed. Extracted values for the figure of merit μC^* of the newly developed polymer/SWNT hybrid are comparable to those of state-of-the-art polymers. However, given the chemical and mechanical robustness of carbon nanotubes[154,246,247] an unexpectedly short operational stability in purified water and in a blood serum-imitating electrolyte like phosphate-buffered saline (PBS) is observed.

4.2 Functionalization by Polymer Exchange

As reference and stock material, purified dispersions of monochiral (6,5) SWNTs were prepared by shear force mixing of CoMoCAT nanotube powder in a solution of PFO-BPy in toluene, as described in chapter 3.2. The synthesis of the wrapping-polymer TEG-PF-BPy with hydrophilic tetraethylene glycol side chains is described in detail in the Supporting Information of the article Heimfarth *et al. ACS Appl. Mater. Interfaces* **2022**, 14 (6), 8209-8217.[235] Following the polymer exchange protocol described in chapter 3.2.2 the filter cake of the stock dispersion is partly transformed into the more hydrophilic polymer/SWNT

hybrid (illustrated in Figure 4.2a). The remaining part of the filter cake served as the reference material throughout the study. When dispersing CoMoCAT raw material directly with TEG-PF-BPy, in contrast to PFO-BPy, a broad mix of chiralities is obtained, which becomes apparent in the optical absorption spectra and the photoluminescence excitation-emission (PLE) maps in Figure 4.1. Clearly, the much longer and very flexible TEG chains reduce the otherwise excellent selectivity of PFO-BPy towards (6,5) SWNTs. This issue makes the extra step of the polymer exchange after purification necessary.

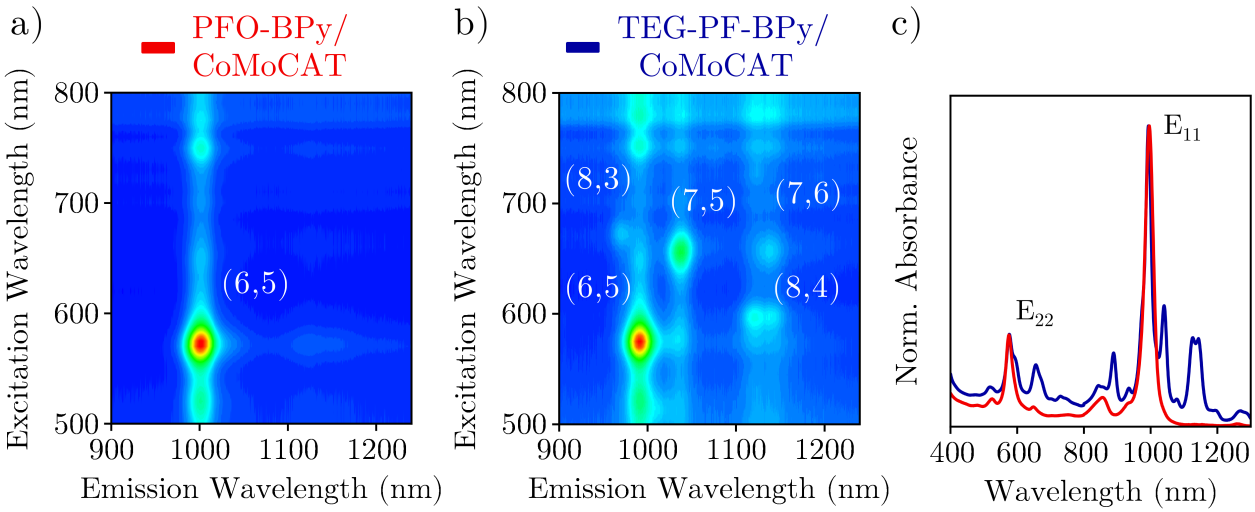

Figure 4.1: Photoluminescence excitation-emission maps of dispersed CoMoCAT raw material using a) PFO-BPy and b) TEG-PF-BPy in toluene. c) Normalized absorption spectra of both dispersions with respect to the E_{11} peak.

To confirm that the quality of the nanotube dispersion during the washing and exchange steps is preserved, the electronic properties and dispersion stability were probed by PL measurements and compared to the stock dispersion. Figure 4.2b shows no shifts or broadening of the characteristic E_{11} transition, corroborating the integrity of the SWNTs. While being detrimental for the selectivity, the long and flexible TEG chains contribute positively to the colloidal stability and prevent aggregation of the dispersion in Figure 4.2c, which is sometimes a problem for the device fabrication.[248,249]

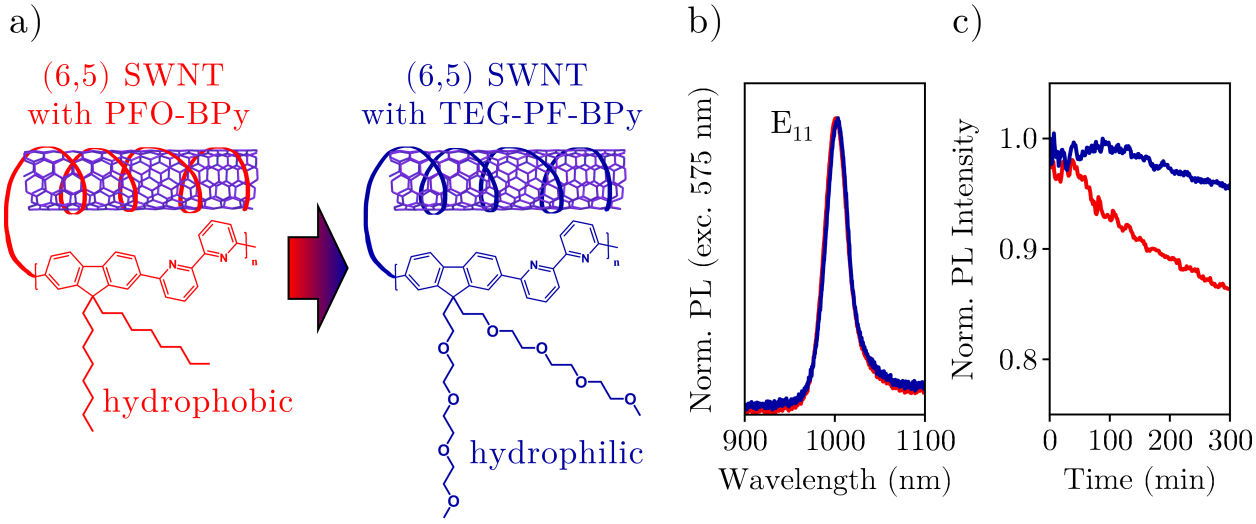

Figure 4.2: (a) Functionalization of (6,5) SWNTs by exchanging the purifying wrapping-polymer PFO-BPy with hydrophobic alkyl side chains by TEG-PF-BPy with hydrophilic ethylene glycol side chains. (b) PL spectra of monochiral (6,5) SWNT dispersions normalized to the E_{11} transition before (red) and after (blue) polymer exchange. (c) Time evolution of the normalized E_{11} PL intensity for dispersions of PFO-BPy/(6,5) SWNTs and TEG-PF-BPy/(6,5) SWNTs in toluene as a measure for dispersion stability.

4.3 Device Layout and Characterization

Although electric double-layers instead of electrochemical redox-based doping occurs in electrolyte-gated SWNT films, the network porosity enables volumetric gating, which is comparable to ECTs. For this reason and to simplify matters, the SWNT EG-FETs in the following chapter will be called ECTs.

Networks of both PFO-BPy/(6,5) SWNTs and TEG-PF-BPy/(6,5) SWNTs were implemented as active layers of ECTs. Electrodes (3 nm Cr + 30 nm Au) were patterned by standard photolithography, featuring a common large side gate centered on the glass substrate and eight sets of T-shaped source and drain electrodes (see Figure 3.2a for the schematic of a single device).

The electrode configuration was chosen to be as simple as possible with long channel lengths and thus relatively large channel areas (see Figure 3.2) to reduce influences of stray currents, contact resistance and parasitic capacitances. Additionally, the electrodes were passivated with a layer of SU-8 photoresist to minimize their contribution to the parasitic capacitance and to suppress leakage currents.

The two polymer/SWNT dispersions were aerosol-jet printed as thin (5–10 nm) and thick

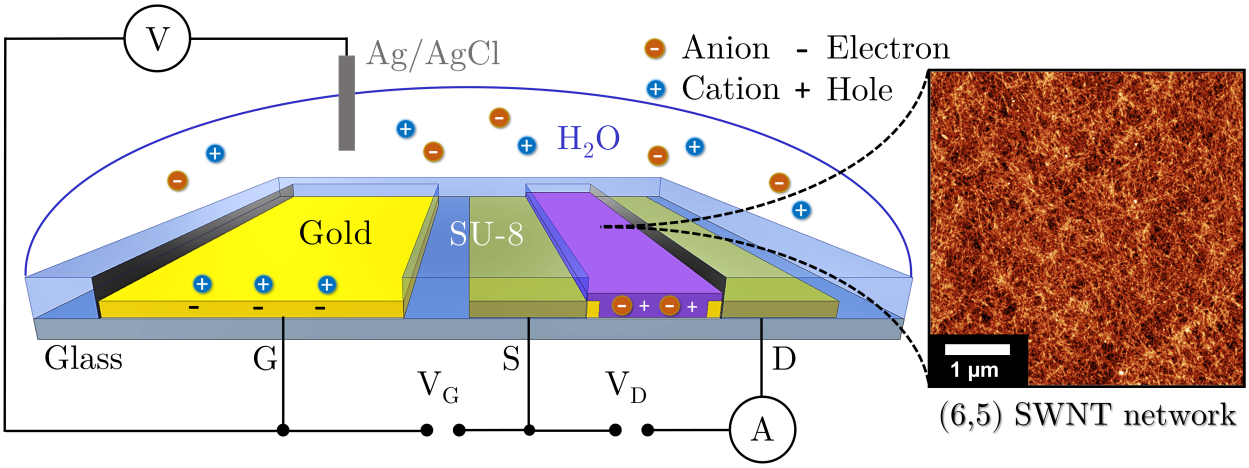

Figure 4.3: (a) Schematic of the ECT design and measurement setup. Water exposure is limited to the channel region and the gate electrode by a passivation layer of SU-8 photoresist. Networks of aerosol-jet-printed (6,5) SWNTs (AFM image) are gated via the large gold side gate and a Ag/AgCl reference electrode is immersed closely to the gate electrode into the electrolyte to monitor the applied voltages.

(up to ≈ 70 nm) layers onto the channel areas. An illustration of the finished device is shown in Figure 4.3.

The morphology of the dense PFO-BPy- and TEG-PF-BPy-wrapped SWNT networks after printing and after rinsing with THF and isopropanol can be compared from the AFM images in Figure 4.4. The fact that the micrographs for the TEG-PF-BPy/(6,5) SWNTs appear more blurry is a first indication for the enhanced hydrophilicity of the film, which promotes the adsorption of water from the air and reduces the resolution. Although all dispersions were printed shortly after redispersion to avoid aggregation, minor differences in the network formation may be present due to the increased dispersion stability of TEG-PF-BPy/(6,5) SWNTs in toluene.

Electrical characterization with ultrapure water and a Ag/AgCl microreference electrode were performed as described in section 3.4.1 and as schematically shown in Figure 4.3. Prior to any other measurements, 10 consecutive linear transfer sweeps at a drain voltage of −0.1 V and a medium integration time of 20 ms were completed on each device to reach a steady state, as shown in Figure 4.5. With every sweep the on-currents increase, indicating that the films became more and more hydrated and the electrolyte ions infiltrate the network more thoroughly. Especially for the hydrophilic TEG-PF-BPy/(6,5) SWNTs this effect is very pronounced and may even produce a slight swelling of the films, which on this level might

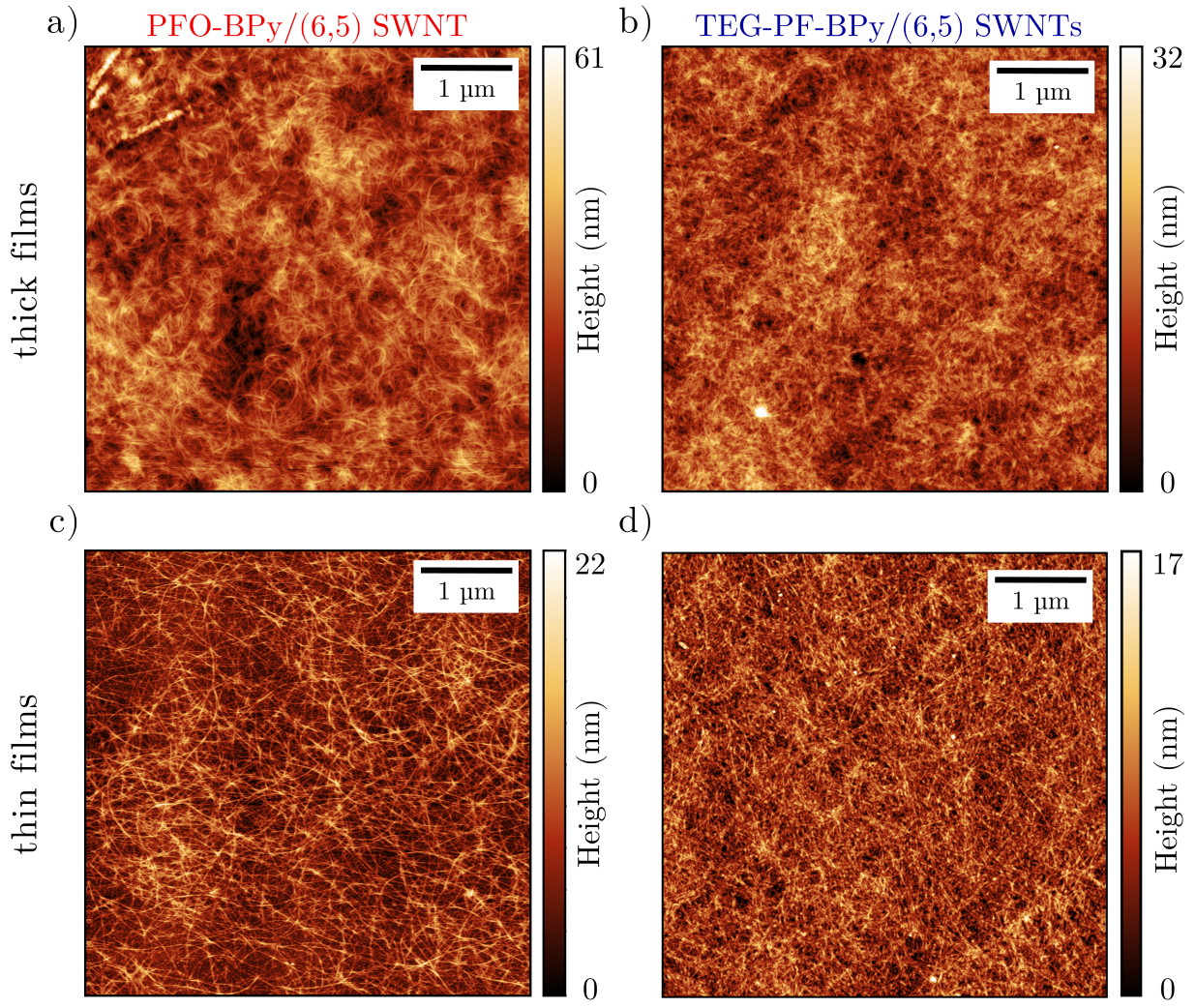

Figure 4.4: AFM images of aerosol-jet printed (6,5) SWNT networks (5 × 5 µm^2). a) Thick and c) thin films of PFO-BPy/(6,5) SWNTs. b) Thick and d) thin films of TEG-PF-BPy/(6,5) SWNTs.

be beneficial for the device performance.

After conditioning, output characteristics were measured in a gate and drain voltage range of 0 to −0.8 V (see Figure 4.6) with a long integration time of 150 ms. For small drain voltages, the devices show well-defined linear behavior, which indicates an Ohmic contact between the nanotube networks and the gold electrodes. At high drain voltages around −0.6 V a distinct saturation regime is reached and only minor current hysteresis is observed for the ECT with TEG-PF-BPy/(6,5) SWNTs. Direct comparison of identical device dimensions and similar film thicknesses show that the maximum drain currents are significantly higher for the SWNT networks with hydrophilic wrapping-polymer.

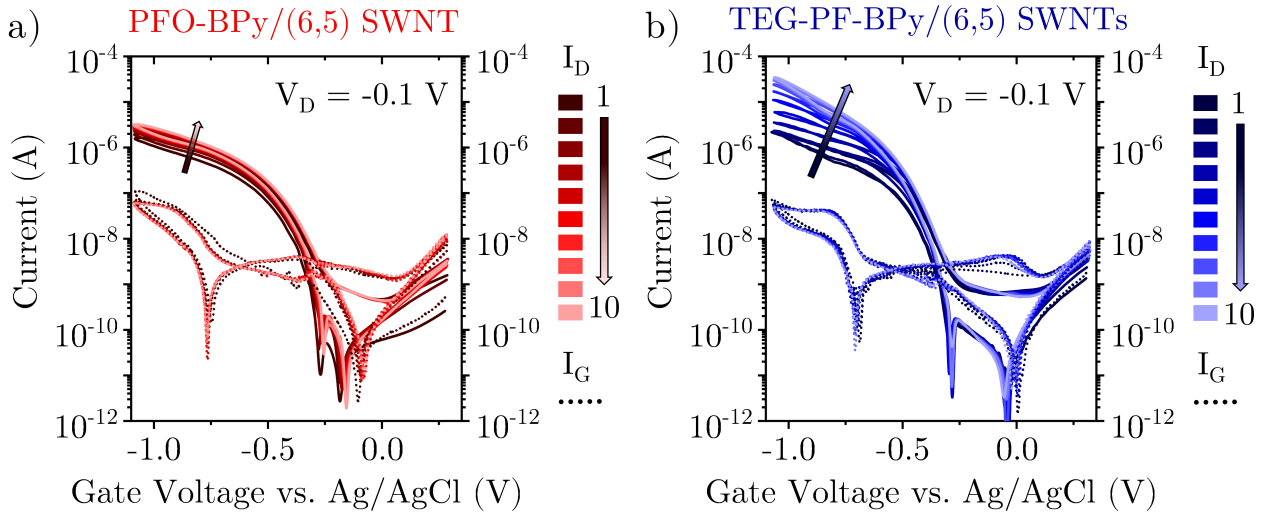

Figure 4.5: Conditioning of ECTs in ultrapure water with a) PFO-BPy/(6,5) SWNT and b) TEG-PF-BPy/(6,5) SWNT thin films by performing ten consecutive linear transfer sweeps.

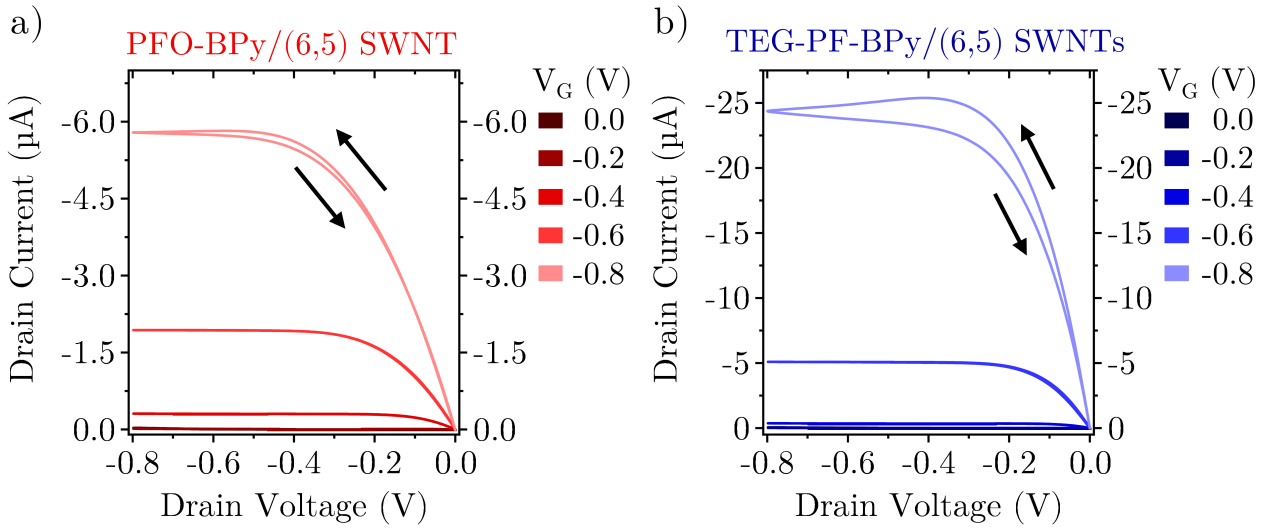

Figure 4.6: Representative output characteristics of water-gated transistors with thin films of a) PFO-BPy/(6,5) SWNTs and b) TEG-PF-BPy/(6,5) SWNTs.

Next, the saturation transfer characteristics were recorded at $V_D = -0.6\,V$, again by scanning slowly with an integration time of 150 ms. Representative transfer curves and the calculated transconductances of devices with equal geometries and thin and thick films are depicted in Figure 4.7. Note that the data was normalized to the L/W ratio for better comparison. In general, the hydrophilic TEG-PF-BPy/(6,5) SWNT films (blue) outperform the hydrophobic PFO-BPy/(6,5) SWNT films (red) with higher on-currents and peak transconductances. The

increase in transconductance is up to 8-fold and is accompanied with a shift of the maximum towards lower gate voltages. Averaging the normalized peak values of the eight devices from the best substrate yields a transconductance of 51 µS, which is roughly 4 times higher than the average for the reference devices (see Table 4.1 in chapter 4.6) and also much higher in comparison to recently reported values for SWNT network ECTs of 0.44 µS.[13]

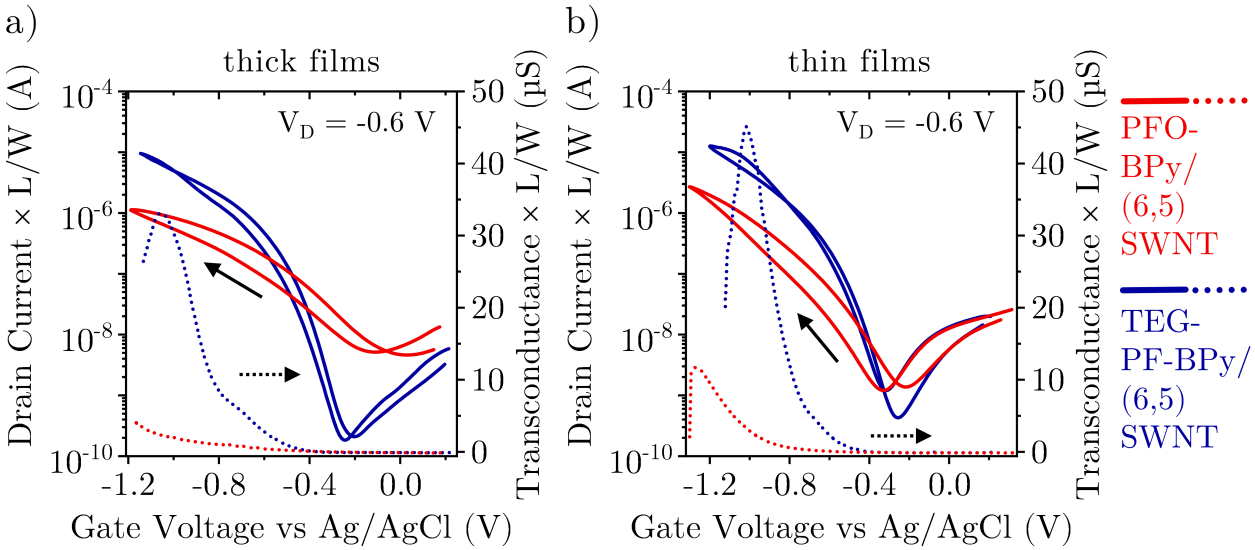

Figure 4.7: Channel dimension-normalized transfer characteristics (solid lines) and transconductances (dotted lines) of ECTs with a) thin and b) thick PFO-BPy/(6,5) SWNT (red) and TEG-PF-BPy/(6,5) SWNT (blue) films.

As mentioned in the introduction of this chapter (section 4.1), the impact of the active material on the normalized transconductance is defined by the product of their charge carrier mobility and the volumetric capactance μC^*. Therefore, an increase in ECT performance upon altering the material originates from an increase of one or both of these factors. Similar to the influence of hydrophilic ethylene glycol side chains on polymer ECTs, an improved volumetric capacitance is to be expected here. The mobility of SWNT networks is mostly determined by the network density, the chirality and the number of nanotube junctions,[58,65] all of which should remain constant upon performing a polymer exchange. However, a hypothetical way to affect the mobility would be a reduced charge screening, which could enable higher mobility pathways deep within the network, to become conductive.

In the following sections, the effect of the hydrophilic side chains onto the device characteristics is investigated in more detail to determine whether the above mentioned expectations are met.

4.4 Electrochemical Photoluminescence Quenching

An effective way to gain insight into the electrochemical or electrostatic doping of SWNT networks is to investigate photoluminescence quenching and trion emission in the near-infrared.[17,114,250] For that purpose, a separate batch of transistors was fabricated with interdigitated source-drain electrodes (see Figure 3.2c, W/L ratio of 10 000 µm/20 µm = 500), with a large gold side gate but without an electrode passivation layer. Comparable film thicknesses of ≈ 20 nm of TEG-PF-BPy/(6,5) SWNTs and PFO-BPy/(6,5) SWNTs were aerosol-jet printed. The devices were operated with ultrapure water in a gate voltage range of 0.5 to −1.0 V and a fixed source-drain bias of −0.1 V. After every gate voltage step, an equilibration time of 5 min was kept before acquiring a PL spectrum and recording the drain currents. The obtained data is visualized in Figure 4.8 as gate voltage-dependent plot, together with the as-measured spectra and normalized to the E_{11} peak.

With increasing hole accumulation in the nanotube networks at higher negative gate voltages, a clear PL quenching is observed for both materials, but is more pronounced for the hydrophilic TEG-PF-BPy/(6,5) SWNTs. While a small fraction of the E_{11} emission remains for the reference samples with PFO-BPy/(6,5) SWNTs even at −1.0 V, the E_{11} intensity for the hydrophilic counterpart drops down close to the noise level at that point. However, the most striking difference is noticeable in the normalized spectra (Figure 4.8c,f), where a distinct trion emission peak emerges for the films with hydrophilic wrapping-polymer. Being a charged exciton, trions can only form when free charge carriers are present within the network. Evidently, a better hydration of the TEG-PF-BPy/(6,5) SWNT films allows the electrolyte ions to completely penetrate the network and gate of the entire semiconductor. Ultimately, the hole accumulation is enhanced, which leads to both larger source-drain currents and stronger PL quenching.

Additional evidence that the more efficient water gating is enabled by the hydrophilicity of the tetraethylene glycol side chains is gained by comparison with ionic liquid ([EMIM][FAP]) gated PFO-BPy/(6,5) SWNT networks,[17,250] where complete PL quenching and pronounced trion emission was reported. Considering the very efficient gating of the SWNT networks in these reports with comparably much larger ions renders any possible influence of the polymer side chains on the morphology of the nanotube networks (*i.e.* pore size) unlikely. Since the

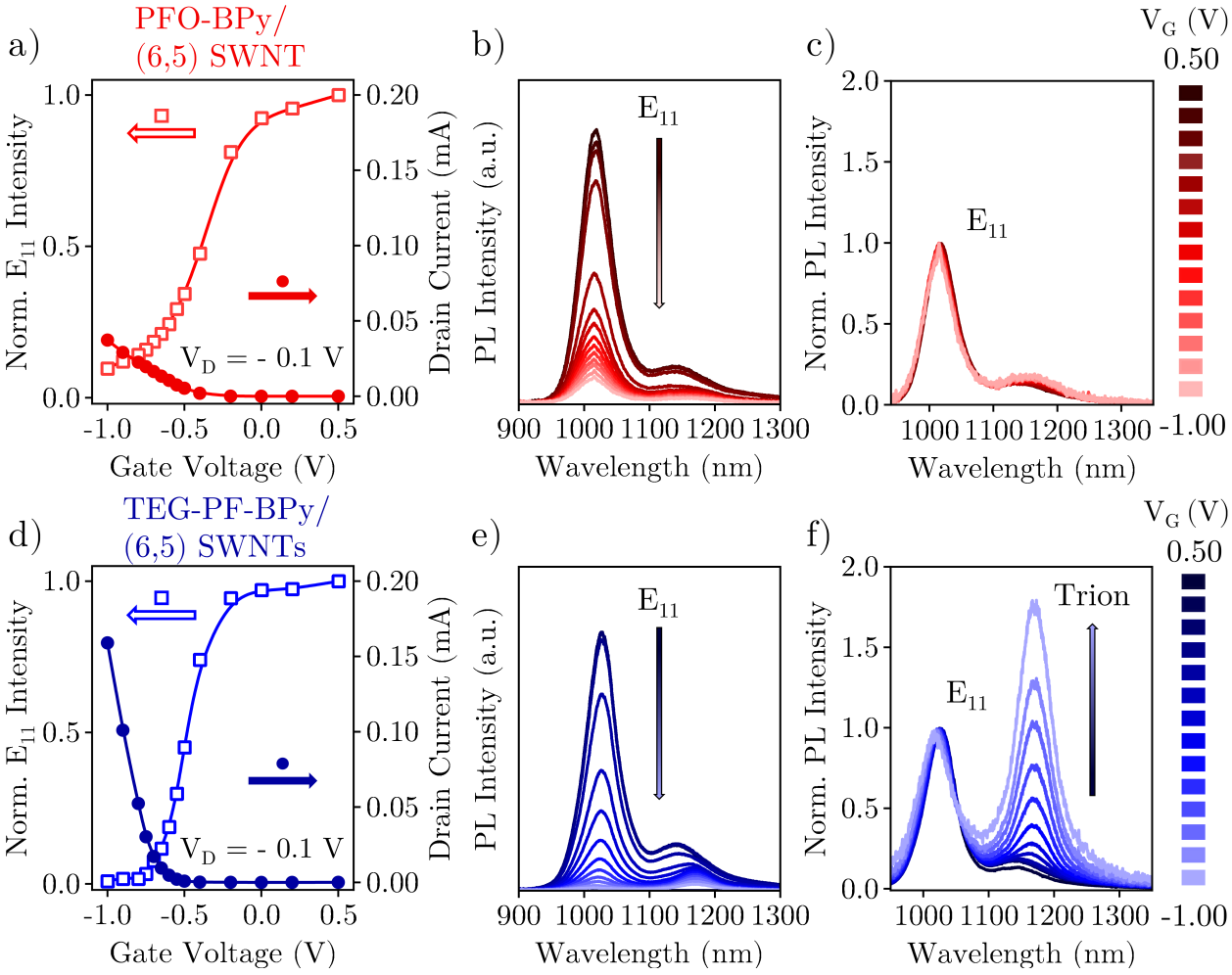

Figure 4.8: Gate voltage-dependent PL quenching of PFO-BPy/(6,5) SWNTs (top row, red) and TEG-PF-BPy/(6,5) SWNTs (bottom row, blue) in ECTs with ≈ 20 nm film thickness and a drain bias of $V_D = -0.1$ V. (a, d) Drain currents (solid circles) and normalized E_{11} PL emission (open squares) during a gate voltage sweep from 0.5 V to −1.0 V. (b, e) Development of the PL spectra under bias. (c, f) Gate voltage-dependent PL spectra, normalized to the E_{11} transition.

data in Figure 4.8 was obtained after a long equilibration time, faster ion diffusion through the network can also be excluded as a possible explanation of the trends.

4.5 Capacitance Determination by Electrochemical Impedance Spectroscopy

The enhanced transconductance values and the increased charge accumulation in the gated PL measurements are indicators for a larger volumetric capacitance as a consequence of the

polymer exchange to the hydrophilic TEG-PF-BPy. After the conditioning and acquisition of transfer and output curves, network capacitances were obtained from electrochemical impedance spectroscopy (EIS) by applying a sinusoidal voltage modulation of 10 mV with a frequency of 1 Hz in a bias range of 0 to −1 V (see chapter 3.4.1). The thickness-normalized capacitance values are plotted against the gate voltage in Figure 4.9 for thick an thin films of TEG-PF-BPy/(6,5) SWNTs (blue) and PFO-BPy/(6,5) SWNTs (red).

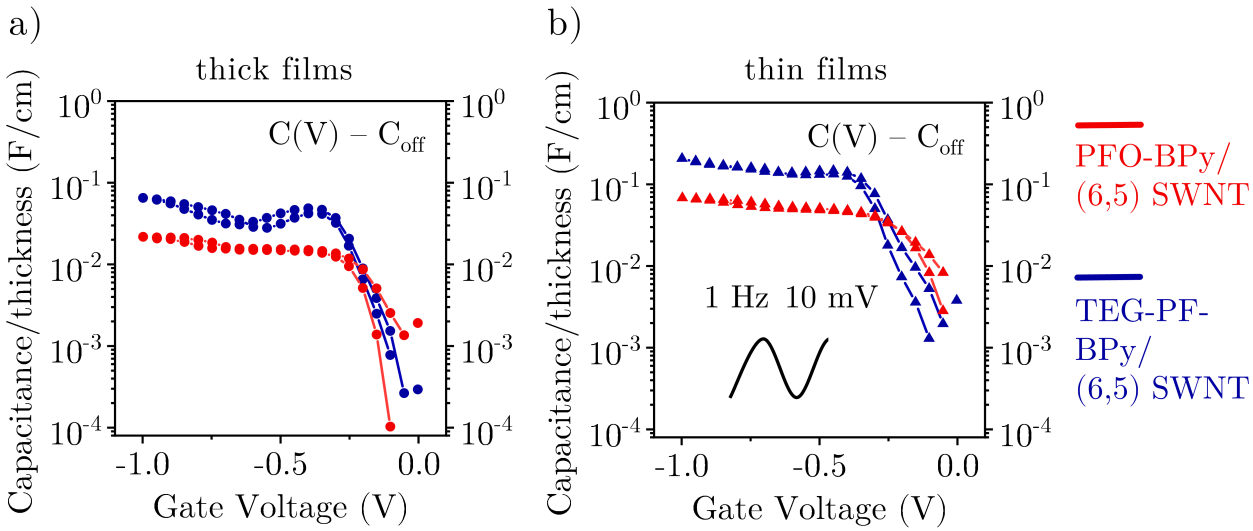

Figure 4.9: Gate voltage-dependent capacitances normalized by thickness and corrected for parasitic capacitances (off-capacitances were subtracted) as extracted from impedance measurements with a modulation of 10 mV rms at 1 Hz, for (a) thick and (b) thin films.

Note that despite the SU-8 passivation, a small parasitic capacitance was measured in the transistor's off-state around 0 V, which was substracted from the data to obtain the capacitance of the SWNT film. One can clearly see a steep rise in capacitance over several orders of magnitude with increasing negative gate voltages, as holes are accumulated in the network. The capacitance reaches a plateau when the network is fully charged and defines the maximum capacitance of the film. The maximum capacitances of the hydrophilic samples were significantly higher than the hydrophobic ones, regardless of the film thickness. After thickness normalization it becomes evident that in both cases, thicker SWNT layers are unfavorable for high volumetric capacitances. Although being viewed as open and highly porous material,[10] effects like charge screening and anisotropic charge transport prevent complete volumetric charging and hence the capacitance from scaling linearly with more layers. An average volumetric capacitance for the different sets of devices was determined

in Figure 4.10a by plotting the extracted maximum capacitances against the geometric film volumes and fitting linearly through the origin.

The total interfacial capacitance between the nanotubes and the electrolyte is composed of the intrinsic quantum capacitance[53] of the one-dimensional nanotubes and the double-layer capacitance. Since the quantum capacitance is defined by the nanotube's band structure which remains unaltered upon polymer exchange, only the double-layer capacitance is affected by the more hydrophilic side chains.

An effect that is well understood is the influence of increasing ion concentration in the electrolyte, which leads to a decreased Debye length because the ions pack more closely to the nanotube surface and the double layer capacitance is enhanced.[55,180] Although the quantum capacitance is much smaller and dominates the interfacial capacitance(see equation (2.18)), a larger double layer capacitance leads to an increase of the overall interfacial capacitance. As the applied gate voltage remains constant, a larger double layer capacitance increases the voltage fraction that drops across the quantum capacitance, indirectly increasing its value. A similar effect seems to occur when adding the tetraethylene glycol side chains, which act as ion coordination sites and allow the electrolyte ions to arrange closer at the nanotube surface, hence boosting the capacitance.

4.6 Device Performance

To compare the device performance and especially the capability of the newly developed TEG-PF-BPy/(6,5) SWNT networks with state-of-the-art polymers, the figure of merit μC^* is used. Typically, this product is extracted from a double logarithmic plot of peak transconductance in the saturation regime against the channel dimensions and operation conditions[165] as plotted in Figure 4.10b. According to equation (2.17) the product μC^* can be determined directly by fitting the data points linearly with a slope of 1 and extracting the y-intercepts. It follows:

$$\mu C^* = 10^{y-\text{intercept}}. \tag{4.1}$$

This graphical representation is very suitable to compare different ECT materials, because

it separates them according to their performance in terms of μC^* from top to bottom. Here, thick an thin films are treated like different materials, as the devices do not scale linearly with film thickness, as already observed in the capacitance measurements. In Figure 4.10b, data sets from different film thicknesses of the PFO-BPy/(6,5) SWNTs (red) and the TEG-PF-BPy/(6,5) SWNTs (blue) are symbolized by triangles (thin) and circles (thick) and connected by arrows. Evidently, the nanotube networks with the hydrophilic side chains of the TEG-PF-BPy surpass the hydrophobic references significantly both for thin and thick networks. In general, thinner films are beneficial for the device performance and exhibit much higher μC^* values and transconductance. The obtained μC^* values can be found in the summarizing Table 4.1.

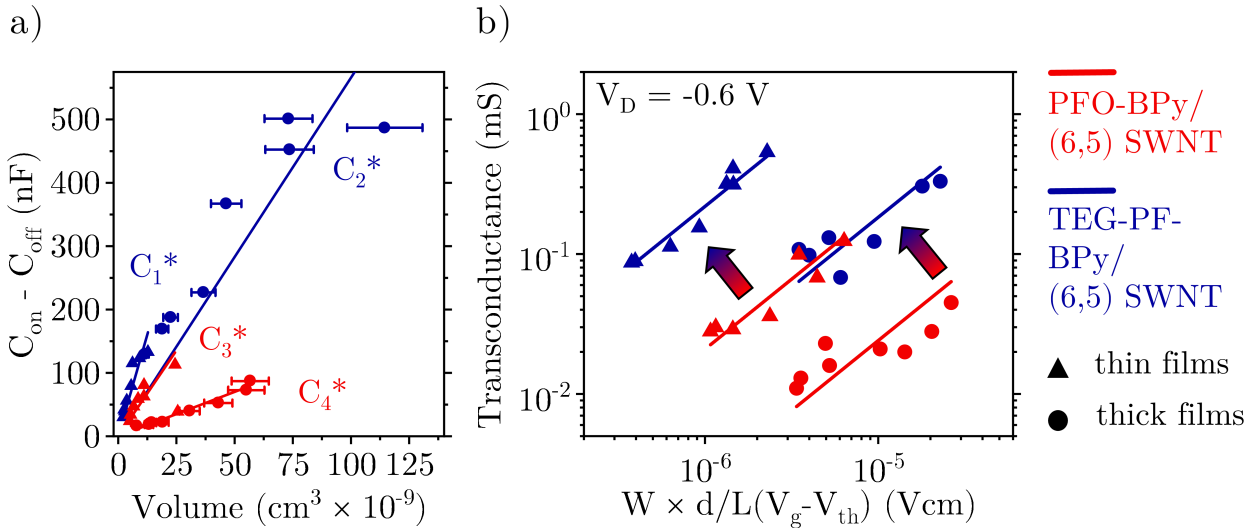

Figure 4.10: a) Net capacitances (on-values minus off-values) as a function of film volume for the determination of the volumetric capacitance of PFO-BPy/(6,5) SWNT (red) and TEG-PF-BPy/(6,5) SWNT (blue) networks. b) Saturation peak transconductance values against channel geometry and operation voltages for the extraction of the figure of merit μC^* utilizing the y-intercepts of the linear relation.

Thin films of TEG-PF-BPy/(6,5) SWNTs achieved the best ECT performances and gave a μC^* value of (219 ± 16) $\mathrm{F\,cm^{-1}\,V^{-1}\,s^{-1}}$, which is one order of magnitude higher than the best performing thin films of PFO-BPy/(6,5) SWNTs with (21 ± 2) $\mathrm{F\,cm^{-1}\,V^{-1}\,s^{-1}}$. This brings nanotube networks close to the figures of merit that are reached by the best-performing semiconducting polymers. For example, the glycolated polythiophene p(g2T-TT) was the benchmark material for ECTs for a long time with a μC^* value of 261 $\mathrm{F\,cm^{-1}\,V^{-1}\,s^{-1}}$, which was only recently surpassed by one of its derivatives with a value of 522 $\mathrm{F\,cm^{-1}\,V^{-1}\,s^{-1}}$,

based on an optimized side chain distribution.

The hole mobilities can be calculated by dividing the μC^* value, extracted from the fit in Figure 4.10b, by the C^* value, obtained from the fit in Figure 4.10a (μ_{fit}). Alternatively, one can calculate the mobilities directly from equation (2.17), using the peak transconductance and C^* values from the transfer characteristics and EIS measurements (μ_{calc}). The averaged μ_{calc} values and the μ_{fit} values overlap within one standard deviation and are comparable to previously reported values for (6,5) SWNT networks.[65] The mobilities are presented in Table 4.1 together with a summary of all extracted data. The volumetric capacitances of SWNT networks even with hydrophilic side chains are still inferior to those of glycolated polymers but due to intrinsically higher hole mobilities, decent μC^* values are reached. Both the more hydrophilic wrapping-polymer as well as thinner films are beneficial to reduce charge screening within the networks which is reflected by larger mobility values. Altogether, thin films of carbon nanotubes with hydrophilic wrapping-polymer outperform those with hydrophobic wrapping-polymer significantly and constitute a high transconductance material for ECTs in bioelectronics.

Table 4.1: Metrics for ECTs with Thin and Thick PFO-BPy/(6,5) SWNT and TEG-PF-BPy/(6,5) SWNT films: film thickness, volumetric capacitance C^*, normalized maximum transconductance g_{m}, figure of merit μC^*, hole mobility μ_{fit} from linear fits in Figures 4.10 and 4.9 and μ_{calc} from transfer characteristics; the data was averaged over eight devices with different W/L ratios for each film thickness and wrapping-polymer.

polymer/ SWNT hybrid	film thickness (nm)	C^* (F cm^{-3})	norm. g_{m} (µS)	μC^* ($\text{F cm}^{-1}\,\text{V}^{-1}\,\text{s}^{-1}$)	μ_{fit} ($\text{cm}^2\,\text{V}^{-1}\,\text{s}^{-1}$)	μ_{calc} ($\text{cm}^2\,\text{V}^{-1}\,\text{s}^{-1}$)
PFO-BPy/ (6,5) SWNT	31 ± 5	1.4 ± 0.1	5.3 ± 1.5	2 ± 1	1.4 ± 0.7	1.4 ± 0.2
	13 ± 3	5.4 ± 0.4	13.0 ± 2.2	21 ± 2	3.9 ± 0.5	3.5 ± 0.7
TEG-PF-BPy/ (6,5) SWNT	52 ± 13	5.7 ± 0.5	42 ± 16	19 ± 3	3.3 ± 0.6	3.6 ± 1.1
	6 ± 1	13 ± 1	51 ± 6	219 ± 16	16.8 ± 1.8	15.4 ± 2.8

4.7 Long-Term Stability

A common flaw of well-performing benchmark polymers in OECTs is their low stability under bias stress. With SWNTs being an inherently robust material,[251] the device stability was tested both in terms of operational stability in purified water and when exposed to PBS as a blood serum-like electrolyte. For that purpose, similar devices with respect to channel dimension and film thickness but also to the measurement history were employed. All stability measurements were performed after the above-mentioned transfer, output and capacitance measurements.

The long-term stability was investigated by switching the ECTs with a 20 s period, a gate voltage of −1 V and a duty cycle of 50 % (*i.e.* 10 s on/off). A constant drain bias of −0.1 V was applied and the drain currents after 3 min of equilibration monitored over 160 min are shown in Figure 4.11 for devices with PFO-BPy/(6,5) SWNTs and TEG-PF-BPy/(6,5) SWNTs.

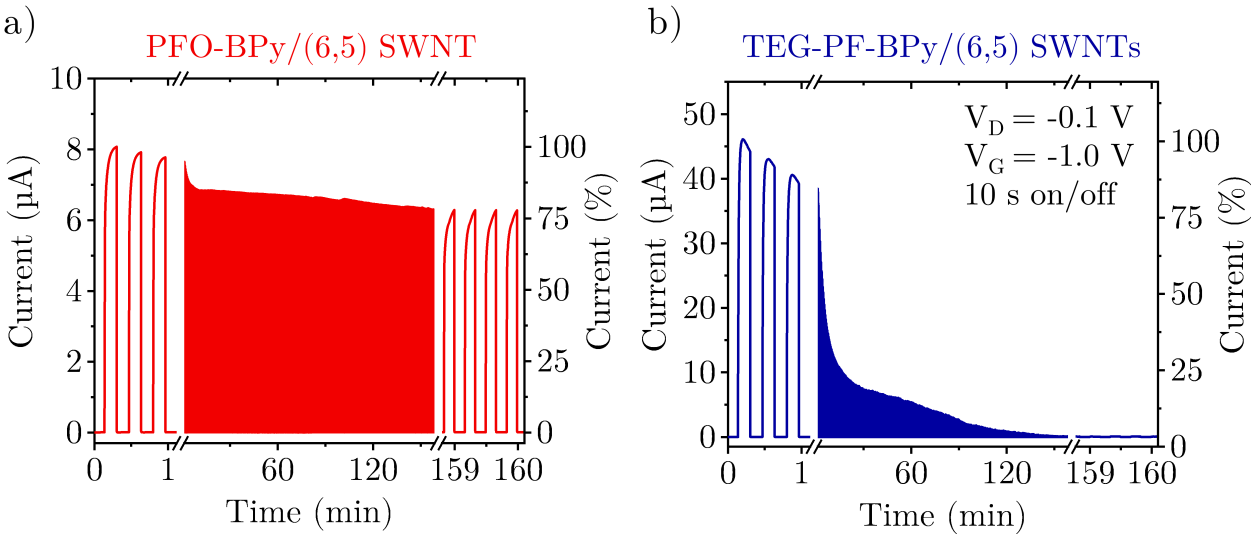

Figure 4.11: Time evolution of the drain currents at $V_D = -0.1$ V while switching between −1 V(on) and 0 V(off) gate voltage with 10 s pulses as a measure of the long-term stability of a) PFO-BPy/(6,5) SWNT and b) TEG-PF-BPy/(6,5) SWNT ECTs.

While in the beginning, the sample with hydrophilic film exhibits consistently higher currents compared to the hydrophobic counterpart, the performance drops drastically within the first hour of operation and the device breaks down completely over the course of the experiment. In contrast, the reference device shows a moderate device stability and the current only drops down to 75 %, which is similar to the values that are reached for previously reported

SWNT sensors[13] or the benchmark polymer p(g2T-TT),[176] however not competitive with recent developments with up to 98 % current retention.[167]

For glycolated polymer ECTs, the device stability is strongly linked to the hydrophilicity of the employed materials, which leads to swelling of the films and thus morphological changes during device operation that are harmful for charge transport. A similar effect might play a role for polymer-wrapped SWNTs with hydrophilic side chains, in a way that SWNTs lose contact and percolation paths are interrupted.

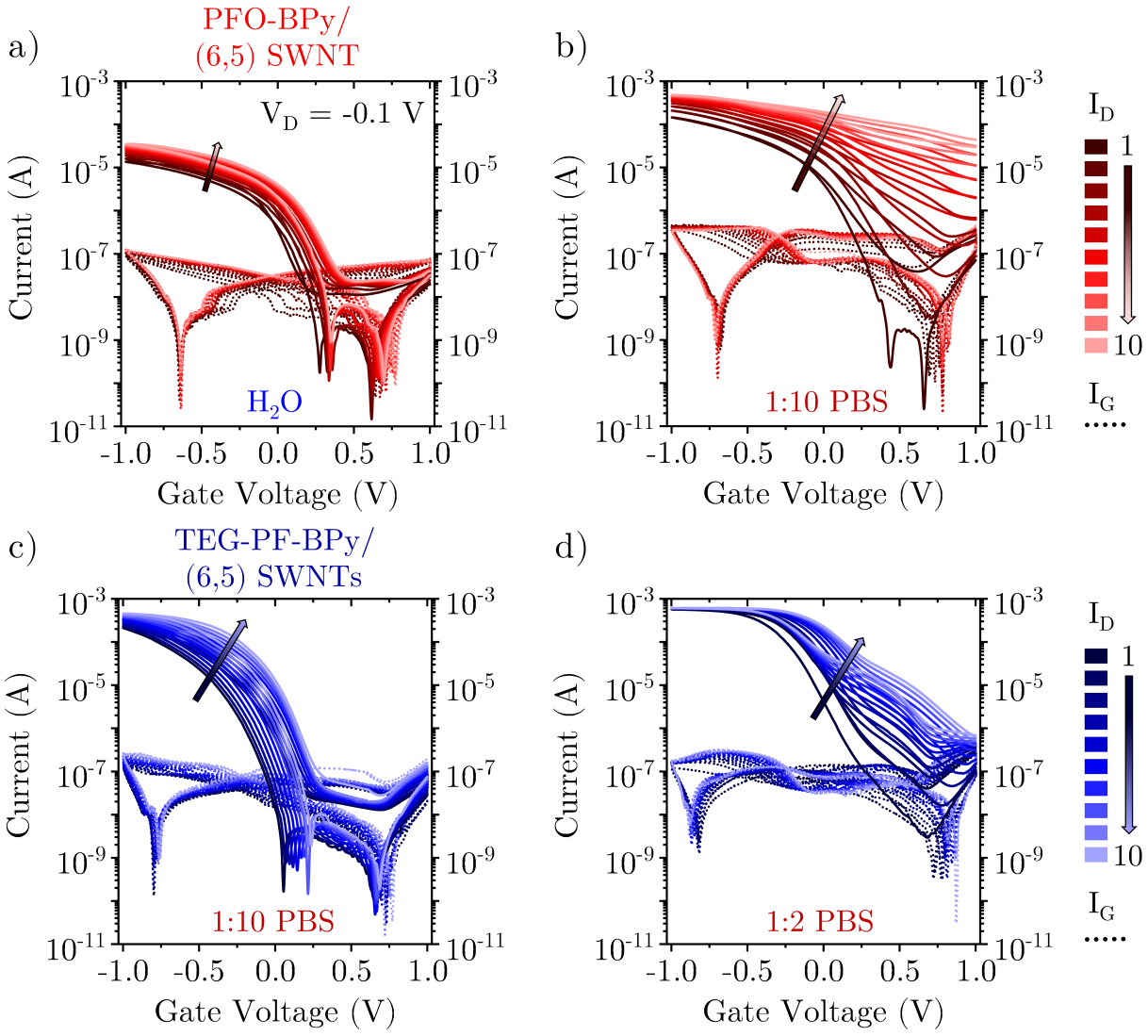

Figure 4.12: Conditioning with diluted PBS as the electrolyte to assess the biostability of ECTs. Comparison of devices with PFO-BPy/(6,5) SWNTs in a) ultrapure water and b) 1 mM PBS versus TEG-PF-BPy/(6,5) SWNTs in c) 1 mM PBS and d) 5 mM PBS.

The stability of the SWNT films towards serum-like electrolyte with high ionic strength was investigated on devices that were based on the layout used for the PL quenching experiments

(sections 3.3.1 and 4.4). Starting from ultrapure water followed by a 1 mM and a 5 mM PBS solution, the transistors were conditioned by ten consecutive transfer sweeps, respectively. Figure 4.12 shows that while the PFO-BPy/(6,5) SWNT device breaks down within a few transfer sweeps in 1 mM PBS, the TEG-PF-BPy/(6,5) SWNT ECT remains stable and shows remarkably steep transfer characteristics. However, already in 5 mM PBS, it also starts to degrade. When measuring the apparently more stable samples with hydrophilic SWNT films directly and only in 1 mM PBS, the devices were still not stable enough to allow for a complete electrical characterization.

Despite SWNTs being a chemically stable and in general durable material, both the long-term stability and the biocompatibility in serum-like electrolytes appear surprisingly poor. The applied operating voltage of -1 V is relatively high for ECTs with aqueous electrolytes and the stability could potentially increase for a narrower gate voltage range. However, this increase in stability would also result in a decreased transconductance and thus performance, since the peak transconductance lies around a gate voltage of -1 V. Reasons for the instabilities caused by the presence of the sodium, potassium and chloride ions in the PBS remain unclear and have not been investigated futher in this work. However, by comparing the degradation effect in PBS to the long-term stability tests in ultrapure water, it can be concluded that the devices that were exposed to PBS must follow a different, additional degradation mechanism, since the channel becomes more conductive with every measurement instead of breaking down.

4.8 Summary and Conclusion

This chapter discussed the influence of the wrapping-polymer of aerosol-jet printed (6,5) SWNTs onto the performance of water-gated ECTs. A large increase in peak transconductance and volumetric capacitance was achieved by exchanging the wrapping-polymer PFO-BPy, which possesses hydrophobic alkyl side chains, with a derivative featuring hydrophilic tetraethylene glycol side chains. The enhanced ion coordination is not only reflected by higher capacitances and transistor metrics, but a more thorough electrochemical doping was confirmed by *in situ* PL spectroscopy. Although the improved volumetric capacitances of the nanotube films do not reach those achieved with polymer semiconductors, good μC^*

values were obtained, owing to the nanotubes' inherently large charge carrier mobility. The highest figure of merit was found for thin films of up to 10 nm of TEG-PF-BPy/(6,5) SWNTs with $(219 \pm 16)\ \mathrm{F\,cm^{-1}\,V^{-1}\,s^{-1}}$, thus outperforming thin PFO-BPy/(6,5) SWNT films by an order of magnitude and advancing into ranges that make SWNT networks a competitor to state-of-the-art polymers. The long-term stability of the reference samples in this work showed comparable voltage cycling durability to previously reported SWNT based sensors.[13,14] However, both the long-term stability of the hydrophilic TEG-PF-BPy/(6,5) SWNTs as well as the stability in PBS of all samples was unexpectedly low. For polymers in ECTs usually the introduction of hydrophilic side chains leads to instable device operation due to swelling of the films.[252] Whether or not this is a possible explanation also for the instabilities in SWNT networks could be studied using electrochemical quartz crystal microbalance with dissipation monitoring (E-QCMD), similarly to polymer ECTs.[173,253] Many further improvements could be applied to the herein examined SWNT networks, like switching to larger diameter nanotube species[65] or by the creation of aligned networks with even higher carrier mobilities.[80]

Chapter 5

Artificial Synapses with Ion-Gel-Gated SWNTs

This chapter reports on slow ion diffusion in SWNT networks as mechanism for electrochemical artificial synapses and neuromorphic computing.

5.1 Introduction

In contrast to transistors with binary switching that require a high current on/off-ratio, much more precision is needed for artificial synapses and neuromorphic devices to fine tune the output current (*i.e.* the conductance) over hundreds of well separated and distinguishable levels. Artificial synapses are able to mimic the highly efficient and parallel computing mechanisms of the brain. Similar to synaptic connections in the brain which become stronger when participating in computing events, artificial synapses return a current that depends on the history of previous switching events. For this functionality, new organic electronic devices are being developed to potentially replace large and complex silicon circuits by energy-efficient single devices, that would revolutionize machine learning and artificial intelligence. In this newly and highly interdisciplinary research field, new materials and concepts are of interest. So far, the challenge of developing single-device artificial synapses has been approached by exploiting numerous materials and various processes with very different properties, such as localized conductive filament formation,[215] ion migration,[210,217,218] charge-trapping-based switching,[219–222] light-assisted reactions[223–225] or electrochemical redox-based switching.[18,164,226] The latter shows the most promising results and can be considered as state-of-the-art, featuring polymers like PEDOT:PSS,[164,206] P3HT[205] or p(g2T-TT)[231] as the active materials. In these devices, the basis on which synaptic functions such as short-term plasticity (STP), long-term plasticity (LTP) or spike-timing-dependent plasticity (STDP) are reproduced is the slow movement of electrolyte ions through the active material. A lot of development in recent years led to reports of highly controlled and reversible electrochemical doping of said polymers.[18,232] These advances resulted even in the first demonstrations of pattern recognition with crossbar arrays[133,232,233] and practical neuromorphic applications in robots.[231]

Another possible material for such applications are SWNTs, as they are highly suitable for electrolyte-gated applications as discussed in the previous chapters. So far, vertically aligned CVD-grown SWNTs have been explored which showed memristive switching, however not for the purpose of implementing synaptic functions.[254,255] Furthermore, circuits of SWNT transistors have been employed as neuromorphic system but not on the single-device level.[134] Additional reports on neuromorphic devices with SWNTs focused mainly

on charge-trapping[134] or light-assisted reactions as mechanisms.[256] A basic model of a spiking neuron using electrolyte-gated SWNTs was successfully reported which was able to mimic the integrate-and-fire mechanism of a biological neuron.[257] This system was further developed to instead implement synaptic functions like LTP and STDP, however without showing STP or the transition from STP to LTP.[258] The latest development of single-device SWNT artificial synapses was reported for back-gated SWNT networks on a silicon surface, making use of the large hysteresis of those devices.[133] However, the performance was hampered by the use of unpurified material with up to 10 % metallic nanotubes.

A very controlled electrochemical doping has also been reported for random SWNT networks, however in the context of electrochromic devices,[17] where the absorption characteristics of (6,5) SWNTs could be tuneed – depending on the charge accumulation in the network – precisely and reversibly on well-defined levels by pulsed operation. This system offers a great basis for the use as artificial synapse and as neuromorphic device. The electrochromic devices featured dense aerosol-jet-printed semiconducting (6,5) SWNT films, which were gated by an ion-gel as electrolyte and airbrush-sprayed semiconducting/conducting TUBALL™ SWNT networks as gate material.

Building one these electrochromic devices, this chapter demonstrates controlled electrochemical doping of (6,5) SWNT films by pulsed operation, which leads to synaptic behavior owing to the slow ion diffusion through the dense SWNT networks. Thus, the goal was to introduce SWNTs as promising new active material for electrochemical artificial synapses and potentially for neuromorphic computing.

In the following sections, first examples of electrochemical artificial synapses with (6,5) SWNTs as active material and TUBALL™ SWNTs as gating material are investigated.

5.2 Device Layout

The device architecture used here was adapted from previously studied electrochromic notch filters,[17] where the geometry and resulting electric fields were optimized to control the level of electrochemical doping of a semiconducting (6,5) SWNT film very precisely. Identical to the electrochromic devices, the samples in this chapter are based on a three-terminal electrode pattern with two parallel stripes for the source and drain and a relatively small side

gate that were deposited *via* standard photolithography onto a glass substrate (see Figures 5.1 and 3.2). A large U-shaped film of mixed metallic/semiconducting TUBALL™ SWNTs was airbrush-sprayed onto the gate pad and a dense network of purely semiconducting (6,5) SWNTs was aerosol-jet-printed into the channel area. To finish the devices, an ion-gel composed of the polymer P(VDF-HFP) and the ionic liquid [EMIM][FAP] was spin-coated as the electrolyte. The two AFM images in Figure 5.1 show the morphology of the SWNT films. One can see the very regular network from the monochiral (6,5) SWNTs with similar tube lengths in the lower image and above the broad diameter and length distribution of the TUBALL™ SWNT film, where the longest tubes tend to curl up, while smaller tubes fill up the pores.

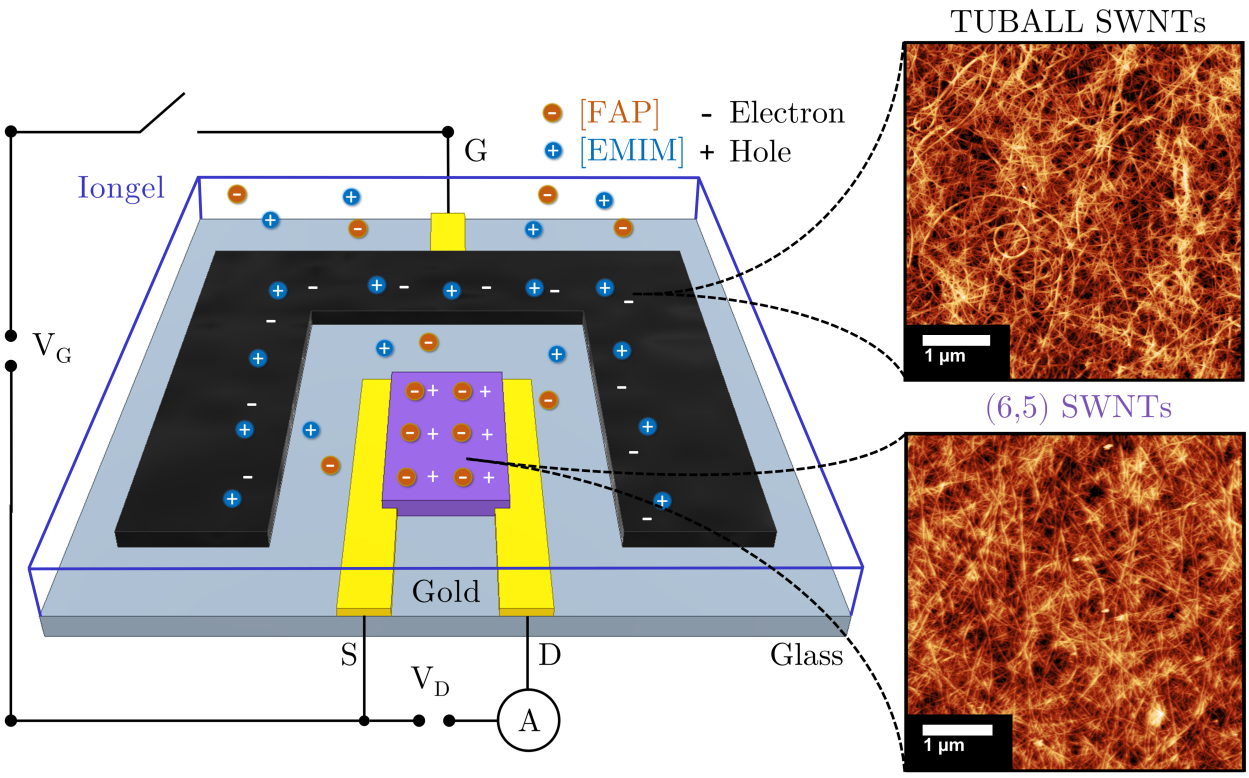

Figure 5.1: Schematic of the artificial synapse design and measurement setup with a channel length of 400 µm and a channel width, determined by the printed area of (6,5) SWNTs, of roughly 1200 µm. Thick networks of airbrush-sprayed TUBALL™ SWNTs and aerosol-jet-printed (6,5) SWNTs (AFM images) are gated with an ion-gel containing [EMIM][FAP] as the electrolyte. An analogue switch allows for pulsed operation and open-circuit condition.

This type of device was able to mimic synaptic functions, by viewing the applied gate voltage as the action potentials of the presynaptic neuron, the drain voltage as the activity of the postsynaptic neuron and the resulting drain current (or conductivity level) as the synaptic

strength between the two neurons.

In order to create synaptic behavior, which builds on the slow ion diffusion through the SWNT networks, the devices were operated with gate pulses and open-circuit condition in between pulses to gradually tune the potential between the gate and the channel, and thus precisely control the electrochemical doping. As indicated in the circuit in the schematic in Figure 5.1, an analog switch was used for that purpose, which was custom-built by the electrical workshop of the Institute for Physical Chemistry (see Figure 3.5) and could be controlled by a waveform generator.

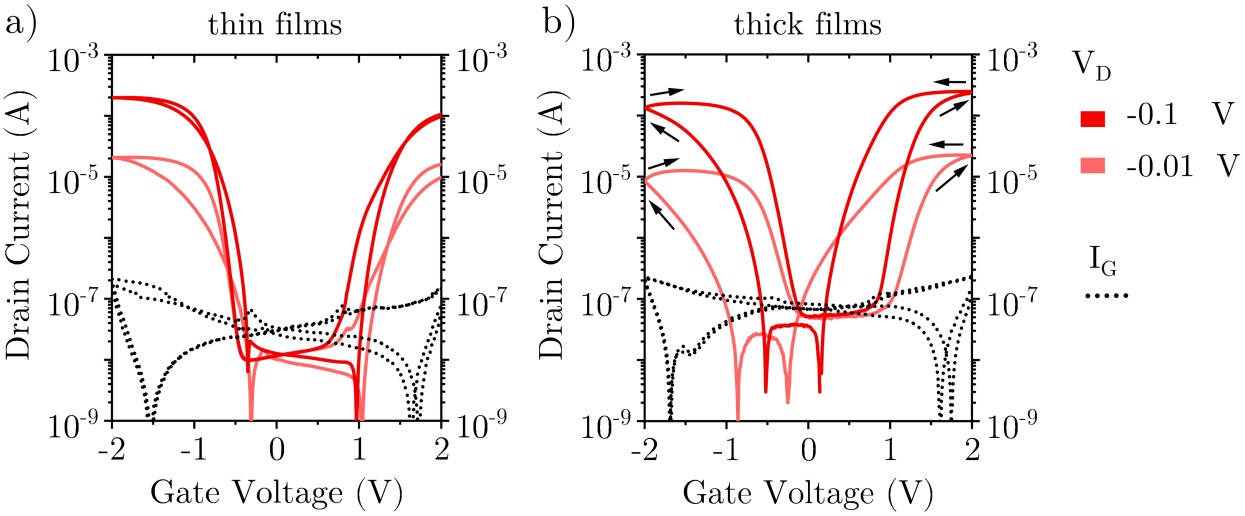

Figure 5.2: Linear transfer characteristics of the artificial synapses measured at a medium integration time of 20 ms and a step size of 0.01 V (corresponding to 0.5 V s^{-1}) for a) thin (10 nm) and b) thick (30 nm) (6,5) SWNT films. The arrows indicate the direction of the sweep and hysteresis.

The ion diffusion strongly depends on the film thicknesses of the employed airbrush-sprayed TUBALL™ and the aerosol-jet-printed (6,5) SWNT network. For a normal transistor a fast ion diffusion is desirable, since a decelerated ion diffusion leads to slower switching speeds and ultimately to a pronounced current hysteresis. While keeping the thickness of the TUBALL™-gate constant around 100 nm, the thickness of the (6,5) SWNT network was increased from 10 nm to around 30 nm by increasing the ink concentration for printing. In the linear transfer characteristics that were acquired with a medium integration time of 20 ms a substantial increase in hysteresis could be observed when going from thin to thick films, as shown in Figure 5.2. The arrows highlight the direction of the hysteresis, which

runs clockwise for the hole current and counter-clockwise for the electron current. While the origin of hysteresis in ECTs is not fully understood and can be the result of different effects,[259] this behavior indicates a slower ion diffusion. The fact that the ions cannot follow the electric field fast enough anymore becomes evident especially when looking at the behavior around a gate voltage of −2 V, where the drain current keeps increasing for a short time even upon sweeping back to the off-regime.
Unlike for a standard transistor, this hysteresis is a desired effect, as it allows to implement synaptic learning and computation mechanisms, as investigated in the following chapters.

5.3 From Short- to Long-Term Plasticity

The human brain is able to both compute and store information using a single mechanism: the plasticity of synapses. According to current understanding, synaptic plasticity is divided into STP that is mainly important for computation processes and LTP that is mostly responsible for learning and memorizing.[260] Each regime is attributed certain synaptic functions but there is a smooth transition between them.
One of the most basic functions of organic synapses associated with STP is paired-pulse facilitation (PPF), describing the short-term potentiation (*i.e.* increased synaptic strength) upon the arrival of two presynaptic spikes in quick succession. This behavior was very well imitated by the fabricated artificial SWNT synapses as shown in Figure 5.3a. While applying a constant drain bias of 0.1 V and two subsequent gate pulses of 1.5 V with a pulse width of 2 s and a period of 5 s, short current spikes could be triggered that dropped down to the noise level shortly after the gate pulses ended. Additionally, the second current spike was significantly larger (≈ 133 %), which translates into an increased synaptic strength that was programmed by the first pulse. By monitoring the gate voltage during the measurement (Figure 5.3a, top, blue), one can see the steady decrease of the open-circuit potential (OCP) after the applied pulse, which corresponds to a slow dedoping of the (6,5) SWNT network. However, upon the arrival of the second pulse, the ions are not fully equilibrated again and can diffuse deeper into the SWNT network. Therefore, the conductance of the channel depends on the history of previous gate pulses, which mimics the behavior of real synapses well and is the basis for further synaptic functionalities.

Another important step is the transition from STP to LTP, which describes the process of prolonged state retention and the formation of memory caused by a repeated stimulation.[261] Whether or not this transition is correctly displayed for the artificial synapses comprising SWNT networks was tested in a similar approach as for the PPF but instead of two distinct pulses, a series of 21 pulses was applied to the gate while monitoring the drain current (synaptic strength) and the OCP. Figure 5.3b clearly shows that with every gate voltage pulse, the drain current spikes higher and thus the conductivity of the (6,5) SWNT network increases, while at the same time, the states are getting more and more stable. Furthermore, the OCP stabilizes faster and at a higher level with every voltage pulse. This indicates that ions are penetrating the SWNT networks only partially within the short time of each voltage pulse but enter deeper and deeper layers of the network where their diffusion is slowed down continuously. As the time for the ions to equilibrate and leave the networks again increases, this leads to improved state retention and thus LTP.

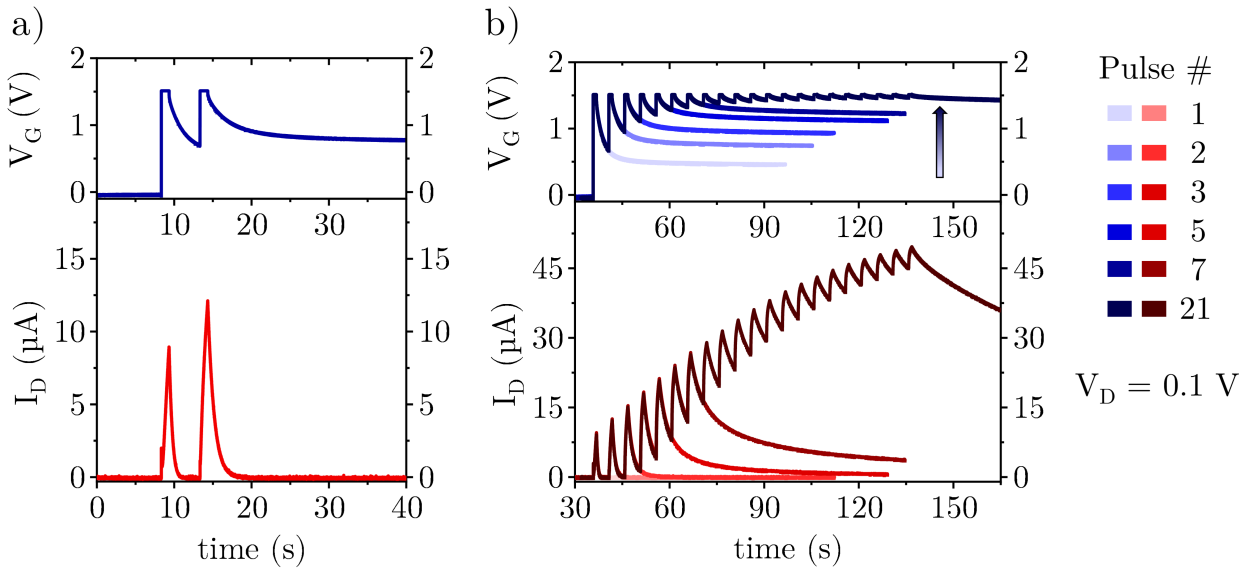

Figure 5.3: a) Short-term plasticity of artificial SWNT synapse representing the typical paired-pulse facilitation of a biological synapse. The blue curve on the topside shows the monitored gate voltage and the red curve below is the measured drain current. b) Transition from short-term to long-term plasticity by repeated stimulation over 21 identical gate pulses. With increasing pulse number, the measured currents are retained for longer time spans under open-circuit conditions.

5.4 Spike-Timing-Dependent Plasticity

A biological mechanism investigated in neuroscience that is closely related to STP but takes place on a more fundamental level is STDP.[196] By means of this mechanism the communication between neurons in the brain is described in a more elaborate manner and it explains how synaptic connections are selectively strengthened but also weakened. The decision whether the connection to a neighboring neuron should become stronger or weaker depends – as the name of the mechanism suggests – on the timing of the input. All inputs that arrive prior to a computation event of a neuron are causally linked and are classified as causal spikes. Synaptic connections to neurons that send causal spikes are strengthened (potentiation) and the closer in time the spike is received, the stronger the connection becomes. On the other hand, the synaptic strength to neurons that send inputs arriving too late to be part of the computation process (anticausal spikes) is decreased (depression). For spikes that arrive closely after the event, this depression is more pronounced.

In order to mimic STDP with the artificial SWNT synapses used in this work, both gate (presynaptic) and the drain (postsynaptic) voltages were applied as pulses. Figure 5.4a shows the applied pulse series and the current response in the synchronous case, were the presynaptic input and the postsynaptic output happen at the same time. In contrast to the previous measurements with continuous drain voltage the current response features sharp spikes that vanish immediately after the applied voltage pulses end instead of displaying slowly decaying states. Other than that, the learning behavior is identical and with every computation event, the synaptic strength increases.

The instabilities of the OCP between source and drain during the first few pulses (Figure 5.4a, green) may be attributed to the filling of volatile trap states within the (6,5) SWNT network. To exclude this effect from the STDP characteristics, the source current response of the 5^{th} pulse was taken as the reference. The effect of the spike timing on the plasticity was studied by shifting the series of source-drain voltage pulses by a small time interval Δt in positive and negative direction relative to the gate voltage series. The response of the system around the 5^{th} pulse is depicted in Figure 5.4b as the excitatory postsynaptic current (EPSC) against the time shift. The EPSC is calculated by – and normalized to – the current of the synchronous case I_0 and the current after the time interval $I_{\Delta\text{t}}$ according to

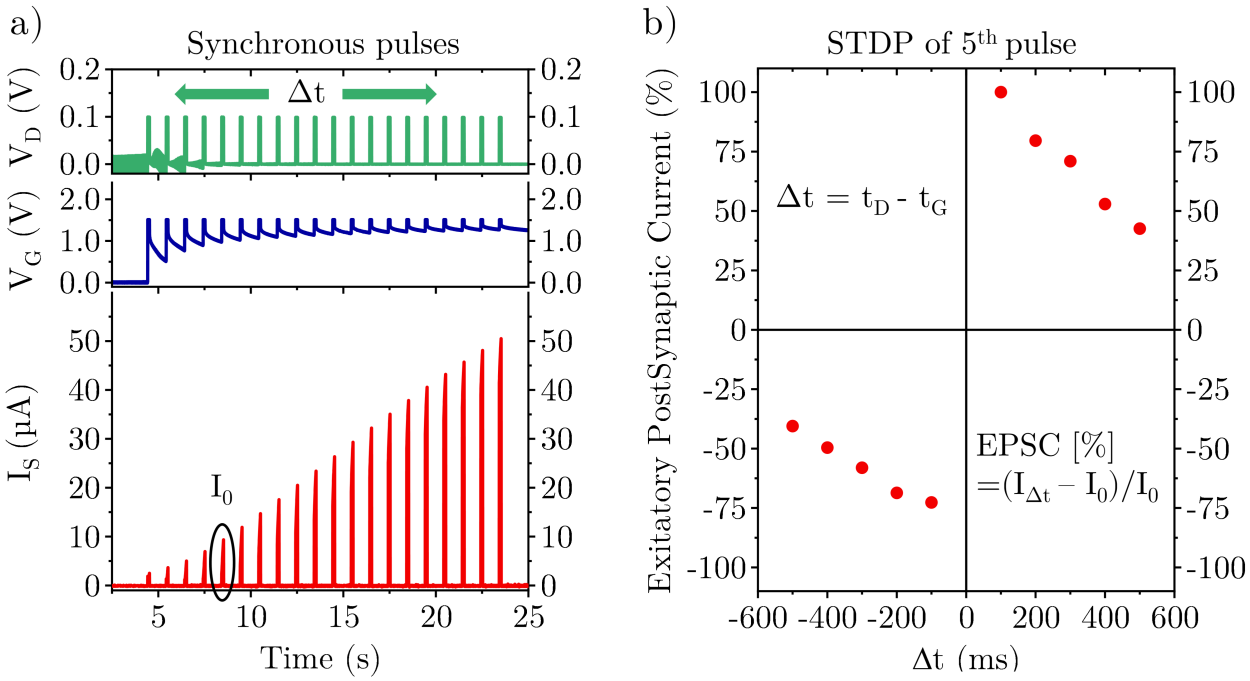

Figure 5.4: a) Operation of artificial SWNT synapses with synchronized drain (green, 0.1 V to OCP) and gate pulses (blue, 1.5 V to OCP) with corresponding source current (red). The source current the negative of the drain current, which however could not be measured in this configuration. STDP can be mimiced by changing the spike-timings by Δt. b) STDP characteristics evaluated for the 5th pulse in percent (normalized to the synchronous case, see equation inside the graph) by shifting the voltage sequences from a) in time.

EPSC $= (I_{\Delta t} - I_0)/I_0$. The normalization yields a percentage value relative to the reference pulse. Since Δt is defined as Δt$= t_D - t_G$, where t_G is the timing of the presynaptic gate pulse and t_D the timing of the postsynaptic drain pulse, negative Δt values correspond to anticausal spikes and positive values to causal spikes. In good agreement with the response of the biological counterpart (see Figure 2.11), the artificial synapse shows potentiation and depression for anticausal and causal spike timings, respectively. In addition, the response of the system is stronger for smaller time shifts and decreases when the pulses arrive with larger time gaps, correctly mimicking the behavior of the biological system. Note that only the qualitative response matches, since the magnitude of the signals in biological and artificial systems is completely different. While biological synapses conduct currents of pA, the SWNT synapses exhibit several tens of μA and conducting polymers several hundreds of μA.[18,231] Additionally, when comparing the timescales, the response of an artificial SWNT synapse in this work is roughly ten times slower than a biological one.[262] Furthermore, the potentiation and depression in Figure 5.4 follows an approximately linear function, rather

than approaching the axes asymptotically like a natural synapse.[263] This discrepancy is a result of the slow ion diffusion inside the dense SWNT networks, which on the other hand is a prerequisite to achieve long-term potentiation as discussed in the previous section. Therefore, depending on the application, this trade-off needs to be optimized, for example by adjusting the film thickness of the (6,5) SWNTs.

In conclusion, artificial synapses comprising electrochemically doped semiconducting (6,5) SWNTs and mixed conducting/semiconducting TUBALL™ SWNTs feature basic synaptic mechanisms like STP and LTP while also being capable of displaying more complex and fundamental synaptic characteristics like STDP.

5.5 Controlled Potentiation and Depression for Neuromorphic Computing

Artificial synapses and their ability to simulate biological computation mechanisms are investigated as building blocks for new computation hardware beyond classical silicon technology.[19,200,228,264] However, the requirements for artificial synapses when trying to mimic the biological system as closely as possible are very different, if not contradicting to the requirements that must be fulfilled in order to work as a component for a functioning neuromorphic computing chip.[19] Especially the volatile character of biological/artificial synapses and their way of computation like for example the transition between STP and LTP is not compatible to state-of-the-art machine learning algorithms on silicon-based artificial neural networks (ANNs). Instead, long-term memory is necessary to prevent the loss of information or ambiguous results. For artificial synapses to be able to replace silicon circuits in ANNs in a non-von-Neumann approach, they need to meet very strict specifications.

As summarized in chapter 2.3.3, an ideal neuromorphic computing device must be switchable over a large range of well-distinguishable conductance states in a very controlled way. Controlled switching implies linear and symmetric conductance steps both towards higher and lower conductance states, meaning that the steps are equidistant regardless of the history of previous switching events. Throughout the whole switching range, the conductance levels must be as stable as possible in time and the power consumption for every switching event

should be as low as possible, preferably as energy-efficient as the brain ($< 1\,\mathrm{fJ}$)[19,265]. Note that these characteristics need to be achieved with identical presynaptic gate voltage pulses to allow for a "blind" and parallel update of synaptic weights when implemented in an ANN array.

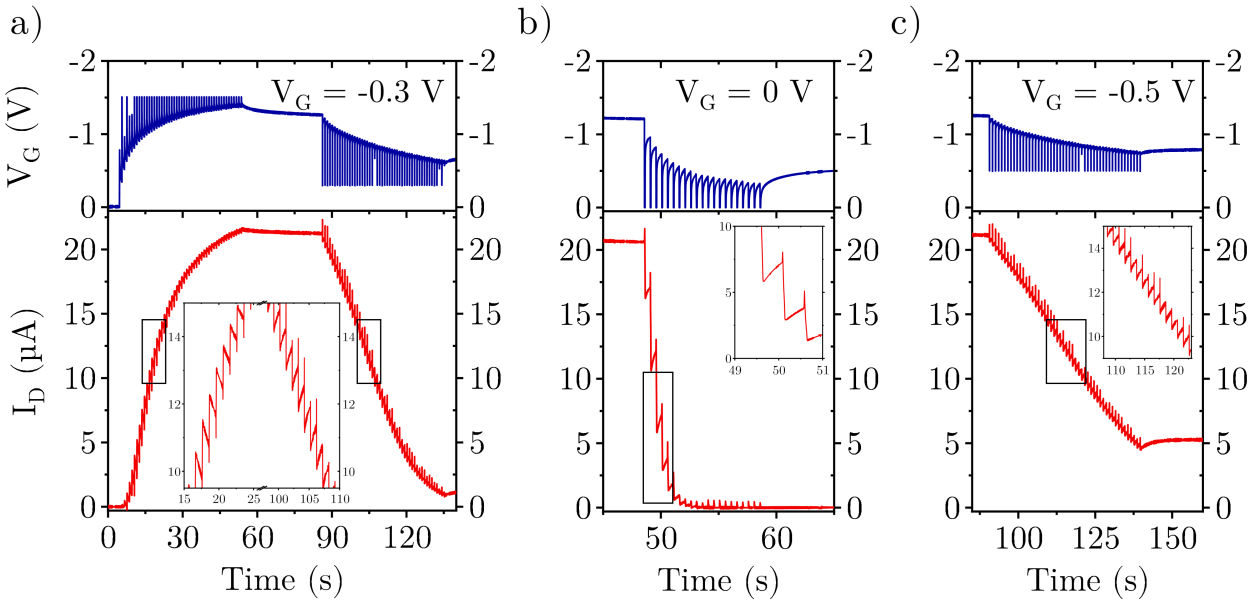

Figure 5.5: a) Optimized operation voltages and timings for a controlled, linear (inset) and symmetric potentiation and depression. Unsymmetrical depression for the same device when applying b) too small and c) too large negative presynaptic gate voltage pulses.

Many of the above-mentioned criteria are interdependent, making it difficult to find the optimal parameters for device fabrication but also device operation. The applied voltages and pulse timings were optimized for the best trade-off between linearity, symmetry, retention time and the number of conductance states. In Figure 5.5a one can see the optimized behavior, where a postsynaptic potential of $-0.01\,\mathrm{V}$ was chosen to monitor the conductance states. First, a potentiation was triggered by 50 presynaptic pulses of $-1.5\,\mathrm{V}$ with a period of 1 s and a duty cycle of 5 % (50 ms). After that, the system was left for 30 s at open-circuit condition to assess the state retention, followed by a depression over 50 pulses of $-0.3\,\mathrm{V}$ with a pulse period of 1 s and a duty cycle of 1 % (50 ms). For this presynaptic input, the postsynaptic output, represented by the drain current, shows that the artificial SWNT synapses can be potentiated and depressed in a very controlled way. The conductance changes linearly over the majority of the total range of the device (see inset Figure 5.5a). This linearity can be observed for both the potentiation and depression, leading to a very symmetric on-

and off-switching over 50 applied pulses, respectively. Only slight changes in the applied potentials triggered completely different responses as shown in the examples in Figure 5.5b and c. There, the potentiation branch is not shown but was identical to the experiment in a). The depression in b), when applying 0 V instead of −0.3 V, discharged the (6,5) SWNT network rapidly and within a few pulses (roughly 80 % within the first 5 pulses). In contrast to that, when applying −0.5 V over 50 pulses, the network was not fully discharged and the system stabilized with a drain current of around 5 µA. The fact that subtle changes in the operation voltage have such a dramatic effect on the device response leaves a narrow margin for batch-to-batch and device-to-device variations which are a common problem in organic electronics especially with printing and airbrush deposition techniques.

Being intended to mimic biologic synaptic behavior, the state retention of the first few states was very poor (STP), which becomes visible in the inset in Figure 5.5, but stabilized after completing all 50 pulses (LTP). The highest drain current state lost only approximately 1 % of its initial value over 30 s, which surpasses the stability of many reported systems[218,223,266] but is still far less stable than state-of-the-art electrochemical devices with a 0.04 % change over 24 h.[19] The energy consumption per switching event is calculated according to equation (2.19) and lies for the potentiation with presynaptic pulses of −1.5 V and pulse widths of 50 ms in the µJ–nJ regime for the highest and lowest conductance states, respectively. At least 5 times lower energies are needed for the depression because of the lower potential. While this is still a large power consumption and far from the pJ regime that is reached by the brain there are still a lot of options for improvements. A possible strategy to lower the energy consumption would be to shrink the device dimensions[19] of the herein studied bulky prototypes, which would be necessary for integration into arrays in any case.

A major difference to state-of-the-art artificial synapses with for example PEDOT:PSS is the semiconducting nature of the (6,5) SWNTs used in this work. Employing a semiconductor in theory offers more energy efficiency, since all devices that are not addressed remain off and carry no currents, reducing the power dissipation in an idle state drastically. However, the fact that linear switching and stable conductance states of (6,5) SWNTs are only reached for the highest conductances, where a lot of training is necessary to reach them, limits the energy efficiency. Additionally, being able to operate devices with conductive polymers around their charge neutrality point has been shown to be essential for stable and well-defined con-

ductance state programming.[18]

Overall, the electrochemical SWNT synapses fulfilled the required specifications only partly and in different regimes. A good linearity was mainly given in intermediate conductance states, while a considerable state retention was only given for high conductance states. Symmetric potentiation and depression was possible but only for optimized voltages and pulse timings. The given conductance range and signal-to-noise ratio was sufficient to program 50 very well distinguishable conductance states, which could be extended further depending on the application.

However, improvements would be needed to transfer the herein investigated electrochemical SWNT synapses to suitable neuromophic computing components. This would require a development away from the synaptic behavior with the transition from STP to LTP and the resulting STDP mechanism, toward a stable state retention over a large range of conductance states. Two possible ideas to improve the state retention are passivation of electrodes to reduce parasitic capacitances and electrical conditioning to reach more stable device operation. These two approaches are briefly investigated in the next section.

5.6 Electrode Passivation and Conditioning

As already discussed in chapter 4, both the passivation of electrodes to reduce the influence of parasitic capacitances as well as electrical conditioning of devices have a large impact on the behavior of the investigated systems (or ECTs). Parasitic capacitances are very likely to affect the state retention negatively, as they are able to withdraw charges from the (6,5) SWNT and the TUBALL™ SWNT networks when switching to OCP, which results in volatile conductance states. The largest contributing parasitic capacitance are the bare gold electrodes which in the prototypes in the previous sections were in direct contact with the ion-gel. Similarly to the approach in the previous chapter, this electrode area was passivated by an insulating photoresist (*i.e.* SU-8) through an additional photolithographic step in the device fabrication. As shown in the optical microscope and SEM images in Figure 5.6a and b, the SU-8 layer was patterned after the deposition of the SWNT films, leaving a small contact area at the source and drain electrodes uncovered to ensure that also the SWNTs in contact with the electrodes are properly gated.

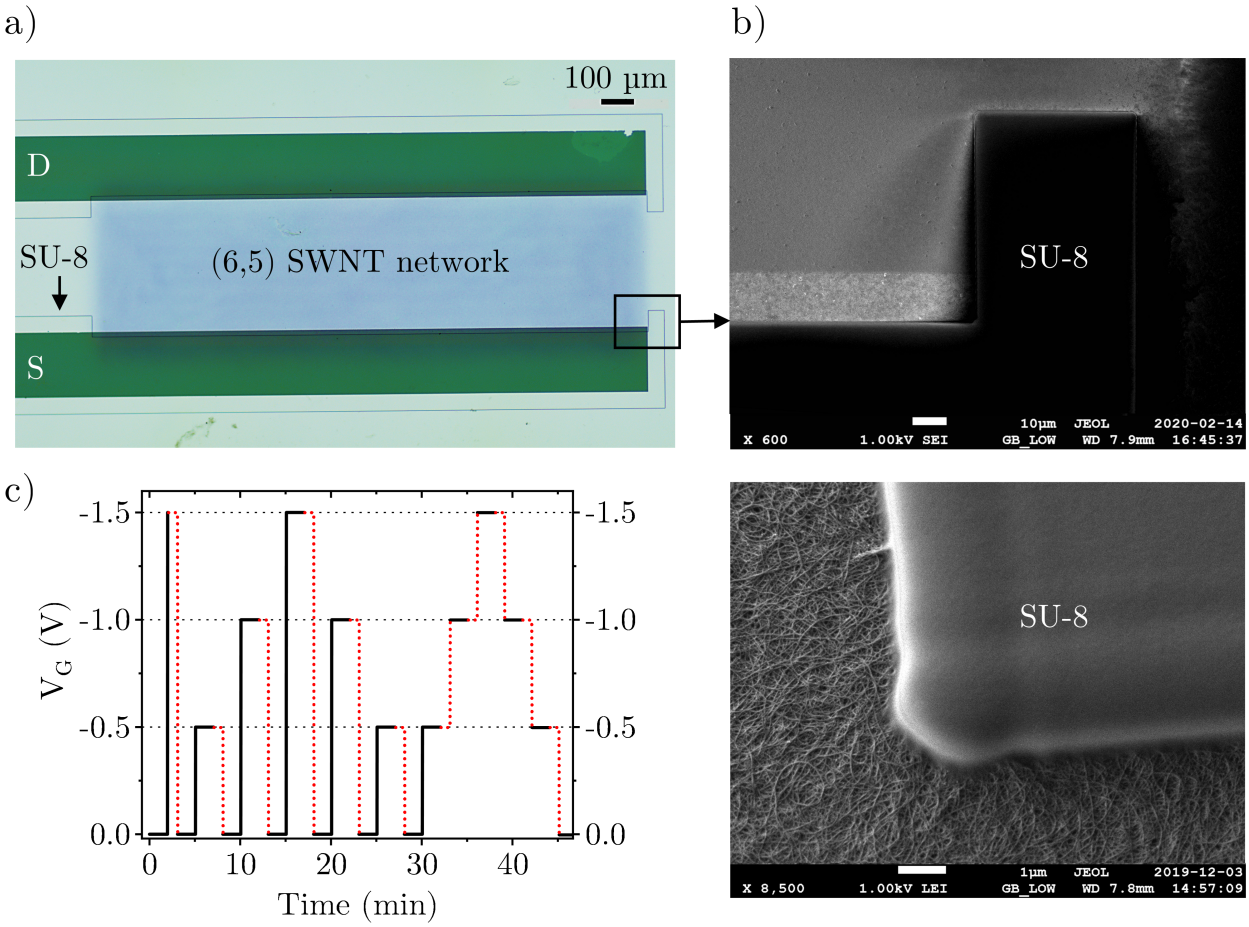

Figure 5.6: a) Optical microscope and b) SEM images of SU-8-passivated electrodes. c) Gate voltage sequence for the electrical conditioning of artificial SWNT synapses. The red dotted line indicates open-circuit condition.

In addition to this passivation, the electrical measurements were complemented by a thorough electrical conditioning of the devices prior to each measurement. During the first few voltage cycles, the charge accumulation inside the SWNT networks is enhanced due to the electrolyte ions penetrating deeper into the porous SWNT networks, as discussed previously for the water-gated ECTs. Removing ions that are coulombically bound to charges on the nanotubes located deep within the SWNT networks occurs on much longer timescales than for ions from the outer layers. This would imply that conductance states that are programmed after conditioning should be persistent. With that in mind, the transition from STP to LTP and the much better state retention for high conductance states that is visible in Figure 5.5a might be partially a conditioning effect. Therefore, performing conditioning prior to each measurement could increase the state retention in general. For this purpose,

the voltage sequence in Figure 5.6c was cycled over night, switching the devices on and off in mostly −0.5 V gate voltage steps with a maximum of −1.5 V.

Finally, the passivated and conditioned devices were tested primarily for their ability to retain a programmed conductance state. A simple experiment was chosen for that purpose, consisting of two identical gating steps with a gate voltage of −1.5 V over more than 120 s, each followed by at least 120 s of open-circuit condition. Over the course of this experiment the drain current was monitored as shown in Figure 5.7a, where the open-circuit phase is shaded in light blue. The light red curve showing the device behavior prior to the conditioning indicates that the SU-8 passivation alone already had a positive effect on the state retention, since the current only dropped by about 0.2 % within 120 s instead of up to 1 % within 30 s as it was the case without passivation. Surprisingly, during the second open circuit step the current even increased slightly. This effect was significantly more pronounced after the overnight conditioning as illustrated by the dark red curve. In both the first and the second open-circuit step after the conditioning the current kept increasing significantly by about 5 % of the value after the programming step. Overall, the current range was extended by the conditioning by up to 50 %, indicating that the (6,5) SWNT network was much more thoroughly gated and apparently better infiltrated by the electrolyte ions.

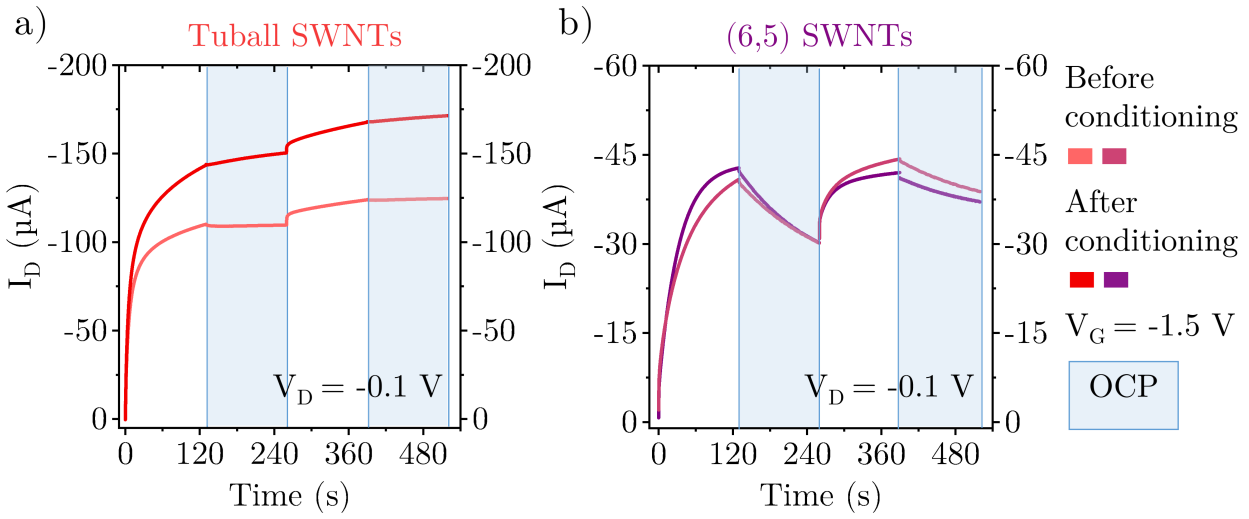

Figure 5.7: State retention measurements of SU-8-passivated artificial synapses before and after electrical conditioning with two identical gating and open circuit steps. Resulting drain current for a) mixed TUBALL™ SWNTs and b) semiconducting (6,5) SWNTs as the gate material.

So far, the reason for the current increase upon switching to open-circuit remains unclear but is a crucial effect to understand, because after programming a specific synaptic strength, neither a conductance decrease nor an increase but a stable state retention is required. Probably, this effect stems from the complex morphology and electronic landscape of the TUBALL™ SWNT network with many different nanotube lengths and diameters as well as the intermixing of conducting and semiconducting nanotubes.

A first step to achieve more insight into the device dynamics and the contributions of the employed components was to reduce the complexity of the system by exchanging the spray-coated mixed network of TUBALL™ SWNTs acting as the gate electrode with an aerosol-jet printed (6,5) SWNT network of equal thickness. This way, the system was reduced to only semiconducting nanotubes and one SWNT chirality. Apart from that, the device fabrication was identical and the obtained samples were tested again before and after an overnight conditioning with respect to their state retention. Three major differences can be observed in Figure 5.7b, which shows the current response for an all-(6,5)-SWNT artificial synapse. First, the overall current range is significantly lower than for the devices with mixed TUBALL™ SWNT gates. Second, the conditioning effect is marginal and third, the state retention during the open-circuit phase is much worse. This indicates that the TUBALL™ SWNT film is a key component for the synaptic devices in general and needs to be investigated in detail to be able to optimize it specifically for a stable state retention. A theoretical explanation for the improved state retention and the susceptibility to conditioning of the TUBALL™ films could be electron traps. There is evidence, that TUBALL™ SWNTs exhibit higher defect densities than other SWNT materials.[267,268] It is also likely, that the complex energy landscape from the various nanotube diameters leads to trapping sites, especially at the interfaces between metallic and semiconducting species. Filling these electron traps *via* electrical conditioning prior to measurements could be the reason for a larger current range compared to unconditioned devices. Since trapped charges require energy to detrap and become mobile, they might have a stabilizing effect also on the electrolyte ions, which could explain the improved state retention. However, the increasing currents during open circuit phases are still a peculiar phenomenon, that requires more experimental and theoretical input to be explained.

5.7 Summary and Conclusion

In this chapter electrochemical transistors with an ion-gel-gated semiconducting (6,5) SWNT network in the channel and a mixed semiconducting and metallic TUBALL™ SWNT network as the gate have been investigated as prototypical artificial synapses and their viability for neuromorphic computing has been assessed. The emulation of basic synaptic functions like STP or LTP and the transition between them as well as fundamental learning mechanisms like STDP have been demonstrated. The behavior of biological synapses was reproduced qualitatively, although the time scales of the processes of the artificial synapses were about 10 times slower. An easy way to improve the switching speed and device response drastically is scaling down the device dimensions, especially the channel length. A miniaturized device architecture would also reduce the high energy consumption on the order of nJ, which is essential for implementation in an array configuration for vector-matrix multiplication.

Artificial carbon nanotube synapses showed promising behavior for the use as neuromorphic devices, like linear and symmetrical potentiation and depression over a large conductance range. However, the artificial synapses exhibited mostly volatile behavior, that is necessary to mimic functions of biological synapses such as STP and STDP. To be able to constitute a viable alternative to state-of-the-art neuromorphic polymer devices[18] the state retention has to be improved significantly. For that, it was shown that the interplay between the two nanotube networks and the ion-gel has to be investigated in more detail and a more elaborate passivation of parasitic capacitances is helpful. Passivation is especially important when moving to array configurations, where cross-talk between devices could become an issue. Furthermore, it was observed that a mixture of semiconducting and conducting nanotubes as gating material (*i.e.* TUBALL™ SWNTs) is favorable for the state retention instead of purely semiconducting nanotubes. Additionally, the electrical conditioning of artificial synapses was introduced as an important tool to achieve less volatile conductance states.

The great research interest in electrochemical doping/dedoping of conducting polymers has led to remarkably well-defined and controlled switching around their charge neutrality point, which explains their success in neuromorphic applications.[18,19,206,231] A major difference and potentially decisive advantage of semiconducting SWNTs over conducting polymers as the active material of electrochemically driven artificial synapses or neuromorphic devices is the

theoretically lower power consumption in a later application. Semiconducting SWNTs are initially non-conducting and only specific devices in an array would become conductive with training, leading to low currents and low energy dissipation. Vice versa, conducting polymers (*e.g.* PEDOT:PSS) always carry comparably large currents on the order of hundreds of µA.[18,231]

In conclusion, ion-gel-gated networks of (6,5) SWNTs as active material with TUBALL™ SWNTs as gating material have been shown to perform well as artificial synapses. For their application as neuromorphic devices, more detailed insights into the ion diffusion in connection with the TUBALL™ SWNTs is required to understand the decaying or increasing conductivity of the (6,5) SWNT network under open-circuit conditions.

Chapter 6

Conclusion and Outlook

This chapter summarizes the findings of this work and addresses open questions that need to be answered in future studies.

The early days of carbon nanotube research were focused on harnessing the highly desired properties of this nanomaterial in basic devices such as field-effect transistors. For this purpose, purification, synthesis and processing methods were heavily researched. By now, the field has reached a state, where many purification methods as well as processing techniques are well-established and SWNTs have proven to be a high-performance material for various electronic components. Additionally, customized functionalization routines have been developed that enable tuning the electrical and optical properties of SWNTs for specific applications.

SWNTs also offer great potential (flexibility, stretchability) for applications in bioelectronics, in particular for sensors based on water-gated transistors. Owing to the high selectivity towards semiconducting nanotubes, polymer-wrapping of SWNT raw material is the arguably most suited chirality-sorting method for transistor applications. However, standard wrapping-polymers like PFO-BPy with alkyl side chains are inherently hydrophobic. While this provides stability in organic solvents, it also limits the interaction of SWNTs with aqueous electrolytes. One way of functionalizing and altering the properties of this hybrid material after the purification and selection process is the polymer exchange method developed and utilized in recent years.[113,114] Using this approach, in combination with a polymer that features hydrophilic oligoethylene glycol side chains instead of alkyl side chains, a more hydrophilic polymer/SWNT hybrid was created and investigated in the first part of this work.

Dispersions of (6,5) nanotubes wrapped with TEG-PF-BPy showed improved colloidal stability in toluene, which was monitored by time-dependent PL spectroscopy. This side-effect is beneficial for device fabrication and device reproducibility. SWNTs with hydrophobic and hydrophilic wrapping-polymer were then incorporated as active material in water-gated electrochemical transistors *via* aerosol-jet printing. Electrical characterization of these devices showed a significant performance increase due to the pegylation, which was caused by a larger volumetric capacitance of the more hydrophilic films. The attached ethylene glycol side chains provide coordination sites for the hydronium and hydroxide ions, promoting a more efficient electrochemical doping and thus a higher effective capacitance of the SWNT layer.

Further evidence for the improved charging was gained from *in situ* PL spectroscopy as a

measure for the degree of electrochemical doping. The pegylated films showed enhanced charge accumulation by more pronounced PL quenching and considerable trion emission. The performance of both SWNT materials for the use in ECTs was assessed by extracting the product of charge carrier mobility and volumetric capacitance. Thin networks of up to 10 nm of the newly created hydrophilic polymer/SWNT hybrid yielded the best metric with $(219 \pm 16)\ \mathrm{F\,cm^{-1}\,V^{-1}\,s^{-1}}$. This value constitutes an improvement compared to PFO-BPy polymer-wrapped SWNTs by an order of magnitude and matches those reported for state-of-the-art semiconducting polymers with optimized side-chains.

These findings are an important step towards high-performance ECTs based on SWNTs, but nevertheless some open questions remain to be answered. An important issue to address is the poor device stability observed so far. Both the long-term stability and the operation with serum-like electrolytes of higher ionic strength were unexpectedly poor and the reasons for that could not be resolved yet. The pegylated SWNTs exhibited a much worse durability against voltage cycling than the reference samples. In contrast to that, they showed improved stability in buffer solution, but unfortunately, still insufficient for applications in bioelectronics. The stability in polymer ECTs is usually limited by the swelling of the polymer films, which negatively affects the charge transport.[174] A common tool to monitor the water uptake and swelling are E-QCMD measurements.[252,253] To which extend swelling is also an issue for the herein investigated SWNT networks could be estimated by performing such measurements. Furthermore, the long-term stability could benefit from lower operation voltages to reduce the bias stress. For that purpose, a shift of the transconductance maximum towards lower gate voltages could be achieved by appropriate (contact)doping or different electrode materials. Additionally, more polymers with different side chains or side chain lengths that are even more hydrophilic should be tested to explore the possible limits and find an optimum. The polymer exchange method (*i.e.* the amount of exchanged polymer) should be further quantified and optimized to get more control over the process.

The second part of this thesis contributes to the new field of brain-inspired computing by introducing slow ion diffusion in electrolyte-gated SWNT networks as a possible approach for the development of artificial synapses and neuromorphic devices. For this purpose, thick networks of aerosol-jet printed semiconducting SWNTs were ion-gel-gated using a thick

airbrush-sprayed network of both semiconducting and metallic SWNTs as the gating material. Pulsed operation of these devices in connection to an analog switch resulted in the successful emulation of synaptic functions such as short-term, long-term and spike-timing-dependent plasticity.

Optimizing the applied voltage pulses and their timing resulted in controlled potentiation and depression of the devices, which is promising for neuromorphic computing. The conductance levels changed linearly and symmetrically over a large range, which are two desired properties for neuromorphic devices. Additionally, a good state retention was observed for the highest conductance states.

The largest discrepancies to the biological counterparts were a much larger power consumption of the artificial synapses and a roughly one order of magnitude slower response time. Both issues could be resolved by downscaling of the device dimensions from the millimeter-sized prototypes down to the micrometer range.

In order to be viable for neuromorphic computing applications, the state retention for lower conductance states has to be improved significantly. For this purpose, as found in this work, the prevention of parasitic capacitances, *e.g.* by passivation of the electrode area, is essential. Furthermore, the ion diffusion inside mixed semiconducting and metallic SWNT networks has to be studied in detail, as it plays an integral role for a non-volatile device operation. Deeper insight could be gained from moving-front experiments similarly to the ion diffusion experiments in polymers.[169,269] In this context, different ion-gel compositions with varying content of the ionic liquid and different ionic liquids should be tested.

The possible areas of SWNT applications are still expanding due to extensive studies over the last decades. In that sense, the findings presented here are a contribution towards carbon nanotube based bioelectronis and brain-inspired computing, two emerging technologies, relying on materials beyond silicon, with increasing importance and impact.

Bibliography

[1] Gordon E Moore. Cramming more components onto integrated circuits With unit cost. *Electronics*, 38, 114 (1965).

[2] Gregor Schwartz, Benjamin C.K. Tee, Jianguo Mei, Anthony L. Appleton, Do Hwan Kim, Huiliang Wang, and Zhenan Bao. Flexible polymer transistors with high pressure sensitivity for application in electronic skin and health monitoring. *Nat. Commun.*, 4, 1859 (2013).

[3] Katelyn P. Goetz, Zhong Li, Jeremy W. Ward, Cortney Bougher, Jonathan Rivnay, Jeremy Smith, Brad R. Conrad, Sean R. Parkin, Thomas D. Anthopoulos, Alberto Salleo, John E. Anthony, and Oana D. Jurchescu. Effect of Acene Length on Electronic Properties in 5-, 6-, and 7-Ringed Heteroacenes. *Adv. Mater.*, 23, 3698–3703 (2011).

[4] Pak Heng Lau, Kuniharu Takei, Chuan Wang, Yeonkyeong Ju, Junseok Kim, Zhibin Yu, Toshitake Takahashi, Gyoujin Cho, and Ali Javey. Fully Printed, High Performance Carbon Nanotube Thin-Film Transistors on Flexible Substrates. *Nano Lett.*, 13, 3864–3869 (2013).

[5] Jana Zaumseil. Single-walled carbon nanotube networks for flexible and printed electronics. *Semicond. Sci. Technol.*, 30, 074001 (2015).

[6] Jacques Lefebvre, Jianfu Ding, Zhao Li, Paul Finnie, Gregory Lopinski, and Patrick R. L. Malenfant. High-Purity Semiconducting Single-Walled Carbon Nanotubes: A Key Enabling Material in Emerging Electronics. *Acc. Chem. Res.*, 50, 2479–2486 (2017).

[7] Arko Graf, Yuriy Zakharko, Stefan P. Schießl, Claudia Backes, Moritz Pfohl, Benjamin S. Flavel, and Jana Zaumseil. Large scale, selective dispersion of long single-

walled carbon nanotubes with high photoluminescence quantum yield by shear force mixing. *Carbon N. Y.*, 105, 593–599 (2016).

[8] Marcel Rother, Maximilian Brohmann, Shuyi Yang, Stefan B. Grimm, Stefan P. Schießl, Arko Graf, and Jana Zaumseil. Aerosol-Jet Printing of Polymer-Sorted (6,5) Carbon Nanotubes for Field-Effect Transistors with High Reproducibility. *Adv. Electron. Mater.*, 3, 1700080 (2017).

[9] Stefan P. Schießl, Nils Froehlich, Martin Held, Florentina Gannott, Manuel Schweiger, Michael Forster, Ullrich Scherf, and Jana Zaumseil. Polymer-Sorted Semiconducting Carbon Nanotube Networks for High-Performance Ambipolar Field-Effect Transistors. *ACS Appl. Mater. Interfaces*, 7, 682–689 (2015).

[10] Marcel Rother, Adelaide Kruse, Maximilian Brohmann, Maik Matthiesen, Sebastian Grieger, Thomas M. Higgins, and Jana Zaumseil. Vertical Electrolyte-Gated Transistors Based on Printed Single-Walled Carbon Nanotubes. *ACS Appl. Nano Mater.*, 1, 3616–3624 (2018).

[11] Gage Hills, Christian Lau, Andrew Wright, Samuel Fuller, Mindy D Bishop, Tathagata Srimani, Pritpal Kanhaiya, Rebecca Ho, Aya Amer, Yosi Stein, Denis Murphy, Arvind, Anantha Chandrakasan, and Max M. Shulaker. Modern microprocessor built from complementary carbon nanotube transistors. *Nature*, 572, 595–602 (2019).

[12] Brendan Mirka, Nicole A Rice, Phillip Williams, Mathieu N Tousignant, Nicholas T Boileau, William J Bodnaryk, Darryl Fong, Alex Adronov, and Benoît H. Lessard. Excess Polymer in Single-Walled Carbon Nanotube Thin-Film Transistors: Its Removal Prior to Fabrication Is Unnecessary. *ACS Nano*, 15, 8252–8266 (2021).

[13] Alireza Molazemhosseini, Fabrizio Antonio Viola, Felix J. Berger, Nicolas F. Zorn, Jana Zaumseil, and Mario Caironi. A Rapidly Stabilizing Water-Gated Field-Effect Transistor Based on Printed Single-Walled Carbon Nanotubes for Biosensing Applications. *ACS Appl. Electron. Mater.*, 3, 3106–3113 (2021).

[14] Marcin S. Filipiak, Marcel Rother, Nesha M. Andoy, Arne C. Knudsen, Stefan Grimm, Christopher Bachran, Lee Kim Swee, Jana Zaumseil, and Alexey Tarasov. Highly sen-

sitive, selective and label-free protein detection in physiological solutions using carbon nanotube transistors with nanobody receptors. *Sensors Actuators B Chem.*, 255, 1507–1516 (2018).

[15] Bajramshahe Shkodra, Mattia Petrelli, Martina Aurora Costa Angeli, Denis Garoli, Nako Nakatsuka, Paolo Lugli, and Luisa Petti. Electrolyte-gated carbon nanotube field-effect transistor-based biosensors: Principles and applications. *Appl. Phys. Rev.*, 8, 041325 (2021).

[16] Xenofon Strakosas, Manuelle Bongo, and Róisín M. Owens. The organic electrochemical transistor for biological applications. *J. Appl. Polym. Sci.*, 132, 41735–41735 (2015).

[17] Felix J. Berger, Thomas M. Higgins, Marcel Rother, Arko Graf, Yuriy Zakharko, Sybille Allard, Maik Matthiesen, Jan M. Gotthardt, Ullrich Scherf, and Jana Zaumseil. From Broadband to Electrochromic Notch Filters with Printed Monochiral Carbon Nanotubes. *ACS Appl. Mater. Interfaces*, 10, 11135–11142 (2018).

[18] Yoeri Van De Burgt, Ewout Lubberman, Elliot J. Fuller, Scott T. Keene, Grégorio C. Faria, Sapan Agarwal, Matthew J. Marinella, A. Alec Talin, and Alberto Salleo. A non-volatile organic electrochemical device as a low-voltage artificial synapse for neuromorphic computing. *Nat. Mater.*, 16, 414–418 (2017).

[19] Yoeri Van De Burgt, Armantas Melianas, Scott Tom Keene, George Malliaras, and Alberto Salleo. Organic electronics for neuromorphic computing. *Nat. Electron.*, 1, 386–397 (2018).

[20] Qingzhou Wan, Mohammad T. Sharbati, John R. Erickson, Yanhao Du, and Feng Xiong. Emerging Artificial Synaptic Devices for Neuromorphic Computing. *Adv. Mater. Technol.*, 4, 1–34 (2019).

[21] Hea Lim Park, Yeongjun Lee, Naryung Kim, Dae Gyo Seo, Gyeong Tak Go, and Tae Woo Lee. Flexible Neuromorphic Electronics for Computing, Soft Robotics, and Neuroprosthetics. *Adv. Mater.*, 32, 1903558 (2020).

[22] Andreas Hirsch. The era of carbon allotropes. *Nat. Mater.*, 9, 868–871 (2010).

[23] H. W. Kroto, J. R. Heath, S. C. O'Brien, R. F. Curl, and R. E. Smalley. C60: Buckminsterfullerene. *Nature*, 318, 162–163 (1985).

[24] S. Iijima. Helical microtubules of graphitic carbon. *Nature*, 354, 56–58 (1991).

[25] K. S. Novoselov, A. K. Geim, S. V. Morozov, D. Jiang, Y. Zhang, S. V. Dubonos, I. V. Grigorieva, and A. A. Firsov. Electric Field Effect in Atomically Thin Carbon Films. *Science*, 306, 666–669 (2004).

[26] Ray H. Baughman, Anvar A. Zakhidov, and Wait A. De Heer. Carbon nanotubes - The route toward applications. *Science*, 297, 787–792 (2002).

[27] M. S. Dresselhaus, G. Dresselhaus, A. Jorio, A. G. Souza Filho, M. A. Pimenta, and R. Saito. Single nanotube Raman spectroscopy. *Acc. Chem. Res.*, 35, 1070–1078 (2002).

[28] R. Saito, M. Fujita, G. Dresselhaus, and M. S. Dresselhaus. Electronic structure of chiral graphene tubules. *Appl. Phys. Lett.*, 60, 2204–2206 (1992).

[29] Xueshen Wang, Qunqing Li, Jing Xie, Zhong Jin, Jinyong Wang, Yan Li, Kaili Jiang, and Shoushan Fan. Fabrication of ultralong and electrically uniform single-walled carbon nanotubes on clean substrates. *Nano Lett.*, 9, 3137–3141 (2009).

[30] S. Reich, J. Maultzsch, C. Thomsen, and P. Ordejón. Tight-binding description of graphene. *Phys. Rev. B - Condens. Matter Mater. Phys.*, 66, 354121–354125 (2002).

[31] Jean Christophe Charlier, Xavier Blase, and Stephan Roche. Electronic and transport properties of nanotubes. *Rev. Mod. Phys.*, 79, 677–732 (2007).

[32] S Maruyama. 1D DOS (van Hove Singularity). http://www.photon.t.u-tokyo.ac.jp/~maruyama/kataura/1D_DOS.html (accessed 28 June, 2022).

[33] Jeroen W. G. Wilder, Liesbeth C. Venema, Andrew G. Rinzler, Richard E. Smalley, and Cees Dekker. Electronic structure of atomically resolved carbon nanotubes. *Nature*, 391, 59–62 (1998).

[34] Lorin X. Benedict, Steven G. Louie, and Marvin L. Cohen. Static polarizabilities of single-wall carbon nanotubes. *Phys. Rev. B*, 52, 8541–8549 (1995).

[35] Hiroki Ago, Naoyasu Uehara, Ken ichi Ikeda, Ryota Ohdo, Kazuhiro Nakamura, and Masaharu Tsuji. Synthesis of horizontally-aligned single-walled carbon nanotubes with controllable density on sapphire surface and polarized Raman spectroscopy. *Chem. Phys. Lett.*, 421, 399–403 (2006).

[36] Mai Takase, Hiroshi Ajiki, Yoshihiko Mizumoto, Keiichiro Komeda, Masanobu Nara, Hideki Nabika, Satoshi Yasuda, Hajime Ishihara, and Kei Murakoshi. Selection-rule breakdown in plasmon-induced electronic excitation of an isolated single-walled carbon nanotube. *Nat. Photonics*, 7, 550–554 (2013).

[37] H. Kataura, Y. Kumazawa, Y. Maniwa, I. Umezu, S. Suzuki, Y. Ohtsuka, and Y. Achiba. Optical properties of single-wall carbon nanotubes. *Synth. Met.*, 103, 2555–2558 (1999).

[38] Sergei M. Bachilo, Michael S. Strano, Carter Kittrell, Robert H. Hauge, Richard E. Smalley, and R. Bruce Weisman. Structure-Assigned Optical Spectra of Single-Walled Carbon Nanotubes. *Science*, 298, 2361–2366 (2002).

[39] A. Jorio, A. G. Souza Filho, G. Dresselhaus, M. S. Dresselhaus, R. Saito, J. H. Hafner, C. M. Lieber, F. M. Matinaga, M. S. S. Dantas, and M. A. Pimenta. Joint density of electronic states for one isolated single-wall carbon nanotube studied by resonant Raman scattering. *Phys. Rev. B*, 63, 245416 (2001).

[40] A. Jorio, R. Saito, J. H. Hafner, C. M. Lieber, M. Hunter, T. McClure, G. Dresselhaus, and M. S. Dresselhaus. Structural (n,m) Determination of Isolated Single-Wall Carbon Nanotubes by Resonant Raman Scattering. *Phys. Rev. Lett.*, 86, 1118–1121 (2001).

[41] Finn L. Sebastian, Nicolas F. Zorn, Simon Settele, Sebastian Lindenthal, Felix J. Berger, Christoph Bendel, Han Li, Benjamin S. Flavel, and Jana Zaumseil. Absolute Quantification of sp3Defects in Semiconducting Single-Wall Carbon Nanotubes by Raman Spectroscopy. *J. Phys. Chem. Lett.*, pages 3542–3548 (2022).

[42] Stefan B. Grimm, Florian Jakubka, Stefan P. Schießl, Florentina Gannott, and Jana Zaumseil. Mapping Charge-Carrier Density Across the p-n Junction in Ambipolar Carbon-Nanotube Networks by Raman Microscopy. *Adv. Mater.*, 26, 7986–7992 (2014).

[43] Fabienne Dragin, Alain Pénicaud, Matteo Iurlo, Massimo Marcaccio, Francesco Paolucci, Eric Anglaret, and Richard Martel. Raman doping profiles of polyelectrolyte SWNTs in solution. *ACS Nano*, 5, 9892–9897 (2011).

[44] Martin Kalbac and Ladislav Kavan. The influence of doping on the Raman intensity of the D band in single walled carbon nanotubes. *Carbon N. Y.*, 48, 832–838 (2010).

[45] Arko Graf, Martin Held, Yuriy Zakharko, Laura Tropf, Malte C. Gather, and Jana Zaumseil. Electrical pumping and tuning of exciton-polaritons in carbon nanotube microcavities. *Nat. Mater.*, 16, 911–917 (2017).

[46] Jana Zaumseil. Recent Developments and Novel Applications of Thin Film, Light-Emitting Transistors. *Adv. Funct. Mater.*, 30, 1905269 (2020).

[47] Severin Schneider, Maximilian Brohmann, Roxana Lorenz, Yvonne J. Hofstetter, Marcel Rother, Eric Sauter, Michael Zharnikov, Yana Vaynzof, Hans-Jörg Himmel, and Jana Zaumseil. Efficient n-Doping and Hole Blocking in Single-Walled Carbon Nanotube Transistors with 1,2,4,5-Tetrakis(tetramethylguanidino)ben-zene. *ACS Nano*, 12, 5895–5902 (2018).

[48] Carla M. Aguirre, Pierre L. Levesque, Matthieu Paillet, François Lapointe, Benoit C. St-Antoine, Patrick Desjardins, and Richard Martel. The Role of the Oxygen/Water Redox Couple in Suppressing Electron Conduction in Field-Effect Transistors. *Adv. Mater.*, 21, 3087–3091 (2009).

[49] Qingkai Qian, Guanhong Li, Yuanhao Jin, Junku Liu, Yuan Zou, Kaili Jiang, Shoushan Fan, and Qunqing Li. Trap-State-Dominated Suppression of Electron Conduction in Carbon Nanotube Thin-Film Transistors. *ACS Nano*, 8, 9597–9605 (2014).

[50] Vasili Perebeinos, J. Tersoff, and Phaedon Avouris. Electron-phonon interaction and transport in semiconducting carbon nanotubes. *Phys. Rev. Lett.*, 94, 2–5 (2005).

[51] Xinjian Zhou, Ji Yong Park, Shaoming Huang, Jie Liu, and Paul L. McEuen. Band structure, phonon scattering, and the performance limit of single-walled carbon nanotube transistors. *Phys. Rev. Lett.*, 95, 1–4 (2005).

[52] G. Pennington and N. Goldsman. Semiclassical transport and phonon scattering of electrons in semiconducting carbon nanotubes. *Phys. Rev. B*, 68, 045426 (2003).

[53] S. Ilani, L. A.K. Donev, M. Kindermann, and P. L. McEuen. Measurement of the quantum capacitance of interacting electrons in carbon nanotubes. *Nat. Phys.*, 2, 687–691 (2006).

[54] Chris Rutherglen and Peter Burke. Nanoelectromagnetics: Circuit and Electromagnetic Properties of Carbon Nanotubes. *Small*, 5, 884–906 (2009).

[55] Jinfeng Li, Phi H. Q. Pham, Weiwei Zhou, Ted D. Pham, and Peter J. Burke. Carbon-Nanotube–Electrolyte Interface: Quantum and Electric Double Layer Capacitance. *ACS Nano*, 12, 9763–9774 (2018).

[56] Han Li, Georgy Gordeev, Oisin Garrity, Stephanie Reich, and Benjamin S Flavel. Separation of Small-Diameter Single-Walled Carbon Nanotubes in One to Three Steps with Aqueous Two-Phase Extraction. *ACS Nano*, 13, 2567–2578 (2019).

[57] Stefan P. Schießl, Florentina Gannott, Sebastian H. Etschel, Manuel Schweiger, Saeideh Grünler, Marcus Halik, and Jana Zaumseil. Self-Assembled Monolayer Dielectrics for Low-Voltage Carbon Nanotube Transistors with Controlled Network Density. *Adv. Mater. Interfaces*, 3, 1600215 (2016).

[58] Stefan P. Schießl, Marcel Rother, Jan Lüttgens, and Jana Zaumseil. Extracting the field-effect mobilities of random semiconducting single-walled carbon nanotube networks: A critical comparison of methods. *Appl. Phys. Lett.*, 111, 193301 (2017).

[59] H.-S. Philip Wong and Deji Akinwande. *Carbon Nanotube and Graphene Device Physics*. Cambridge University Press (2011). ISBN 978-0-521-51905-2.

[60] S. Kumar, G. B. Blanchet, M. S. Hybertsen, J. Y. Murthy, and M. A. Alam. Performance of carbon nanotube-dispersed thin-film transistors. *Appl. Phys. Lett.*, 89 (2006).

[61] E. S. Snow, P. M. Campbell, M. G. Ancona, and J. P. Novak. High-mobility carbon-nanotube thin-film transistors on a polymeric substrate. *Appl. Phys. Lett.*, 86, 1–3 (2005).

[62] Nima Rouhi, Dheeraj Jain, and Peter John Burke. High-performance semiconducting nanotube inks: Progress and prospects. *ACS Nano*, 5, 8471–8487 (2011).

[63] William A. Gaviria Rojas and Mark C. Hersam. Chirality-Enriched Carbon Nanotubes for Next-Generation Computing. *Adv. Mater.*, 32, 1905654 (2020).

[64] Maximilian Brohmann, Marcel Rother, Stefan P. Schießl, Eduard Preis, Sybille Allard, Ullrich Scherf, and Jana Zaumseil. Temperature-Dependent Charge Transport in Polymer-Sorted Semiconducting Carbon Nanotube Networks with Different Diameter Distributions. *J. Phys. Chem. C*, 122, 19886–19896 (2018).

[65] Maximilian Brohmann, Felix J. Berger, Maik Matthiesen, Stefan P. Schießl, Severin Schneider, and Jana Zaumseil. Charge Transport in Mixed Semiconducting Carbon Nanotube Networks with Tailored Mixing Ratios. *ACS Nano*, 13, 7323–7332 (2019).

[66] M. Stadermann, S. J. Papadakis, M. R. Falvo, J. Novak, E. Snow, Q. Fu, J. Liu, Y. Fridman, J. J. Boland, R. Superfine, and S. Washburn. Nanoscale study of conduction through carbon nanotube networks. *Phys. Rev. B - Condens. Matter Mater. Phys.*, 69, 10–12 (2004).

[67] Peter N. Nirmalraj, Philip E. Lyons, Sukanta De, Jonathan N. Coleman, and John J. Boland. Electrical connectivity in single-walled carbon nanotube networks. *Nano Lett.*, 9, 3890–3895 (2009).

[68] Jana Zaumseil. Semiconducting Single-Walled Carbon Nanotubes or Very Rigid Conjugated Polymers: A Comparison. *Adv. Electron. Mater.*, 5, 1–28 (2019).

[69] Cedric Rolin, Enpu Kang, Jeong-Hwan Lee, Gustaaf Borghs, Paul Heremans, and Jan Genoe. Charge carrier mobility in thin films of organic semiconductors by the gated van der Pauw method. *Nat. Commun.*, 8, 14975 (2017).

[70] Soumendra N. Barman, Melburne C. Lemieux, Jaeyeon Baek, Rut Rivera, and Zhenan Bao. Effects of dispersion conditions of single-walled carbon nanotubes on the electrical characteristics of thin film network transistors. *ACS Appl. Mater. Interfaces*, 2, 2672–2678 (2010).

[71] Brenna Norton-Baker, Rachelle Ihly, Isaac E. Gould, Azure D. Avery, Zbyslaw R. Owczarczyk, Andrew J. Ferguson, and Jeffrey L. Blackburn. Polymer-Free Carbon Nanotube Thermoelectrics with Improved Charge Carrier Transport and Power Factor. *ACS Energy Lett.*, 1, 1212–1220 (2016).

[72] Shrividya Ravi, Alan B. Kaiser, and Christopher W. Bumby. Charge transport in surfactant-free single walled carbon nanotube networks. *Phys. Status Solidi Basic Res.*, 250, 1463–1467 (2013).

[73] Mikhail E. Itkis, Aron Pekker, Xiaojuan Tian, Elena Bekyarova, and Robert C. Haddon. Networks of Semiconducting SWNTs: Contribution of Midgap Electronic States to the Electrical Transport. *Acc. Chem. Res.*, 48, 2270–2279 (2015).

[74] N. F. Mott. Conduction in non-crystalline materials. *Philos. Mag.*, 19, 835–852 (1969).

[75] Ping Sheng. Fluctuation-induced tunneling conduction in disordered materials. *Phys. Rev. B*, 21, 2180–2195 (1980).

[76] Nicolas F. Zorn, Felix J. Berger, and Jana Zaumseil. Charge Transport in and Electroluminescence from sp 3 -Functionalized Carbon Nanotube Networks. *ACS Nano*, 15, 10451–10463 (2021).

[77] Stefan P. Schießl, Xander de Vries, Marcel Rother, Andrea Massé, Maximilian Brohmann, Peter A. Bobbert, and Jana Zaumseil. Modeling carrier density dependent charge transport in semiconducting carbon nanotube networks. *Phys. Rev. Mater.*, 1, 046003 (2017).

[78] Andrea Massé, Pascal Friederich, Franz Symalla, Feilong Liu, Robert Nitsche, Reinder Coehoorn, Wolfgang Wenzel, and Peter A. Bobbert. Ab initio charge-carrier mobility model for amorphous molecular semiconductors. *Phys. Rev. B*, 93, 195209 (2016).

[79] Y. Y. Yimer, P. A. Bobbert, and R. Coehoorn. Charge transport in disordered organic host-guest systems: Effects of carrier density and electric field. *J. Phys. Condens. Matter*, 20 (2008).

[80] Katherine R. Jinkins, Sean M. Foradori, Vivek Saraswat, Robert M. Jacobberger, Jonathan H. Dwyer, Padma Gopalan, Arganthaël Berson, and Michael S. Arnold. Aligned 2D carbon nanotube liquid crystals for wafer-scale electronics. *Sci. Adv.*, 7, 1–12 (2021).

[81] C. Journet, W. K. Maser, P. Bernier, A. Loiseau, M. Lamy de la Chapelle, S. Lefrant, P. Deniard, R. Lee, and J. E. Fischer. Large-scale production of single-walled carbon nanotubes by the electric-arc technique. *Nature*, 388, 756–758 (1997).

[82] T. Guo, P. Nikolaev, A. Thess, D.T. Colbert, and R.E. Smalley. Catalytic growth of single-walled manotubes by laser vaporization. *Chem. Phys. Lett.*, 243, 49–54 (1995).

[83] Yoshinori Ando, Xinluo Zhao, Kaori Hirahara, Kazutomo Suenaga, Shunji Bandow, and Sumio Iijima. Mass production of single-wall carbon nanotubes by the arc plasma jet method. *Chem. Phys. Lett.*, 323, 580–585 (2000).

[84] Frank Hennrich, Ralph Krupke, Katharina Arnold, Jan A. Rojas Stuetz, Sergei Lebedkin, Thomas Koch, Thomas Schimmel, and Manfred M Kappes. The Mechanism of Cavitation-Induced Scission of Single-Walled Carbon Nanotubes. *J. Phys. Chem. B*, 111, 1932–1937 (2007).

[85] Michael J. O'Connell, Sergei M. Bachilo, Chad B. Huffman, Valerie C. Moore, Michael S. Strano, Erik H. Haroz, Kristy L. Rialon, Peter J. Boul, William H. Noon, Carter Kittrell, Jianpeng Ma, Robert H. Hauge, R. Bruce Weisman, and Richard E. Smalley. Band Gap Fluorescence from Individual Single-Walled Carbon Nanotubes. *Science*, 297, 593–596 (2002).

[86] Timothy J. McDonald, Chaiwat Engtrakul, Marcus Jones, Garry Rumbles, and Michael J. Heben. Kinetics of PL Quenching during Single-Walled Carbon Nanotube Rebundling and Diameter-Dependent Surfactant Interactions. *J. Phys. Chem. B*, 110, 25339–25346 (2006).

[87] Huaping Liu, Daisuke Nishide, Takeshi Tanaka, and Hiromichi Kataura. Large-scale single-chirality separation of single-wall carbon nanotubes by simple gel chromatography. *Nat. Commun.*, 2, 309 (2011).

[88] Jeffrey A. Fagan, Constantine Y. Khripin, Carlos A. Silvera Batista, Jeffrey R. Simpson, Erik H. Hároz, Angela R. Hight Walker, and Ming Zheng. Isolation of Specific Small-Diameter Single-Wall Carbon Nanotube Species via Aqueous Two-Phase Extraction. *Adv. Mater.*, 26, 2800–2804 (2014).

[89] Qian Li and Jing Liu. Retracted: Combined Printing of Highly Aligned Single-Walled Carbon Nanotube Thin Films with Liquid Metal for Direct Fabrication of Functional Electronic Devices. *Adv. Electron. Mater.*, 6, 2000537 (2020).

[90] Ralph Krupke, Frank Hennrich, Hilbert v. Loehneysen, and Manfred M. Kappes. Separation of Metallic from Semiconducting Single-Walled Carbon Nanotubes. *Science*, 301, 344–347 (2003).

[91] Adrian Nish, Jeong-yuan Hwang, James Doig, and Robin J Nicholas. Highly selective dispersion of single-walled carbon nanotubes using aromatic polymers. *Nat. Nanotechnol.*, 2, 640–646 (2007).

[92] Florian Jakubka, Stefan P Schießl, Sebastian Martin, Jan M Englert, Frank Hauke, Andreas Hirsch, and Jana Zaumseil. Effect of Polymer Molecular Weight and Solution Parameters on Selective Dispersion of Single-Walled Carbon Nanotubes. *ACS Macro Lett.*, 1, 815–819 (2012).

[93] Widianta Gomulya, Guadalupe Diaz Costanzo, Elton J Figueiredo de Carvalho, Satria Zulkarnaen Bisri, Vladimir Derenskyi, Martin Fritsch, Nils Fröhlich, Sybille Allard, Pavlo Gordiichuk, Andreas Herrmann, Siewert Jan Marrink, Maria Cristina dos Santos, Ulrich Scherf, and Maria Antonietta Loi. Semiconducting Single-Walled Carbon Nanotubes on Demand by Polymer Wrapping. *Adv. Mater.*, 25, 2948–2956 (2013).

[94] Masayoshi Tange, Toshiya Okazaki, and Sumio Iijima. Selective Extraction of Semiconducting Single-Wall Carbon Nanotubes by Poly(9,9-dioctylfluorene- alt -pyridine) for 1.5 μm Emission. *ACS Appl. Mater. Interfaces*, 4, 6458–6462 (2012).

[95] Hang Woo Lee, Yeohoon Yoon, Steve Park, Joon Hak Oh, Sanghyun Hong, Luckshitha S Liyanage, Huiliang Wang, Satoshi Morishita, Nishant Patil, Young Jun Park, Jong Jin Park, Andrew Spakowitz, Giulia Galli, Francois Gygi, Philip H.-S.

Wong, Jeffrey B.-H. Tok, Jong Min Kim, and Zhenan Bao. Selective dispersion of high purity semiconducting single-walled carbon nanotubes with regioregular poly(3-alkylthiophene)s. *Nat. Commun.*, 2, 541 (2011).

[96] Huiliang Wang, Ghada I Koleilat, Peng Liu, Gonzalo Jiménez-Osés, Ying-Chih Lai, Michael Vosgueritchian, Ya Fang, Steve Park, Kendall N Houk, and Zhenan Bao. High-Yield Sorting of Small-Diameter Carbon Nanotubes for Solar Cells and Transistors. *ACS Nano*, 8, 2609–2617 (2014).

[97] Fabien A Lemasson, Timo Strunk, Peter Gerstel, Frank Hennrich, Sergei Lebedkin, Christopher Barner-Kowollik, Wolfgang Wenzel, Manfred M Kappes, and Marcel Mayor. Selective Dispersion of Single-Walled Carbon Nanotubes with Specific Chiral Indices by Poly(N -decyl-2,7-carbazole). *J. Am. Chem. Soc.*, 133, 652–655 (2011).

[98] Fabien Lemasson, Nicolas Berton, Jana Tittmann, Frank Hennrich, Manfred M. Kappes, and Marcel Mayor. Polymer Library Comprising Fluorene and Carbazole Homo- and Copolymers for Selective Single-Walled Carbon Nanotubes Extraction. *Macromolecules*, 45, 713–722 (2012).

[99] Jeong-Yuan Hwang, Adrian Nish, James Doig, Sigrid Douven, Chun-Wei Chen, Li-Chyong Chen, and Robin J Nicholas. Polymer Structure and Solvent Effects on the Selective Dispersion of Single-Walled Carbon Nanotubes. *J. Am. Chem. Soc.*, 130, 3543–3553 (2008).

[100] Widianta Gomulya, Jorge Mario Salazar Rios, Vladimir Derenskyi, Satria Zulkarnaen Bisri, Stefan Jung, Martin Fritsch, Sybille Allard, Ullrich Scherf, Maria Cristina dos Santos, and Maria Antonietta Loi. Effect of temperature on the selection of semiconducting single walled carbon nanotubes using Poly(3-dodecylthiophene-2,5-diyl). *Carbon N. Y.*, 84, 66–73 (2015).

[101] Vladimir Derenskyi, Widianta Gomulya, Jia Gao, Satria Zulkarnaen Bisri, Mariacecilia Pasini, Yueh-Lin Loo, and Maria Antonietta Loi. Semiconducting SWNTs sorted by polymer wrapping: How pure are they? *Appl. Phys. Lett.*, 112, 072106 (2018).

[102] Yongho Joo, Gerald J Brady, Catherine Kanimozhi, Jaehyoung Ko, Matthew J Shea, Michael T Strand, Michael S Arnold, and Padma Gopalan. Polymer-Free Electronic-Grade Aligned Semiconducting Carbon Nanotube Array. *ACS Appl. Mater. Interfaces*, 9, 28859–28867 (2017).

[103] Rama Dubey, Dhiraj Dutta, Arpan Sarkar, and Pronobesh Chattopadhyay. Functionalized carbon nanotubes: synthesis, properties and applications in water purification, drug delivery, and material and biomedical sciences. *Nanoscale Adv.*, 3, 5722–5744 (2021).

[104] Zahra Abousalman-Rezvani, Parvaneh Eskandari, Hossein Roghani-Mamaqani, and Mehdi Salami-Kalajahi. Functionalization of carbon nanotubes by combination of controlled radical polymerization and "grafting to" method. *Adv. Colloid Interface Sci.*, 278, 102126 (2020).

[105] Jana Zaumseil. Luminescent Defects in Single-Walled Carbon Nanotubes for Applications. *Adv. Opt. Mater.*, 10, 2101576 (2022).

[106] Anil Suri, Amit K. Chakraborty, and Karl S. Coleman. A Facile, Solvent-Free, Noncovalent, and Nondisruptive Route To Functionalize Single-Wall Carbon Nanotubes Using Tertiary Phosphines. *Chem. Mater.*, 20, 1705–1709 (2008).

[107] Jules Zeuna Nguendia, Weiheng Zhong, Alexandre Fleury, Guillaume De Grandpré, Armand Soldera, Ribal Georges Sabat, and Jerome P. Claverie. Supramolecular Complexes of Multivalent Cholesterol-Containing Polymers to Solubilize Carbon Nanotubes in Apolar Organic Solvents. *Chem. - An Asian J.*, 9, 1356–1364 (2014).

[108] Jianying Ouyang, Jianfu Ding, Jacques Lefebvre, Zhao Li, Chang Guo, Arnold J. Kell, and Patrick R.L. Malenfant. Sorting of Semiconducting Single-Walled Carbon Nanotubes in Polar Solvents with an Amphiphilic Conjugated Polymer Provides General Guidelines for Enrichment. *ACS Nano*, 12, 1910–1919 (2018).

[109] Junfeng Sun, Ashish Sapkota, Hyejin Park, Prince Wesley, Younsu Jung, Bijendra Bishow Maskey, Yushin Kim, Yutaka Majima, Jianfu Ding, Jianying Ouyang, Chang Guo, Jacques Lefebvre, Zhao Li, Patrick R.L. Malenfant, Ali Javey, and Gyoujin

Cho. Fully R2R-Printed Carbon-Nanotube-Based Limitless Length of Flexible Active-Matrix for Electrophoretic Display Application. *Adv. Electron. Mater.*, 6, 1901431 (2020).

[110] Felix J. Berger, Jan Lüttgens, Tim Nowack, Tobias Kutsch, Sebastian Lindenthal, Lucas Kistner, Christine C. Müller, Lukas M. Bongartz, Victoria A. Lumsargis, Yuriy Zakharko, and Jana Zaumseil. Brightening of Long, Polymer-Wrapped Carbon Nanotubes by sp 3 Functionalization in Organic Solvents. *ACS Nano*, 13, 9259–9269 (2019).

[111] Simon Settele, Felix J. Berger, Sebastian Lindenthal, Shen Zhao, Abdurrahman Ali El Yumin, Nicolas F. Zorn, Andika Asyuda, Michael Zharnikov, Alexander Högele, and Jana Zaumseil. Synthetic control over the binding configuration of luminescent sp3-defects in single-walled carbon nanotubes. *Nat. Commun.*, 12, 2119 (2021).

[112] Samuel D. Stranks, Anton M. R. Baker, Jack A. Alexander-Webber, Beate Dirks, and Robin J. Nicholas. Production of High-Purity Single-Chirality Carbon Nanotube Hybrids by Selective Polymer Exchange. *Small*, 9, 2245–2249 (2013).

[113] Merve Balcı Leinen, Felix J. Berger, Patrick Klein, Markus Mühlinghaus, Nicolas F. Zorn, Simon Settele, Sybille Allard, Ullrich Scherf, and Jana Zaumseil. Doping-Dependent Energy Transfer from Conjugated Polyelectrolytes to (6,5) Single-Walled Carbon Nanotubes. *J. Phys. Chem. C*, 123, 22680–22689 (2019).

[114] Merve Balcı Leinen, Patrick Klein, Finn L. Sebastian, Nicolas F. Zorn, Sylwia Adamczyk, Sybille Allard, Ullrich Scherf, and Jana Zaumseil. Spiropyran-Functionalized Polymer–Carbon Nanotube Hybrids for Dynamic Optical Memory Devices and UV Sensors. *Adv. Electron. Mater.*, 6, 2000717 (2020).

[115] Yiding Gu, Ting Zhang, Hao Chen, Feng Wang, Yueming Pu, Chunming Gao, and Shibin Li. Mini Review on Flexible and Wearable Electronics for Monitoring Human Health Information. *Nanoscale Res. Lett.*, 14, 263 (2019).

[116] Alina S. Sharova, Filippo Melloni, Guglielmo Lanzani, Christopher J. Bettinger, and

Mario Caironi. Edible Electronics: The Vision and the Challenge. *Adv. Mater. Technol.*, 6, 2000757 (2021).

[117] Hagen Klauk. Organic thin-film transistors. *Chem. Soc. Rev.*, 39, 2643 (2010).

[118] Lay-Lay Chua, Peter K. H. Ho, Henning Sirringhaus, and Richard H. Friend. High-stability ultrathin spin-on benzocyclobutene gate dielectric for polymer field-effect transistors. *Appl. Phys. Lett.*, 84, 3400–3402 (2004).

[119] R. L. Hoffman. ZnO-channel thin-film transistors: Channel mobility. *J. Appl. Phys.*, 95, 5813–5819 (2004).

[120] Matthew Waldrip, Oana D Jurchescu, David J Gundlach, and Emily G Bittle. Contact Resistance in Organic Field-Effect Transistors: Conquering the Barrier. *Adv. Funct. Mater.*, 30, 1904576 (2019).

[121] Jana Zaumseil and Henning Sirringhaus. Electron and Ambipolar Transport in Organic Field-Effect Transistors. *Chem. Rev.*, 107, 1296–1323 (2007).

[122] J. Zaumseil, C. L. Donley, J.-S. Kim, R. H. Friend, and H. Sirringhaus. Efficient Top-Gate, Ambipolar, Light-Emitting Field-Effect Transistors Based on a Green-Light-Emitting Polyfluorene. *Adv. Mater.*, 18, 2708–2712 (2006).

[123] Constance Rost, Siegfried Karg, Walter Riess, Maria Antonietta Loi, Mauro Murgia, and Michele Muccini. Ambipolar light-emitting organic field-effect transistor. *Appl. Phys. Lett.*, 85, 1613–1615 (2004).

[124] Florian Jakubka, Stefan B. Grimm, Yuriy Zakharko, Florentina Gannott, and Jana Zaumseil. Trion Electroluminescence from Semiconducting Carbon Nanotubes. *ACS Nano*, 8, 8477–8486 (2014).

[125] Phaedon Avouris, Marcus Freitag, and Vasili Perebeinos. Carbon-nanotube photonics and optoelectronics. *Nat. Photonics*, 2, 341–350 (2008).

[126] Michael L. Geier, Pradyumna L. Prabhumirashi, Julian J. McMorrow, Weichao Xu, Jung-Woo T Seo, Ken Everaerts, Chris H. Kim, Tobin J. Marks, and Mark C. Her-

sam. Subnanowatt carbon nanotube complementary logic enabled by threshold voltage control. *Nano Lett.*, 13, 4810–4 (2013).

[127] Christian Lau, Tathagata Srimani, Mindy D. Bishop, Gage Hills, and Max M. Shulaker. Tunable n -Type Doping of Carbon Nanotubes through Engineered Atomic Layer Deposition HfO X Films. *ACS Nano*, 12, 10924–10931 (2018).

[128] R. Martel, V. Derycke, C. Lavoie, J. Appenzeller, K. K. Chan, J. Tersoff, and Ph Avouris. Ambipolar Electrical Transport in Semiconducting Single-Wall Carbon Nanotubes. *Phys. Rev. Lett.*, 87, 256805 (2001).

[129] J. Lefebvre, J. Ding, Z. Li, F. Cheng, N. Du, and P. R. L. Malenfant. Hysteresis free carbon nanotube thin film transistors comprising hydrophobic dielectrics. *Appl. Phys. Lett.*, 107, 243301 (2015).

[130] R. Martel, T. Schmidt, H. R. Shea, T. Hertel, and Ph. Avouris. Single- and multi-wall carbon nanotube field-effect transistors. *Appl. Phys. Lett.*, 73, 2447–2449 (1998).

[131] Chenyi Zhao, Donglai Zhong, Jie Han, Lijun Liu, Zhiyong Zhang, and Lian-Mao Peng. Exploring the Performance Limit of Carbon Nanotube Network Film Field-Effect Transistors for Digital Integrated Circuit Applications. *Adv. Funct. Mater.*, 29, 1808574 (2019).

[132] Jianshi Tang, Qing Cao, George Tulevski, Keith A. Jenkins, Luca Nela, Damon B. Farmer, and Shu-Jen Han. Flexible CMOS integrated circuits based on carbon nanotubes with sub-10 ns stage delays. *Nat. Electron.*, 1, 191–196 (2018).

[133] Sungho Kim, Jinsu Yoon, Hee-Dong Kim, and Sung-Jin Choi. Carbon Nanotube Synaptic Transistor Network for Pattern Recognition. *ACS Appl. Mater. Interfaces*, 7, 25479–25486 (2015).

[134] Sungho Kim, Yongwoo Lee, Hee Dong Kim, and Sung Jin Choi. Parallel weight update protocol for a carbon nanotube synaptic transistor array for accelerating neuromorphic computing. *Nanoscale*, 12, 2040–2046 (2020).

[135] Chenguang Qiu, Zhiyong Zhang, Mengmeng Xiao, Yingjun Yang, Donglai Zhong, and Lian-Mao Peng. Scaling carbon nanotube complementary transistors to 5-nm gate lengths. *Science*, 355, 271–276 (2017).

[136] Aaron D. Franklin, Shu-Jen Han, George S. Tulevski, Mathieu Luisier, Chris M. Breslin, Lynne Gignac, Mark S. Lundstrom, and Wilfried Haensch. Sub-10 nm carbon nanotube transistor. In *2011 Int. Electron Devices Meet.*, pages 23.7.1–23.7.3. IEEE (2011).

[137] Qing Cao, Shu-Jen Han, Jerry Tersoff, Aaron D. Franklin, Yu Zhu, Zhen Zhang, George S. Tulevski, Jianshi Tang, and Wilfried Haensch. End-bonded contacts for carbon nanotube transistors with low, size-independent resistance. *Science*, 350, 68–72 (2015).

[138] Yuegang Zhang, Aileen Chang, Jien Cao, Qian Wang, Woong Kim, Yiming Li, Nathan Morris, Erhan Yenilmez, Jing Kong, and Hongjie Dai. Electric-field-directed growth of aligned single-walled carbon nanotubes. *Appl. Phys. Lett.*, 79, 3155–3157 (2001).

[139] Seong Jun Kang, Coskun Kocabas, Taner Ozel, Moonsub Shim, Ninad Pimparkar, Muhammad A. Alam, Slava V. Rotkin, and John A. Rogers. High-performance electronics using dense, perfectly aligned arrays of single-walled carbon nanotubes. *Nat. Nanotechnol.*, 2, 230–236 (2007).

[140] Bilu Liu, Jia Liu, Hai-Bei Li, Radha Bhola, Edward A. Jackson, Lawrence T. Scott, Alister Page, Stephan Irle, Keiji Morokuma, and Chongwu Zhou. Nearly Exclusive Growth of Small Diameter Semiconducting Single-Wall Carbon Nanotubes from Organic Chemistry Synthetic End-Cap Molecules. *Nano Lett.*, 15, 586–595 (2015).

[141] Guangyu Zhang, Pengfei Qi, Xinran Wang, Yuerui Lu, Xiaolin Li, Ryan Tu, Sarunya Bangsaruntip, David Mann, Li Zhang, and Hongjie Dai. Selective Etching of Metallic Carbon Nanotubes by Gas-Phase Reaction. *Science*, 314, 974–977 (2006).

[142] Yongho Joo, Gerald J. Brady, Michael S. Arnold, and Padma Gopalan. Dose-Controlled, Floating Evaporative Self-assembly and Alignment of Semiconducting Carbon Nanotubes from Organic Solvents. *Langmuir*, 30, 3460–3466 (2014).

[143] Xiaowei He, Weilu Gao, Lijuan Xie, Bo Li, Qi Zhang, Sidong Lei, John M. Robinson, Erik H. Hároz, Stephen K. Doorn, Weipeng Wang, Robert Vajtai, Pulickel M. Ajayan, W. Wade Adams, Robert H. Hauge, and Junichiro Kono. Wafer-scale monodomain films of spontaneously aligned single-walled carbon nanotubes. *Nat. Nanotechnol.*, 11, 633–638 (2016).

[144] Yiran Liang, Jiye Xia, and Xuelei Liang. Short channel carbon nanotube thin film transistors with high on/off ratio fabricated by two-step fringing field dielectrophoresis. *Sci. Bull.*, 61, 794–800 (2016).

[145] Andreas Malhofer, Marcel Rother, Yuriy Zakharko, Arko Graf, Stefan P. Schießl, and Jana Zaumseil. Direct visualization of percolation paths in carbon nanotube/polymer composites. *Org. Electron.*, 45, 151–158 (2017).

[146] Jianfu Ding, Zhao Li, Jacques Lefebvre, Fuyong Cheng, Girjesh Dubey, Shan Zou, Paul Finnie, Amy Hrdina, Ludmila Scoles, Gregory P. Lopinski, Christopher T. Kingston, Benoit Simard, and Patrick R. L. Malenfant. Enrichment of large-diameter semiconducting SWCNTs by polyfluorene extraction for high network density thin film transistors. *Nanoscale*, 6, 2328 (2014).

[147] Lijun Liu, Jie Han, Lin Xu, Jianshuo Zhou, Chenyi Zhao, Sujuan Ding, Huiwen Shi, Mengmeng Xiao, Li Ding, Ze Ma, Chuanhong Jin, Zhiyong Zhang, and Lian-Mao Peng. Aligned, high-density semiconducting carbon nanotube arrays for high-performance electronics. *Science*, 368, 850–856 (2020).

[148] Gerald J. Brady, Austin J. Way, Nathaniel S. Safron, Harold T. Evensen, Padma Gopalan, and Michael S. Arnold. Quasi-ballistic carbon nanotube array transistors with current density exceeding Si and GaAs. *Sci. Adv.*, 2, 1–9 (2016).

[149] Bongjun Kim, Michael L. Geier, Mark C. Hersam, and Ananth Dodabalapur. Inkjet printed circuits based on ambipolar and p-type carbon nanotube thin-film transistors. *Sci. Rep.*, 7, 39627 (2017).

[150] Junfeng Sun, Ashish Sapkota, Hyejin Park, Prince Wesley, Younsu Jung, Bijendra Bishow Maskey, Yushin Kim, Yutaka Majima, Jianfu Ding, Jianying Ouyang,

Chang Guo, Jacques Lefebvre, Zhao Li, Patrick R. L. Malenfant, Ali Javey, and Gyoujin Cho. Fully R2R-Printed Carbon-Nanotube-Based Limitless Length of Flexible Active-Matrix for Electrophoretic Display Application. *Adv. Electron. Mater.*, 6, 1901431 (2020).

[151] Luisa Petti, Niko Münzenrieder, Christian Vogt, Hendrik Faber, Lars Büthe, Giuseppe Cantarella, Francesca Bottacchi, Thomas D. Anthopoulos, and Gerhard Tröster. Metal oxide semiconductor thin-film transistors for flexible electronics. *Appl. Phys. Rev.*, 3, 021303 (2016).

[152] Heng Zhang, Li Xiang, Yingjun Yang, Mengmeng Xiao, Jie Han, Li Ding, Zhiyong Zhang, Youfan Hu, and Lian-Mao Peng. High-Performance Carbon Nanotube Complementary Electronics and Integrated Sensor Systems on Ultrathin Plastic Foil. *ACS Nano*, 12, 2773–2779 (2018).

[153] Lijun Liu, Li Ding, Donglai Zhong, Jie Han, Shuo Wang, Qinghai Meng, Chenguang Qiu, Xingye Zhang, Lian-Mao Peng, and Zhiyong Zhang. Carbon Nanotube Complementary Gigahertz Integrated Circuits and Their Applications on Wireless Sensor Interface Systems. *ACS Nano*, 13, 2526–2535 (2019).

[154] Changyong Cao, Joseph B. Andrews, and Aaron D. Franklin. Completely Printed, Flexible, Stable, and Hysteresis-Free Carbon Nanotube Thin-Film Transistors via Aerosol Jet Printing. *Adv. Electron. Mater.*, 3, 1700057 (2017).

[155] Daniel A. Bernards and George G. Malliaras. Steady-state and transient behavior of organic electrochemical transistors. *Adv. Funct. Mater.*, 17, 3538–3544 (2007).

[156] Jonathan Rivnay, Sahika Inal, Alberto Salleo, Róisín M. Owens, Magnus Berggren, and George G. Malliaras. Organic electrochemical transistors. *Nat. Rev. Mater.*, 3, 17086 (2018).

[157] Dion Khodagholy, Jonathan Rivnay, Michele Sessolo, Moshe Gurfinkel, Pierre Leleux, Leslie H. Jimison, Eleni Stavrinidou, Thierry Herve, Sébastien Sanaur, Róisín M. Owens, and George G. Malliaras. High transconductance organic electrochemical transistors. *Nat. Commun.*, 4, 1–6 (2013).

[158] Jonathan Rivnay, Pierre Leleux, Michele Sessolo, Dion Khodagholy, Thierry Hervé, Michel Fiocchi, and George G. Malliaras. Organic Electrochemical Transistors with Maximum Transconductance at Zero Gate Bias. *Adv. Mater.*, 25, 7010–7014 (2013).

[159] Maria Daniela Angione, Serafina Cotrone, Maria Magliulo, Antonia Mallardi, Davide Altamura, Cinzia Giannini, Nicola Cioffi, Luigia Sabbatini, Emiliano Fratini, Piero Baglioni, Gaetano Scamarcio, Gerardo Palazzo, and Luisa Torsi. Interfacial electronic effects in functional biolayers integrated into organic field-effect transistors. *Proc. Natl. Acad. Sci.*, 109, 6429–6434 (2012).

[160] Srikanth Ranganathan and Richard L. McCreery. Electroanalytical Performance of Carbon Films with Near-Atomic Flatness. *Anal. Chem.*, 73, 893–900 (2001).

[161] Jonathan Rivnay, Pierre Leleux, Marc Ferro, Michele Sessolo, Adam Williamson, Dimitrios A. Koutsouras, Dion Khodagholy, Marc Ramuz, Xenofon Strakosas, Roisin M. Owens, Christian Benar, Jean-Michel Badier, Christophe Bernard, and George G. Malliaras. High-performance transistors for bioelectronics through tuning of channel thickness. *Sci. Adv.*, 1, 1–6 (2015).

[162] Peng Lin and Feng Yan. Organic Thin-Film Transistors for Chemical and Biological Sensing. *Adv. Mater.*, 24, 34–51 (2012).

[163] Dion Khodagholy, Thomas Doublet, Pascale Quilichini, Moshe Gurfinkel, Pierre Leleux, Antoine Ghestem, Esma Ismailova, Thierry Hervé, Sébastien Sanaur, Christophe Bernard, and George G. Malliaras. In vivo recordings of brain activity using organic transistors. *Nat. Commun.*, 4, 1575 (2013).

[164] Paschalis Gkoupidenis, Nathan Schaefer, Benjamin Garlan, and George G. Malliaras. Neuromorphic Functions in PEDOT:PSS Organic Electrochemical Transistors. *Adv. Mater.*, 27, 7176–7180 (2015).

[165] Sahika Inal, George G. Malliaras, and Jonathan Rivnay. Benchmarking organic mixed conductors for transistors. *Nat. Commun.*, 8, 1–6 (2017).

[166] Jacob T. Friedlein, Robert R. McLeod, and Jonathan Rivnay. Device physics of organic electrochemical transistors (2018).

[167] Maximilian Moser, Tania Cecilia Hidalgo, Jokubas Surgailis, Johannes Gladisch, Sarbani Ghosh, Rajendar Sheelamanthula, Quentin Thiburce, Alexander Giovannitti, Alberto Salleo, Nicola Gasparini, Andrew Wadsworth, Igor Zozoulenko, Magnus Berggren, Eleni Stavrinidou, Sahika Inal, and Iain McCulloch. Side Chain Redistribution as a Strategy to Boost Organic Electrochemical Transistor Performance and Stability. *Adv. Mater.*, 32, 1–6 (2020).

[168] Eleni Stavrinidou, Pierre Leleux, Harizo Rajaona, Dion Khodagholy, Jonathan Rivnay, Manfred Lindau, Sébastien Sanaur, and George G Malliaras. Direct Measurement of Ion Mobility in a Conducting Polymer. *Adv. Mater.*, 25, 4488–4493 (2013).

[169] Sahika Inal, George G. Malliaras, and Jonathan Rivnay. Optical study of electrochromic moving fronts for the investigation of ion transport in conducting polymers. *J. Mater. Chem. C*, 4, 3942–3947 (2016).

[170] Yue Wang, Chenxin Zhu, Raphael Pfattner, Hongping Yan, Lihua Jin, Shucheng Chen, Francisco Molina-Lopez, Franziska Lissel, Jia Liu, Noelle I. Rabiah, Zheng Chen, Jong Won Chung, Christian Linder, Michael F. Toney, Boris Murmann, and Zhenan Bao. A highly stretchable, transparent, and conductive polymer. *Sci. Adv.*, 3, 1–11 (2017).

[171] Maria Asplund, Tobias Nyberg, and Olle Inganäs. Electroactive polymers for neural interfaces. *Polym. Chem.*, 1, 1341–1520 (2010).

[172] Daniele Mantione, Isabel del Agua, Wandert Schaafsma, Mohammed ElMahmoudy, Ilke Uguz, Ana Sanchez-Sanchez, Haritz Sardon, Begoña Castro, George G. Malliaras, and David Mecerreyes. Low-Temperature Cross-Linking of PEDOT:PSS Films Using Divinylsulfone. *ACS Appl. Mater. Interfaces*, 9, 18254–18262 (2017).

[173] Maximilian Moser, Johannes Gladisch, Sarbani Ghosh, Tania Cecilia Hidalgo, James F. Ponder, Rajendar Sheelamanthula, Quentin Thiburce, Nicola Gasparini, Andrew Wadsworth, Alberto Salleo, Sahika Inal, Magnus Berggren, Igor Zozoulenko, Eleni Stavrinidou, and Iain McCulloch. Controlling Electrochemically Induced Volume Changes in Conjugated Polymers by Chemical Design: from Theory to Devices. *Adv. Funct. Mater.*, 31, 1–10 (2021).

[174] Achilleas Savva, Rawad Hallani, Camila Cendra, Jokubas Surgailis, Tania C. Hidalgo, Shofarul Wustoni, Rajendar Sheelamanthula, Xingxing Chen, Mindaugas Kirkus, Alexander Giovannitti, Alberto Salleo, Iain McCulloch, and Sahika Inal. Balancing Ionic and Electronic Conduction for High-Performance Organic Electrochemical Transistors. *Adv. Funct. Mater.*, 30, 1907657 (2020).

[175] Achilleas Savva, Camila Cendra, Andrea Giugni, Bruno Torre, Jokubas Surgailis, David Ohayon, Alexander Giovannitti, Iain McCulloch, Enzo Di Fabrizio, Alberto Salleo, Jonathan Rivnay, and Sahika Inal. Influence of Water on the Performance of Organic Electrochemical Transistors. *Chem. Mater.*, 31, 927–937 (2019).

[176] Alexander Giovannitti, Dan-Tiberiu Sbircea, Sahika Inal, Christian B. Nielsen, Enrico Bandiello, David A. Hanifi, Michele Sessolo, George G. Malliaras, Iain McCulloch, and Jonathan Rivnay. Controlling the mode of operation of organic transistors through side-chain engineering. *Proc. Natl. Acad. Sci.*, 113, 12017–12022 (2016).

[177] Christian B. Nielsen, Alexander Giovannitti, Dan Tiberiu Sbircea, Enrico Bandiello, Muhammad R. Niazi, David A. Hanifi, Michele Sessolo, Aram Amassian, George G. Malliaras, Jonathan Rivnay, and Iain McCulloch. Molecular Design of Semiconducting Polymers for High-Performance Organic Electrochemical Transistors. *J. Am. Chem. Soc.*, 138, 10252–10259 (2016).

[178] Alexander Giovannitti, Christian B. Nielsen, Dan-Tiberiu Sbircea, Sahika Inal, Mary Donahue, Muhammad R. Niazi, David A. Hanifi, Aram Amassian, George G. Malliaras, Jonathan Rivnay, and Iain McCulloch. N-type organic electrochemical transistors with stability in water. *Nat. Commun.*, 7, 13066 (2016).

[179] Eleni Stavrinidou, Orawan Winther-Jensen, Bijan S. Shekibi, Vanessa Armel, Jonathan Rivnay, Esma Ismailova, Sébastien Sanaur, George G. Malliaras, and Bjorn Winther-Jensen. Engineering hydrophilic conducting composites with enhanced ion mobility. *Phys. Chem. Chem. Phys.*, 16, 2275–2279 (2014).

[180] Jinfeng Li and Peter J. Burke. Measurement of the combined quantum and electrochemical capacitance of a carbon nanotube. *Nat. Commun.*, 10, 3598 (2019).

[181] Jie Jiang, Junjie Guo, Xiang Wan, Yi Yang, Haipeng Xie, Dongmei Niu, Junliang Yang, Jun He, Yongli Gao, and Qing Wan. 2D MoS 2 Neuromorphic Devices for Brain-Like Computational Systems. *Small*, 13, 1700933 (2017).

[182] Stephen Ong and Shahadat Uddin. Data science and artificial intelligence in project management: The past, present and future. *J. Mod. Proj. Manag.*, 7, 26–33 (2020).

[183] Khan Muhammad, Amin Ullah, Jaime Lloret, Javier Del Ser, and Victor Hugo C. de Albuquerque. Deep Learning for Safe Autonomous Driving: Current Challenges and Future Directions. *IEEE Trans. Intell. Transp. Syst.*, 22, 4316–4336 (2021).

[184] Dawid Polap and Marcin Wozniak. Voice recognition by neuro-heuristic method. *Tsinghua Sci. Technol.*, 24, 9–17 (2019).

[185] Yann LeCun, Yoshua Bengio, and Geoffrey Hinton. Deep learning. *Nature*, 521, 436–444 (2015).

[186] J. von Neumann. First draft of a report on the EDVAC. *IEEE Ann. Hist. Comput.*, 15, 27–75 (1993).

[187] Catherine D. Schuman, Thomas E. Potok, Robert M. Patton, J. Douglas Birdwell, Mark E. Dean, Garrett S. Rose, and James S. Plank. A Survey of Neuromorphic Computing and Neural Networks in Hardware. *1705.06963*, pages 1–88 (2017).

[188] Sébastien Pecqueur, Dominique Vuillaume, and Fabien Alibart. Perspective: Organic electronic materials and devices for neuromorphic engineering. *J. Appl. Phys.*, 124 (2018).

[189] Frederico A.C. Azevedo, Ludmila R.B. Carvalho, Lea T. Grinberg, José Marcelo Farfel, Renata E.L. Ferretti, Renata E.P. Leite, Wilson Jacob Filho, Roberto Lent, and Suzana Herculano-Houzel. Equal numbers of neuronal and nonneuronal cells make the human brain an isometrically scaled-up primate brain. *J. Comp. Neurol.*, 513, 532–541 (2009).

[190] Bente Pakkenberg. Aging and the human neocortex. *Exp. Gerontol.*, 38, 95–99 (2003).

[191] A. L. Hodgkin and A. F. Huxley. A quantitative description of membrane current and its application to conduction and excitation in nerve. *J. Physiol.*, 117, 500–544 (1952).

[192] Alberto E. Pereda. Electrical synapses and their functional interactions with chemical synapses. *Nat. Rev. Neurosci.*, 15, 250–263 (2014).

[193] Fred Attneave, M. B., and D. O. Hebb. The Organization of Behavior; A Neuropsychological Theory. *Am. J. Psychol.*, 63, 633 (1949).

[194] Laurence F Abbott and Wade G. Regehr. Synaptic computation. *Nature*, 431, 796–803 (2004).

[195] Guo-qiang Bi and Mu-ming Poo. Synaptic Modifications in Cultured Hippocampal Neurons: Dependence on Spike Timing, Synaptic Strength, and Postsynaptic Cell Type. *J. Neurosci.*, 18, 10464–10472 (1998).

[196] H. Markram, W. Gerstner, and P. J. Sjöström. Spike-Timing-Dependent Plasticity: A Comprehensive Overview. *Front. Synaptic Neurosci.*, 4, 2010–2012 (2012).

[197] Carver Mead. Neuromorphic electronic systems. *Proc. IEEE*, 78, 1629–1636 (1990).

[198] Leon Chua. Memristor-The missing circuit element. *IEEE Trans. Circuit Theory*, 18, 507–519 (1971).

[199] Dmitri B. Strukov, Gregory S. Snider, Duncan R. Stewart, and R. Stanley Williams. The missing memristor found. *Nature*, 453, 80–83 (2008).

[200] Shilei Dai, Yiwei Zhao, Yan Wang, Junyao Zhang, Lu Fang, Shu Jin, Yinlin Shao, and Jia Huang. Recent Advances in Transistor-Based Artificial Synapses. *Adv. Funct. Mater.*, 29, 1903700 (2019).

[201] Yi Ren, Jia-Qin Yang, Li Zhou, Jing-Yu Mao, Shi-Rui Zhang, Ye Zhou, and Su-Ting Han. Gate-Tunable Synaptic Plasticity through Controlled Polarity of Charge Trapping in Fullerene Composites. *Adv. Funct. Mater.*, 28, 1805599 (2018).

[202] Huilin Li, Ruopeng Wang, Su-Ting Han, and Ye Zhou. Ferroelectric polymers for non-volatile memory devices: a review. *Polym. Int.*, 69, 533–544 (2020).

[203] H. K. Li, T. P. Chen, P. Liu, S. G. Hu, Y. Liu, Q. Zhang, and P. S. Lee. A light-stimulated synaptic transistor with synaptic plasticity and memory functions based on InGaZnO x –Al 2 O 3 thin film structure. *J. Appl. Phys.*, 119, 244505 (2016).

[204] Jian Shi, Sieu D. Ha, You Zhou, Frank Schoofs, and Shriram Ramanathan. A correlated nickelate synaptic transistor. *Nat. Commun.*, 4, 2676 (2013).

[205] Chuan Qian, Jia Sun, Ling An Kong, Guangyang Gou, Junliang Yang, Jun He, Yongli Gao, and Qing Wan. Artificial Synapses Based on in-Plane Gate Organic Electrochemical Transistors. *ACS Appl. Mater. Interfaces*, 8, 26169–26175 (2016).

[206] Paschalis Gkoupidenis, Nathan Schaefer, Xenofon Strakosas, Jessamyn A. Fairfield, and George G. Malliaras. Synaptic plasticity functions in an organic electrochemical transistor. *Appl. Phys. Lett.*, 107, 263302 (2015).

[207] Henry Markram. The Blue Brain Project. In *Proc. 2006 ACM/IEEE Conf. Supercomput. - SC '06*, volume 7, page 53. ACM Press, New York, New York, USA (2006).

[208] Christian Pehle, Sebastian Billaudelle, Benjamin Cramer, Jakob Kaiser, Korbinian Schreiber, Yannik Stradmann, Johannes Weis, Aron Leibfried, Eric Müller, and Johannes Schemmel. The BrainScaleS-2 Accelerated Neuromorphic System With Hybrid Plasticity. *Front. Neurosci.*, 16, 1–21 (2022).

[209] Sebastian Schmitt, Johann Klahn, Guillaume Bellec, Andreas Grubl, Maurice Guttler, Andreas Hartel, Stephan Hartmann, Dan Husmann, Kai Husmann, Sebastian Jeltsch, Vitali Karasenko, Mitja Kleider, Christoph Koke, Alexander Kononov, Christian Mauch, Eric Muller, Paul Muller, Johannes Partzsch, Mihai A. Petrovici, Stefan Schiefer, Stefan Scholze, Vasilis Thanasoulis, Bernhard Vogginger, Robert Legenstein, Wolfgang Maass, Christian Mayr, Rene Schuffny, Johannes Schemmel, and Karlheinz Meier. Neuromorphic hardware in the loop: Training a deep spiking network on the BrainScaleS wafer-scale system. In *2017 Int. Jt. Conf. Neural Networks*, volume 2017-May, pages 2227–2234. IEEE (2017).

[210] Elliot J. Fuller, Farid El Gabaly, François Léonard, Sapan Agarwal, Steven J. Plimpton, Robin B. Jacobs-Gedrim, Conrad D. James, Matthew J. Marinella, and A. Alec Talin. Li-Ion Synaptic Transistor for Low Power Analog Computing. *Adv. Mater.*, 29, 1–8 (2017).

[211] Sungho Kim, Yongwoo Lee, Hee Dong Kim, and Sung Jin Choi. Parallel weight update protocol for a carbon nanotube synaptic transistor array for accelerating neuromorphic computing. *Nanoscale*, 12, 2040–2046 (2020).

[212] Chuan Sen Yang, Da Shan Shang, Nan Liu, Elliot J. Fuller, Sapan Agrawal, A. Alec Talin, Yong Qing Li, Bao Gen Shen, and Young Sun. All-Solid-State Synaptic Transistor with Ultralow Conductance for Neuromorphic Computing. *Adv. Funct. Mater.*, 28, 1–10 (2018).

[213] Sapan Agarwal, Steven J. Plimpton, David R. Hughart, Alexander H. Hsia, Isaac Richter, Jonathan A. Cox, Conrad D. James, and Matthew J. Marinella. Resistive memory device requirements for a neural algorithm accelerator. *Proc. Int. Jt. Conf. Neural Networks*, 2016-Octob, 929–938 (2016).

[214] Simon B. Laughlin, Rob R. de Ruyter van Steveninck, and John C. Anderson. The metabolic cost of neural information. *Nat. Neurosci.*, 1, 36–41 (1998).

[215] Zhongrui Wang, Saumil Joshi, Sergey E. Savel'ev, Hao Jiang, Rivu Midya, Peng Lin, Miao Hu, Ning Ge, John Paul Strachan, Zhiyong Li, Qing Wu, Mark Barnell, Geng Lin Li, Huolin L. Xin, R. Stanley Williams, Qiangfei Xia, and J. Joshua Yang. Memristors with diffusive dynamics as synaptic emulators for neuromorphic computing. *Nat. Mater.*, 16, 101–108 (2017).

[216] Yuchao Yang, Peng Gao, Linze Li, Xiaoqing Pan, Stefan Tappertzhofen, Shinhyun Choi, Rainer Waser, Ilia Valov, and Wei D. Lu. Electrochemical dynamics of nanoscale metallic inclusions in dielectrics. *Nat. Commun.*, 5, 4232 (2014).

[217] Sizhao Li, Fei Zeng, Chao Chen, Hongyan Liu, Guangsheng Tang, Shuang Gao, Cheng Song, Yisong Lin, Feng Pan, and Dong Guo. Synaptic plasticity and learning behaviours mimicked through Ag interface movement in an Ag/conducting polymer/Ta memristive system. *J. Mater. Chem. C*, 1, 5292–5298 (2013).

[218] Wentao Xu, Himchan Cho, Young Hoon Kim, Young Tae Kim, Christoph Wolf, Chan Gyung Park, and Tae Woo Lee. Organometal Halide Perovskite Artificial Synapses. *Adv. Mater.*, 28, 5916–5922 (2016).

[219] Christophe Novembre, David Guérin, Kamal Lmimouni, Christian Gamrat, and Dominique Vuillaume. Gold nanoparticle-pentacene memory transistors. *Appl. Phys. Lett.*, 92, 90–93 (2008).

[220] Fabien Alibart, Stéphane Pieutin, David Guérin, Christophe Novembre, Stéphane Lenfant, Kamal Lmimouni, Christian Gamrat, and Dominique Vuillaume. An organic nanoparticle transistor behaving as a biological spiking synapse. *Adv. Funct. Mater.*, 20, 330–337 (2010).

[221] T. Zhang, D. Guérin, F. Alibart, D. Vuillaume, K. Lmimouni, S. Lenfant, A. Yassin, M. Oçafrain, P. Blanchard, and J. Roncali. Negative Differential Resistance, Memory, and Reconfigurable Logic Functions Based on Monolayer Devices Derived from Gold Nanoparticles Functionalized with Electropolymerizable TEDOT Units. *J. Phys. Chem. C*, 121, 10131–10139 (2017).

[222] Chang-Hyun Kim, Sujin Sung, and Myung-Han Yoon. Synaptic organic transistors with a vacuum-deposited charge-trapping nanosheet. *Sci. Rep.*, 6, 33355 (2016).

[223] Lin Shao, Hailu Wang, Yi Yang, Yongli He, Yicheng Tang, Hehai Fang, Jianwen Zhao, Hongshan Xiao, Kun Liang, Miaomiao Wei, Wenya Xu, Manman Luo, Qing Wan, Weida Hu, Tianqi Gao, and Zheng Cui. Optoelectronic Properties of Printed Photogating Carbon Nanotube Thin Film Transistors and Their Application for Light-Stimulated Neuromorphic Devices. *ACS Appl. Mater. Interfaces*, 11, 12161–12169 (2019).

[224] Lin Shao, Min Li, Peisong Wu, Fang Wang, Shulin Chen, Weida Hu, Hua Wang, Zheng Cui, and Jianwen Zhao. Optically and electrically modulated printed carbon nanotube synaptic transistors with a single input terminal and multi-functional output characteristics. *J. Mater. Chem. C*, 8, 6914–6922 (2020).

[225] Min Li, Ziyu Xiong, Shuangshuang Shao, Lin Shao, Su-Ting Han, Hua Wang, and Jianwen Zhao. Multimodal optoelectronic neuromorphic electronics based on lead-free perovskite-mixed carbon nanotubes. *Carbon N. Y.*, 176, 592–601 (2021).

[226] Ling-an Kong, Jia Sun, Chuan Qian, Ying Fu, Juxiang Wang, Junliang Yang, and Yongli Gao. Long-term synaptic plasticity simulated in ionic liquid/polymer hybrid electrolyte gated organic transistors. *Org. Electron.*, 47, 126–132 (2017).

[227] J. Joshua Yang, M.-X. Zhang, Matthew D. Pickett, Feng Miao, John Paul Strachan, Wen-Di Li, Wei Yi, Douglas A. A. Ohlberg, Byung Joon Choi, Wei Wu, Janice H. Nickel, Gilberto Medeiros-Ribeiro, and R. Stanley Williams. Engineering nonlinearity into memristors for passive crossbar applications. *Appl. Phys. Lett.*, 100, 113501 (2012).

[228] Navnidhi K Upadhyay, Hao Jiang, Zhongrui Wang, Shiva Asapu, Qiangfei Xia, and J. Joshua Yang. Emerging Memory Devices for Neuromorphic Computing. *Adv. Mater. Technol.*, 4, 1–13 (2019).

[229] Zhengguo Xiao and Jinsong Huang. Energy-Efficient Hybrid Perovskite Memristors and Synaptic Devices. *Adv. Electron. Mater.*, 2, 1600100 (2016).

[230] Tim Leydecker, Martin Herder, Egon Pavlica, Gvido Bratina, Stefan Hecht, Emanuele Orgiu, and Paolo Samorì. Flexible non-volatile optical memory thin-film transistor device with over 256 distinct levels based on an organic bicomponent blend. *Nat. Nanotechnol.*, 11, 769–775 (2016).

[231] Imke Krauhausen, Dimitrios A. Koutsouras, Armantas Melianas, Scott T. Keene, Katharina Lieberth, Hadrien Ledanseur, Rajendar Sheelamanthula, Alexander Giovannitti, Fabrizio Torricelli, Iain Mcculloch, Paul W. M. Blom, Alberto Salleo, Yoeri van de Burgt, and Paschalis Gkoupidenis. Organic neuromorphic electronics for sensorimotor integration and learning in robotics. *Sci. Adv.*, 7, 1–9 (2021).

[232] Elliot J. Fuller, Scott T. Keene, Armantas Melianas, Zhongrui Wang, Sapan Agarwal, Yiyang Li, Yaakov Tuchman, Conrad D. James, Matthew J. Marinella, J. Joshua Yang, Alberto Salleo, and A. Alec Talin. Parallel programming of an ionic floating-gate memory array for scalable neuromorphic computing. *Science*, 364, 570–574 (2019).

[233] Chaoxing Wu, Tae Whan Kim, Hwan Young Choi, Dmitri B. Strukov, and J. Joshua Yang. Flexible three-dimensional artificial synapse networks with correlated learning and trainable memory capability. *Nat. Commun.*, 8, 752 (2017).

[234] Florian Trilling, Michelle Kathrin Ausländer, and Ullrich Scherf. Ladder-Type Polymers and Ladder-Type Polyelectrolytes with On-Chain Dibenz[a, h]anthracene Chromophores. *Macromolecules*, 52, 3115–3122 (2019).

[235] Daniel Heimfarth, Merve Balcı Leinen, Patrick Klein, Sybille Allard, Ullrich Scherf, and Jana Zaumseil. Enhancing Electrochemical Transistors Based on Polymer-Wrapped (6,5) Carbon Nanotube Networks with Ethylene Glycol Side Chains. *ACS Appl. Mater. Interfaces*, 14, 8209–8217 (2022).

[236] Patrick Klein. *Konjugierte Polymere für Sensorikanwendungen.* Ph.D. thesis (2021).

[237] Marcel Rother. *Engineering of Aerosol-Jet Printed Carbon Nanotube Network Transistors.* Ph.D. thesis (2019).

[238] Shiheng Lu, Joanne Zheng, Jorge A. Cardenas, Nicholas X. Williams, Yuh Chen Lin, and Aaron D. Franklin. Uniform and Stable Aerosol Jet Printing of Carbon Nanotube Thin-Film Transistors by Ink Temperature Control. *ACS Appl. Mater. Interfaces*, 12, 43083–43089 (2020).

[239] Bryan D Paulsen, Klas Tybrandt, Eleni Stavrinidou, and Jonathan Rivnay. Organic mixed ionic–electronic conductors. *Nat. Mater.*, 19, 13–26 (2020).

[240] Erica Zeglio and Olle Inganäs. Active Materials for Organic Electrochemical Transistors. *Adv. Mater.*, 30, 1–18 (2018).

[241] Elayne M. Thomas, Phong H. Nguyen, Seamus D. Jones, Michael L. Chabinyc, and Rachel A. Segalman. Electronic, Ionic, and Mixed Conduction in Polymeric Systems. *Annu. Rev. Mater. Res.*, 51, 1–20 (2021).

[242] Bin Meng, Jun Liu, and Lixiang Wang. Oligo(ethylene glycol) as side chains of conjugated polymers for optoelectronic applications. *Polym. Chem.*, 11, 1261–1270 (2020).

[243] Rajiv Giridharagopal, Jiajie Guo, Jessica Kong, and David S. Ginger. Nanowire Architectures Improve Ion Uptake Kinetics in Conjugated Polymer Electrochemical Transistors. *ACS Appl. Mater. Interfaces*, 13, 34616–34624 (2021).

[244] Hengda Sun, Mikhail Vagin, Suhao Wang, Xavier Crispin, Robert Forchheimer, Magnus Berggren, and Simone Fabiano. Complementary Logic Circuits Based on High-Performance n-Type Organic Electrochemical Transistors. *Adv. Mater.*, 30, 1704916 (2018).

[245] Samuel D. Stranks, Chaw Keong Yong, Jack A. Alexander-Webber, Christian Weisspfennig, Michael B. Johnston, Laura M. Herz, and Robin J. Nicholas. Nanoengineering coaxial carbon nanotube-dual-polymer heterostructures. *ACS Nano*, 6, 6058–6066 (2012).

[246] Ma-Guang Zhu, Zhiyong Zhang, and Lian-Mao Peng. High-Performance and Radiation-Hard Carbon Nanotube Complementary Static Random-Access Memory. *Adv. Electron. Mater.*, 5, 1900313 (2019).

[247] Atsuko Sekiguchi, Fumiaki Tanaka, Takeshi Saito, Yuki Kuwahara, Shunsuke Sakurai, Don N. Futaba, Takeo Yamada, and Kenji Hata. Robust and Soft Elastomeric Electronics Tolerant to Our Daily Lives. *Nano Lett.*, 15, 5716–5723 (2015).

[248] Wytse Talsma, Aprizal Akbar Sengrian, Jorge Mario Salazar-Rios, Herman Duim, Mustapha Abdu-Aguye, Stefan Jung, Sybille Allard, Ullrich Scherf, and Maria Antonietta Loi. Remarkably Stable, High-Quality Semiconducting Single-Walled Carbon Nanotube Inks for Highly Reproducible Field-Effect Transistors. *Adv. Electron. Mater.*, 5, 1900288 (2019).

[249] Severin Schneider, Jacques Lefebvre, Nicolas J. Diercks, Felix J. Berger, François Lapointe, Juliette Schleicher, Patrick R. L. Malenfant, and Jana Zaumseil. Phenanthroline Additives for Enhanced Semiconducting Carbon Nanotube Dispersion Stability and Transistor Performance. *ACS Appl. Nano Mater.*, 3, 12314–12324 (2020).

[250] Florian Jakubka, Stefan B. Grimm, Yuriy Zakharko, Florentina Gannott, and Jana Zaumseil. Trion electroluminescence from semiconducting carbon nanotubes. *ACS Nano*, 8, 8477–8486 (2014).

[251] Steven G. Noyce, James L. Doherty, Zhihui Cheng, Hui Han, Shane Bowen, and

Aaron D. Franklin. Electronic Stability of Carbon Nanotube Transistors under Long-Term Bias Stress. *Nano Lett.*, 19, 1460–1466 (2019).

[252] Philip Schmode, Achilleas Savva, Robert Kahl, David Ohayon, Florian Meichsner, Oleksandr Dolynchuk, Thomas Thurn-Albrecht, Sahika Inal, and Mukundan Thelakkat. The Key Role of Side Chain Linkage in Structure Formation and Mixed Conduction of Ethylene Glycol Substituted Polythiophenes. *ACS Appl. Mater. Interfaces*, 12, 13029–13039 (2020).

[253] Camila Cendra, Alexander Giovannitti, Achilleas Savva, Vishak Venkatraman, Iain McCulloch, Alberto Salleo, Sahika Inal, and Jonathan Rivnay. Role of the Anion on the Transport and Structure of Organic Mixed Conductors. *Adv. Funct. Mater.*, 29, 1–11 (2019).

[254] O. A. Ageev, Yu. F. Blinov, O. I. Il'in, A. S. Kolomiitsev, B. G. Konoplev, M. V. Rubashkina, V. A. Smirnov, and A. A. Fedotov. Memristor effect on bundles of vertically aligned carbon nanotubes tested by scanning tunnel microscopy. *Tech. Phys.*, 58, 1831–1836 (2013).

[255] Marina V. Il'ina, Oleg I. Il'in, Yuriy F. Blinov, Vladimir A. Smirnov, Alexey S. Kolomiytsev, Alexander A. Fedotov, Boris G. Konoplev, and Oleg A. Ageev. Memristive switching mechanism of vertically aligned carbon nanotubes. *Carbon N. Y.*, 123, 514–524 (2017).

[256] Karim Gacem, Jean-Marie Retrouvey, Djaafar Chabi, Arianna Filoramo, Weisheng Zhao, Jacques-Olivier Klein, and Vincent Derycke. Neuromorphic function learning with carbon nanotube based synapses. *Nanotechnology*, 24, 384013 (2013).

[257] C-L Chen, K. Kim, Q. Truong, A. Shen, Z. Li, and Y. Chen. A spiking neuron circuit based on a carbon nanotube transistor. *Nanotechnology*, 23, 275202 (2012).

[258] Kyunghyun Kim, Chia Ling Chen, Quyen Truong, Alex M. Shen, and Yong Chen. A carbon nanotube synapse with dynamic logic and learning. *Adv. Mater.*, 25, 1693–1698 (2013).

[259] Vikash Kaphle, Shiyi Liu, Chang-Min Keum, and Björn Lüssem. Organic Electrochemical Transistors Based on Room Temperature Ionic Liquids: Performance and Stability. *Phys. status solidi*, 215, 1800631 (2018).

[260] Christian Tetzlaff, Christoph Kolodziejski, Irene Markelic, and Florentin Wörgötter. Time scales of memory, learning, and plasticity. *Biol. Cybern.*, 106, 715–726 (2012).

[261] Takeo Ohno, Tsuyoshi Hasegawa, Tohru Tsuruoka, Kazuya Terabe, James K. Gimzewski, and Masakazu Aono. Short-term plasticity and long-term potentiation mimicked in single inorganic synapses. *Nat. Mater.*, 10, 591–595 (2011).

[262] Gayle M. Wittenberg and S. S.-H. Wang. Malleability of Spike-Timing-Dependent Plasticity at the CA3-CA1 Synapse. *J. Neurosci.*, 26, 6610–6617 (2006).

[263] Harel Shouval. Spike timing dependent plasticity: a consequence of more fundamental learning rules. *Front. Comput. Neurosci.*, 4, 1–13 (2010).

[264] Navnidhi K. Upadhyay, Saumil Joshi, and J. Joshua Yang. Synaptic electronics and neuromorphic computing. *Sci. China Inf. Sci.*, 59, 1–26 (2016).

[265] Jennifer Hasler and Bo Marr. Finding a roadmap to achieve large neuromorphic hardware systems. *Front. Neurosci.*, 7, 1–29 (2013).

[266] Gang Liu, Cheng Wang, Wenbin Zhang, Liang Pan, Chaochao Zhang, Xi Yang, Fei Fan, Yu Chen, and Run Wei Li. Organic Biomimicking Memristor for Information Storage and Processing Applications. *Adv. Electron. Mater.*, 2, 1–8 (2016).

[267] Alex Chortos, Igor Pochorovski, Pei Lin, Gregory Pitner, Xuzhou Yan, Theodore Z. Gao, John W. F. To, Ting Lei, John W. Will, H.-S. Philip Wong, and Zhenan Bao. Universal Selective Dispersion of Semiconducting Carbon Nanotubes from Commercial Sources Using a Supramolecular Polymer. *ACS Nano*, 11, 5660–5669 (2017).

[268] Lingyun Lyu, Kazuhiro Kirihara, Yuki Okigawa, Masataka Hasegawa, Wuxiao Ding, Ying Wang, Masakazu Mukaida, Ying Zhou, and Qingshuo Wei. Extracting carrier mobility using a photoinduced charge transfer reaction: From conducting polymers to nanocarbon materials. *Org. Electron.*, 78, 105615 (2020).

[269] Pasquale D' Angelo, Nicola Coppedè, Giuseppe Tarabella, Agostino Romeo, Francesco Gentile, Salvatore Iannotta, Enzo Di Fabrizio, and Roberto Mosca. Liquid electrolyte positioning along the device channel influences the operation of Organic Electro-Chemical Transistors. *Org. Electron.*, 15, 3016–3023 (2014).

Acknowledgements/Danksagung

Zum Abschluss dieser Arbeit bleibt mir nur allen danke zu sagen, die mich bei meiner Promotion unterstützt haben. Langjährige Projekte wie eine Doktorarbeit gehen immer mit Höhen und Tiefen einher, wobei das Erreichen der Höhen und das Durchstehen der Tiefen nicht ohne das richtige Team möglich sind.

Zuerst möchte ich *Prof. Dr. Jana Zaumseil* danken, für die Möglichkeit in ihrer Arbeitsgruppe zu Promovieren. Danke für die engagierte Betreuung und alles was ich bei Dir und Deiner Arbeitsgruppe lernen konnte.
Vielen Dank an *Prof. Dr. Martijn Kemerink* für das Übernehmen des Zweitgutachtens, sowie *Prof. Dr. Sandra Klevansky* und *Prof. Dr. Thomas Pfeifer* für das Vervollständigen meines Prüfungskomitees.
Bei allen Alumni, die ich kennenlernen durfte, sowie allen aktuellen Mitgliedern der *NMOE-* und der *PC2D-Arbeitsgruppe* möchte ich mich herzlich für das angenehme Arbeitsklima bedanken. Den freundlichen Umgang miteinander und die stete Hilfsbereitschaft aller habe ich sehr genossen. Danke, *Maximilian Brohmann*, für die herzliche Aufnahme in die Arbeitsgruppe und deine Unterstützung in der Anfangsphase meiner Promotion. Ich hätte mir keinen besseren Mentor wünschen können. Danke, *Severin Schneider*, für die vielen Gespräche während Kaffeepausen und dein offenes Ohr für alle Probleme. Ich habe deine qualifizierte Meinung immer sehr geschätzt. Danke, *Maik Matthiesen*, für deine ruhige und besonnene Art und die viele Arbeit, die du trotz genügend eigener Aufgaben, für die Gruppe geleistet hast. Danke, *Kevin Synnatschke*, für deine vorgelebte Zielstrebigkeit und Energie.
Vielen Dank auch an *Sonja Wieland*, *Nicolas Zorn*, *Jan Gotthardt*, *Steffen Ott* und *Gergana Borisova* für das Korrekturlesen dieser Arbeit.
Thank you, *Merve Balcı*, for all your help and your patience with the many last batches.
Danke, *Simon Settele*, für die gute Zeit auf meiner einzigen Vor-Ort-Konferenz außerhalb

Deutschlands (in dem Zusammenhang auch danke Covid...).
Danke, *Sebastian Lindenthal*, dass du mit deiner schallenden und ansteckenden Lache eine Quelle der guten Laune bist.
Many thanks to *Felix Berger, Jan Lüttgens, Manuel Hertzog, Elisa Fresta, Beata Szydlowska, Maximilian Krings, Sebastian Grieger, Abdurrahman Ali El Yumin, Yan Huang, Finn Sebastian, Tim Nowack Angus Hawkey, Niklas Herrmann, Parvathi Valsalan, Farnia Rashvand and Vaisnavi Rao* for creating such a nice and friendly but also productive working athmosphere.
Ein großes Dankeschön auch an die vielen Laborwichtel, die ständig für einen gefüllten Schrank mit Dispersionen gesorgt haben.
Danke an *Patrick Klein* für das Synthetisieren des in dieser Arbeit verwendeten Polymers.
Außerdem danke ich meinen beiden Studenten *Konrad Münch* und *Heiko Mager*. Ich habe bei der Betreuung viel gelernt und bin stolz auf die Ergebnisse und eure guten Abschlussarbeiten, die dabei herausgekommen sind.
Ich möchte mich ebenfalls sehr für die hervorragende Arbeit der Mitarbeiter am Institut bedanken. Vielen Dank *Klaus Schmitt* und der gesamten Feinmechanikwerkstatt für die professionelle Umsetzung von diversen Projekten. Danke, *Günter Meinusch* und *Peter Jeschka*, für die kompetente Unterstützung bei allen Elektronik und IT-Problemen und für das Bauen und Programmieren der Analogschalter. Weiterhin vielen Dank an *Karin Jordan*, *Swetlana Duchnay*, *Benjamin Scherke* und *Isabella Haffelder*, für die Hilfestellung bei allen Verwaltungsthemen.
Darüber hinaus, vielen Dank Steffen, für die lehrreichen Schachlektionen nach dem Mittagessen. Danke auch, an alle Mitspieler der mittäglichen Skatrunden für das Gehirnjogging.

Zu guter Letzt möchte ich mich bei meiner Familie für die Unterstützung und den Rückhalt bedanken auf den ich mich bedingungslos verlassen kann. Danke, dass ihr mir helft, jede Hürde die ich mir in den Weg stelle zu nehmen. Vielen lieben Dank, *Gergana Borisova*, dafür, dass du der entscheidende Faktor warst wieso ich diese Promotion angefangen, und trotz aller Widrigkeiten auch durchgezogen habe.

Erklärung:

Ich versichere, dass ich diese Arbeit selbstständig verfasst, und keine anderen als die angegebenen Quellen und Hilfsmittel benutzt habe.

Heidelberg, den 08. August 2022 . . . . . .

Declaration:

I hereby certify that the thesis I am submitting is entirely my own original work except where otherwise indicated.

Heidelberg, August 8th 2022 . . . . . .